UNIVERSITY OF CALIFORNIA SAN DIEGO

Structure Formation and Diffusive Transport in the Endoplasmic Reticulum

A dissertation submitted in partial satisfaction of the
requirements for the degree Doctor of Philosophy

in

Physics

by

Zubenelgenubi Chippendale Scott

Committee in charge:

Elena F. Koslover, Chair
Nigel Goldenfeld
Padmini Rangamani
Wouter-Jan Rappel
Johannes Schöneberg

2024

The Dissertation of Zubenelgenubi Chippendale Scott is approved, and it is acceptable in quality and form for publication on microfilm and electronically.

University of California San Diego

2024

TABLE OF CONTENTS

LIST OF FIGURES

LIST OF SUPPLEMENTAL VIDEOS

ACKNOWLEDGEMENTS

I want to thank the long string of incredible teachers that got me here. Starting with naturalists and counselors at Mass Audubon getting me so excited about the birds, insects and plants around me that I started to memorize bird books like a total nerd; my first excellent science teacher in middle school, Dr. Kuranda for her warmth and passion; Mr. Sherry for kicking my butt throughout high school with math classes I would to this day probably only get a B in (and serving as a patient advisor to a very much not grown up teenager); Ms. Cyrier for setting me down the road of physics by teaching some damn good physics and math classes; my physics professors at Reed, in order of appearance, Nelia, Johnny, Darrell, Lucas, Joel, John and Alison, who crafted a one-of-a-kind curriculum and environment that I cherish and always strive to recreate.

This brings me to graduate school and my advisor, Elena Koslover, whose patient, attentive mentorship and endless (apparently tea-fueled) drive has been the biggest contributor to my growth as a scientist. I would like to thank all fellow members of the Koslover group for their friendship over the years. Specifically Saurabh and Anamika for welcoming me to the group in the midst of Covid; Keaton for being a research confidante and always providing great feedback on my work and presentations; I will miss our daily lunches at the much-coveted, butterfly-garden table. Hold down the fort! Mario, for his immediate sincerity and scientific guidance, and Owen and Lizzy for their enthusiasm and camaraderie.

I want to thank Kristin and Clark, for putting up with me and Natalie for 3 of these 6 years. That's a lot of time! I am forever indebted to you for your support, and your many delicious meals, especially this last year upon the arrival of June.

I owe everything to my parents, Janet and Rob, whose individual influences (doctor-y and artistic?) are apparent on my trajectory in science. To both, thank you for your belief in me and for your decades of endless love and support, which has been brought further into focus as I've embarked on raising a child of my own.

Finally, Natalie and June. Thank you for keeping me afloat whenever life gets hard, and

(more Natalie on this one) whenever I want a figure, paper, presentation, or application to be *good*, turning into my personal scientific editor. Thank you for everything.

Chapter 2, in full, is a reprint of the material with minor edits as it will appear in Zubenelgenubi C. Scott, Samuel B. Steen, Greg Huber, Laura M. Westrate, and Elena F. Koslover. "The Endoplasmic Reticulum as an Active Liquid Network." Proceedings of the National Academy of Sciences, (2024)

Chapter 3, in full, is a reprint of the material with minor edits as it appears in Zubenelgenubi C. Scott, Aidan I. Brown, Saurabh S. Mogre, Laura M. Westrate, and Elena F. Koslover. "Diffusive search and trajectories on tubular networks: a propagator approach." The European Physical Journal E 44, no. 6 (2021): 80.

Chapter 4, in full, is a reprint of the material with minor edits as it appears in Zubenelgenubi C. Scott, Katherine Koning, Molly Vanderwerp, Lorna Cohen, Laura M. Westrate, and Elena F. Koslover. "Endoplasmic reticulum network heterogeneity guides diffusive transport and kinetics." Biophysical Journal 122, no. 15 (2023): 3191-3205.

VITA

2016	Bachelor of Arts, Reed College
2017	Master of Advanced Study, King's College, University of Cambridge
2018-2020	Teaching Assistant, Department of Physics University of California San Diego
2021-2024	Graduate Student Researcher, University of California San Diego
2023	Instructor of Record, Department of Physics University of California San Diego Diego
2024	Doctor of Philosophy in Physics, University of California San Diego

ABSTRACT OF THE DISSERTATION

Structure Formation and Diffusive Transport in the Endoplasmic Reticulum

by

Zubenelgenubi Chippendale Scott

Doctor of Philosophy in Physics

University of California San Diego, 2024

Elena F. Koslover, Chair

The endoplasmic reticulum is a highly conserved organelle throughout the eukaryotes. The endoplasmic reticulum (ER) forms a vast network of membrane-bound tubules and stacked sheet-like structures that fill the cell, connecting distant structures like the nuclear envelope, the plasma membrane and many other organelles such as mitochondria and endosomes. It plays critical roles in cell signaling (through Ca^{2+} release), the cellular stress response, lipid biosythesis and storage, and the production and quality control of secreted proteins.

This work employs a diverse set of modeling tools paired with quantitative image analysis techniques to better understand the structure-function relationship of the ER. In Chapter 2, we develop a model that takes into account the micro-scale fluctuations that drive ER motion to

recreate the large-scale morphology of the ER. Several key geometric features are found to match the mammalian ER. Analytic calculations, informed by the growth laws of polygons (regions between tubules) in simulated networks, also recreate observed polygon size distributions and survival times.

In Chapter 3, we develop propagator-based methods for efficiently calculating search times and simulating diffusive search and reaction processes on stationary spatial networks. These powerful methods shed light on several important design choices of intracellular structures such as the peripheral ER and mitochondrial networks.

In Chapter 4, these techniques are paired with live-cell photoactivation experiments to explicitly demonstrate how ER network heterogeneity influences protein transport. Through the use of the aforementioned model for network dynamics, we show that network rearrangements are too slow to substantially affect protein transport at the several micron scale. Additionally, we identify the existence of hot-spots within the ER network structure, wherein sparse diffusive reactants are more likely to encounter one another. Altogether, these results drive forward our understanding of the ER as a dynamic, structurally-complex hub for the transport and reaction of biomolecules

Chapter 1

Introduction

A defining feature of eukaryotic cells is the existence of specialized organelles which compartmentalize reactions and aid in the storage and transport of essential biomolecules. This compartmentalization into organelles makes large, complex, highly evolved cell types possible [1]. One such organelle, the endoplasmic reticulum (ER), is conserved across the eukaryotes and fills the cell with an interconnected web of membrane-bound tubules (the peripheral ER), stacked-sheet volumes near the nucleus and other diverse, interspersed, complex structures (Fig. 1.1A). Bound within the ER membrane is a single, continuous aqueous lumen, separate from the cytoplasm, with a distinct population of proteins and a high concentration of Ca^{2+} ions. With its unique morphology and composition, the ER fulfills diverse functional roles within the cell. As the first step in the secretory pathway, it is a site for the translation, quality control and transport of proteins [2]. Via ion pumps and channels, the ER acts as a reservoir for Ca^{2+}, facilitating intra- and extra-cellular signaling [3, 4]. The ER also synthesizes, stores and delivers lipids throughout the cell via contacts with other organelles and budding processes [5, 6]. The ER forms important contact sites with many subcellular structures [7, 8] and is highly dynamic, allowing it to accomplish a variety of tasks, all while adapting to changing cellular and environmental conditions [9].

In addition to its essential role in the transport of proteins, lipids and ions, the ER functions as a quality-control center for newly synthesized proteins destined for secretion [2]. These

proteins must interact with ER-resident chaperones for proper folding and then locate ER exit sites (ERES) for transport out of the organelle. The ERES are stable structures budding from the ER that package secretory cargo into vesicles for delivery to the Golgi apparatus [10, 11, 12, 13]. As there is no established method for active transport within the ER, proteins must diffuse to find their chaperones and exit sites (Fig. 1.1B). Thus, understanding how the ER's network architecture influences particle transport and encounter kinetics is vital for comprehending its biological functions.

Perhaps due to its omnipresence within the cell, perturbations to ER structure are associated with a variety of human diseases, most notably, neurodegenerative diseases such as hereditary spastic paraplegias, amyotrophic lateral sclerosis (ALS) [14], and Alzheimer's [15, 16]. From these diseases, it is clear that the unique structure of the ER is key to supporting its many functions within the cell. Specifically *how* the structure impacts function remains opaque. To achieve a better understanding of this organelle and its role in health and disease requires quantitative, physical descriptions of structure formation and the effects of network morphology on biological transport and function, which is the focus of this work.

Previous research has focused on how the ER's various morphologies [17] arise from a combination of ER morphogen proteins and membrane mechanics. For example, certain proteins induce and stabilize the positive curvature of tubules [18, 19], while others maintain the spacing between sheets [20, 21]. Junction formation is mediated by proteins like lunapark and the atlastin GTPase family [22, 23, 24]. The relative abundance of junctions, tubules, and sheets is determined by the concentrations of these curvature-producing proteins and by membrane tension [20, 25]. Recent models have shown that tuning the proportions of these proteins can generate a variety of ER morphologies, highlighting the role of membrane curvature and low tension in forming intricate ER structures [26].

In addition to the effects of morphogen gradients and membrane mechanics, active forces drive the ER to be highly dynamic. New tubules often form when motor proteins such as dynein or kinesin-1 bind to the ER and pull out a new tubule while walking along acetylated

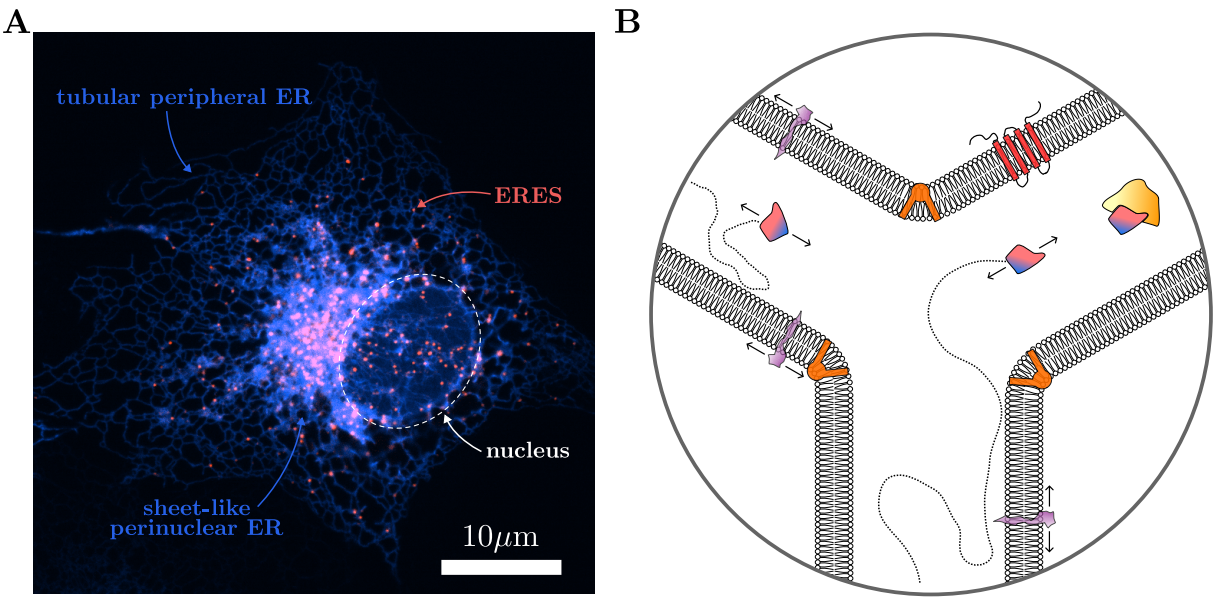

Figure 1.1. Structure and transport in the endoplasmic reticulum. (A) Confocal image of COS7 ER (blue, BFP_KDEL) and distribution of ER exit sites (red, mCherry_Sec23A). Image courtesy of Professor Laura M. Westrate, Calvin University. (B) Schematic of an ER junction at the sub-micron scale. Proteins diffuse through the membrane or lumen of the ER while searching for binding partners or exit sites.

microtubules [27, 28]. Other mechanisms involve the ER attaching to dynamic microtubule plus-ends [29] or motile organelles [30, 31, 32]. The inherent membrane tension in the lipid bilayer of the tubules also leads to junction sliding and loop closure, similar to rearrangements observed in systems such as foams [33], epithelial cell monolayers [34], and crystal grains [35]. These structural changes can be functionally significant, such as when aiding in the fission of mitochondria [32] and endosomes [36]. The balance of new tubule nucleation and junction sliding leads to an adaptive, constantly evolving steady-state structure.

Research has explored the relationship between ER dynamics and structure. For instance, the movement of ER exit sites along tubules has been modeled as motion along a semi-flexible polymer [37]. The dynamics of the ER also influence other cellular structures, such as the distribution of microtubules, which has been shown to be regulated by the motion of ER junctions [38].

In other systems, such as plant cells [39, 40] and reconstituted lipid-protein systems [41],

the ER has been shown to behave as a network which minimizes its length over time. Although these models focused on small ER regions, they provided insights into difficult-to-measure biophysical quantities such as local membrane tension and the viscoelastic properties of the cytoplasm. A key aspect of these studies, which we apply to our work, lies in the assumption that the ER behaves as a network with constant tension propagated along fluid-like tubules. This approach is distinct from traditional models of intracellular networks (e.g. actin and microtubule lattices) where filaments are treated as polymer chains with spring-like stretching and bending energies.

To connect the small-scale dynamics of the peripheral ER to its large-scale structure, in Chapter 2 we develop a physical model of the ER as an 'active liquid network.' Junction mobility and tubule spawning rate are identified as the two key factors regulating network density. The balance between tubule creation and annihilation determines the network's steady-state density and connectivity profile. Our model reproduces key geometric features of the ER, such as the distribution of areas between tubules, and shows how the ER's large-scale structure emerges from local dynamics. Through static tethering of the ER to the cytoskeleton and withdrawal of newly growing tubules, cells can tune junction mobility and tubule spawning rates, respectively, thus affecting steady-state network properties. Using a combination of computational models, analytical calculations, and quantitative image analysis of living mammalian cells, we identify physical rules governing ER formation and maintenance at the cellular scale.

Ultimately, it is critical to connect the dynamic structural properties of the ER to its function as a hub for the storage and diffusive transport of proteins, lipids and ions. This is a fundamental problem with broad significance: diffusive transport in complex geometries plays a crucial role in numerous biophysical processes, including transcriptional regulation in the nucleus [42, 43], reactions within organelles [44, 45], and intercellular communication through channels and bridges [46]. The morphology of these environments significantly impacts diffusion-limited reactions. Switching between compact and non-compact search processes, depending on the domain's effective dimensionality, changes the kinetics, a concept referred to

as ‘geometry-controlled kinetics’ [47, 48]. Confined diffusion can lead to unique behaviors in multimolecular systems, such as ultrasensitivity, bistability, and proofreading [49, 50, 51]. When domain structures change dynamically, they can also alter diffusion rates [52, 53] and expand the range of search times for reactions [54].

A key class of these confined diffusion processes occurs on spatial networks, which include organelle structures [55, 45], neuronal trees [56], and porous media [57, 58]. Spatial networks, characterized by nodes and edges embedded in physical space, have a limited node degree because connections are restricted to nearby neighbors [59]. Traditional studies of random walks on networks often assume uniform hop times, treated either as discrete steps [60, 61] or constant-rate processes [62, 63]. However, recent advancements have introduced theories for heterogeneous continuous-time random walks, which account for transition times that vary across the network [64].

Particle diffusion along edges in a spatial network produces a broad distribution of inter-node transition times, dependent on edge length [45]. In Chapter 3, we develop mathematical methods to compute reaction mean first passage times (MFPT) on arbitrary spatial networks, incorporating diffusion as a physical transport process along edges. Unlike past models that used a single effective rate constant for node transitions [63, 62], our approach explicitly includes edge-length-dependent transition time distributions and splitting probabilities, linking local diffusive dynamics to large-scale transport.

In many reaction-diffusion systems, more than just the mean first passage time is needed to understand the behavior of interest. Biochemical processes might depend on extreme value statistics [65] or require consideration of particles that repeatedly return to a target [49]. These complexities often necessitate stochastic simulations beyond analytical methods. A family of agent-based simulation methods, known as kinetic Monte Carlo [66], are well-suited for simulating particle diffusion in complex geometries, as they efficiently manage computational time by adapting the propagation timestep to local domain structures. We build tools for simulating diffusive transport informed by this prior research.

In this work, we introduce new algorithms to quantify target search and reaction kinetics in spatial networks, accounting for the effects of variable edge-length and connectivity profiles. We focus on tubular networks similar to those formed by intracellular reticulated organelles like the endoplasmic reticulum (ER) and mitochondrial networks. Our framework accurately computes search and encounter time distributions for diffusive particles, using both analytical and stochastic simulation methods. With these techniques, we explore the notion of optimality in ER networks, and identify potential design principles dictating the broad dispersal of ER exit sites for optimal export of proteins. Building upon this, in Chapter 4, stochastic simulations reveal that ER heterogeneity creates 'hot spots' where diffusing reactants are more likely to meet. In live cells, we show that ER exit sites are frequently located in regions with higher accessibility due to network connectivity and proximity to the nucleus. Thus, we model the kinetics of various molecular processes confined within tubular networks, providing a comprehensive understanding of diffusive transport in these intricate structures.

With these powerful new methods in hand, we can begin to probe how specific structures in the cell affect the transport of biomolecules, with direct comparison to imaging of the ER and its resident proteins in living cells. Prior research emphasizes the importance of network connectivity, which can be influenced by mutations affecting ER morphogens [22, 38, 4]. While earlier studies primarily examined global network properties like mean first-passage times, cellular networks are not uniform lattices, and local transport variability can significantly affect particle encounter rates and distribution within the cell [67].

Chapter 4 focuses on the spatial heterogeneity of the peripheral ER network in mammalian (COS7) cells and the impact this has on the diffusive transport of proteins. We show that structural differences within individual ER networks lead to varied diffusive access across different ER regions. Using live-cell imaging, we demonstrate that photoactivated membrane proteins spread unevenly to nearby ER areas, consistent with simulations predicting preferential transport to well-connected regions. We also simulate diffusive transport on the aforementioned model of the ER as an active liquid network, finding little effect of dynamic ER rearrangements on membrane

protein distribution. This work highlights the relationship between ER network structure and its function in regulating diffusion-limited reactions and local protein distribution.

In this dissertation, we explore how the unique structure of the peripheral ER arises from simple mechanical laws and how these emergent morphological features impact the biological function of the cell, viewed through the lens of diffusion-mediated transport and reaction processes. Paired with quantitative analysis of live-cell imaging data, we identify key design principles connecting the physical laws of pattern formation with biological transport and regulation of kinetics within cells.

Chapter 2

The Endoplasmic Reticulum as an Active Liquid Network

2.1 Abstract

The peripheral endoplasmic reticulum (ER) forms a dense, interconnected, and constantly evolving network of membrane-bound tubules in eukaryotic cells. While individual structural elements and the morphogens that stabilize them have been described, a quantitative understanding of the dynamic large-scale network topology remains elusive. We develop a physical model of the ER as an active liquid network, governed by a balance of tension-driven shrinking and new tubule growth. This minimalist model gives rise to steady-state network structures with density and rearrangement timescales predicted from the junction mobility and tubule spawning rate. Several parameter-independent geometric features of the liquid network model are shown to be representative of ER architecture in live mammalian cells. The liquid network model connects the timescales of distinct dynamic features such as ring closure and new tubule growth in the ER. Furthermore, it demonstrates how the steady-state network morphology on a cellular scale arises from the balance of microscopic dynamic rearrangements.

2.2 Introduction

The endoplasmic reticulum (ER) consists of a vast interconnected web of membrane-bound tubules and sheets in eukaryotic cells. It forms connections with many subcellular structures [7, 8], synthesizes and delivers lipids to other organelles [6, 5], stores and releases calcium [3, 4], and serves as a hub for the translation, folding, and quality control of secreted proteins [68, 2]. The ER is highly dynamic and assumes a variety of structural motifs, which aid in accomplishing these diverse functional roles and maintaining its interconnection with other organelles [9].

Prior work on ER structure has focused on how its diverse morphologies (tubules, junctions, helicoidal ramps, fenestrated sheets, cisternae, etc. [17]) arise from an interplay of ER morphogen proteins and membrane mechanics. A variety of ER membrane proteins (including the reticulons and the DP1/REEP/Yop1p family) induce and stabilize the high positive curvature of tubules [18, 19]. Others (e.g.: Climp63) stabilize the thickness of sheets and tubules [20, 21], while proteins such as lunapark [22] and the atlastin GTPase family [23, 24, 22] help to form and maintain junctions. It has been shown that the relative abundance of junctions, tubules and sheets is determined by a combination of the absolute concentrations of curvature-producing proteins and membrane tension [20, 25]. In other work, it was found that a diverse set of ER morphologies can be generated by tuning the proportions of reticulons and lunapark [69]. Recently, a model was developed which highlighted the role of intrinsic membrane curvature and ultra-low tensions in generating ER tubular matrices, ER sheet nanoholes and other intricate membrane structures [26]. These studies have helped elucidate the diverse structures observed in the ER as manifestations of local mechanical equilibrium.

Other work has sought to understand the link between ER dynamics and its structure. For instance, the anomalous diffusion of ER exit sites (ERES) along tubules is captured by a model of an individual ER tubule as a semi-flexible polymer [37]. The fluctuations of individual tubules have also been quantified, with variations in their dynamic behavior associated with

different regions of the cell [70]. The dynamics of the ER are also implicated in controlling other subcellular structures; for instance, the motion of junctions may help regulate the distribution of microtubules within the cell [38].

Prior modeling work on plant cell ER [39, 40] demonstrated how small networks between persistent points appear to minimize the length of intervening tubules. This is consistent with observations from in vitro studies of reconstituted lipid-protein systems, where the tension responsible for rearrangements is theorized to arise from the dimerization of membrane proteins [41]. Although these studies focused on small regions of the ER with only a few tubules, quantification of such minimal networks enabled estimation of biophysical quantities such as local membrane tension and viscoelastic properties of the cytoplasm. Notably, the ER was treated not as a polymer chain with spring-like stretching or bending energies, but rather as a network with constant tension along effectively fluid tubules, an assumption which we also adopt in this work.

The tubular network of the peripheral ER (Fig. 2.1A) undergoes dynamic rearrangements (Fig. 2.1B, Video S2.1) that include two frequently observed processes. First, there is the creation of new tubules, which branch from and remain connected to the existing network. Most commonly, tubule creation occurs when cytoplasmic dynein or kinesin-1 motors bind to the ER and walk along acetylated microtubules [27, 28]. Other mechanisms of new tubule growth include attachment of the ER to the dynamic plus-ends of microtubules, deemed TAC events [29], or to motile organelles such as trafficking endosomes [30], lysosomes [31] and mitochondria [32]. The second class of dynamic ER rearrangements arises from the inherent membrane tension in the lipid bilayer of the tubules. This tension induces junction sliding and neighbor rearrangements, akin to the T1 rearrangements observed in foams [33], leading to a net decrease in network edge length [71]. As a result, loops of tubules can shrink until they vanish, often referred to as loop or ring closure. Certain loop closure events play important functional roles in the fission of mitochondria [32] and endosomes [36], while other loop closures are rapid and do not appear to be associated with other organelles.

Similar structural rearrangements, such as T1 events and ring closures, have been observed in other physical systems characterized by interfaces under an effective tension. These include foams [72, 73], microemulsions [74, 75], crystal grain growth in metals [76, 35], and patterns formed by mass-conserving reaction-diffusion systems [77, 78]. The evolution of domain boundaries in these systems is driven by a curvature-dependent effective pressure and a characteristic rate of material transport across the boundary. The tendency of large domains to grow at the expense of small ones leads to domain coarsening over time with a characteristic scaling [33, 79].

Other space-tiling systems, such as epithelial cell monolayers, do not coarsen, but also undergo boundary rearrangements driven by a combination of interface tension and domain pressure [34]. Such monolayers exhibit T1 junction rearrangements, ring closure due to cell extrusion, and domain splitting arising from cell division. Domain splitting is also observed in ER networks, resulting from the spawning and growth of new tubules. However, the ER differs from previous classic models of foams, crystal grains, and monolayers due to the 'empty' nature of the domains between tubules, with no substantial resistance expected to the exchange of cytoplasm between neighboring domains.

With the aim of connecting the small-scale dynamic rearrangements of the peripheral ER to its large-scale topological structure, we develop a simple physical model of the ER as an 'active liquid network.' We first identify junction mobility and tubule spawning rate as the primary regulators of steady-state network density within the liquid network model. The balance of creation and annihilation of tubules leads to a network structure with a characteristic density and connectivity profile. Key geometric quantities from the ER of living cells, such as the distribution of areas between tubules and their shapes, are reproduced by this simple model. Liquid networks with physiological densities are also found to rearrange at a rate consistent with the living ER. Intriguingly, extracted laws for growth and shrinking dynamics in simulations are sufficient to recapitulate the distribution of areas, thus highlighting how large-scale structure emerges from local dynamics. Cells may modulate these properties by tuning their effective

junction mobility or tubule spawning rate. This could be achieved by static tethering of the ER to the cytoskeleton and other organelles and by withdrawal of newly growing tubules in 'catastrophe' events whose rate is quantified via semi-automated tracking in COS7 cells. Through computational models, analytic calculations, and quantitative image analysis of the peripheral ER in living mammalian cells, we identify physical rules governing its formation and maintenance on a cellular scale.

2.3 Results

2.3.1 Emergent network topology from tension and growth

Inspired by the dynamic processes observed in living animal cells and prior descriptions of small ER subregions as length-minimizing networks [39, 40, 41], we build a physical model of the large-scale mammalian peripheral ER as an active liquid network. Here, we focus on two-dimensional networks, relevant for adherent mammalian cells such as COS7 cells, whose thin periphery typically accommodate only a single layer of ER tubules [80]. The 2D nature of these ER networks is evidenced by the dearth of degree four junctions visible in planar projections of the network (Fig. 2.1A). We separately explore the extension of the model to three dimensions in SI Appendix (Fig. S1). The liquid network is composed of edges which transmit a membrane tension force between neighboring junctions. The membrane tension and tubule radii are assumed to be constant throughout the network.

In the low Reynolds-number environment of the cytoplasm, the motion of junction node i, located at position $\vec{r}_i$, is assumed to obey an overdamped Langevin equation (Fig. 2.1C):

$$\frac{d\vec{r}_i}{dt} = -b\nabla f(\vec{r}_i) + \sqrt{2D}\vec{\eta}(t). \tag{2.1}$$

Here, b is the junction mobility (units of μm/s), $f(\vec{r}_i) = \sum_{j=1}^{d} \left|\vec{r}_i - \vec{r}_j\right|$ is the total tubule length connecting junction i with its neighbors at positions $\vec{r}_j$, D is the junction diffusivity, and $\vec{\eta}(t)$ is a Gaussian distributed random noise term with zero mean and unit variance in each dimension.

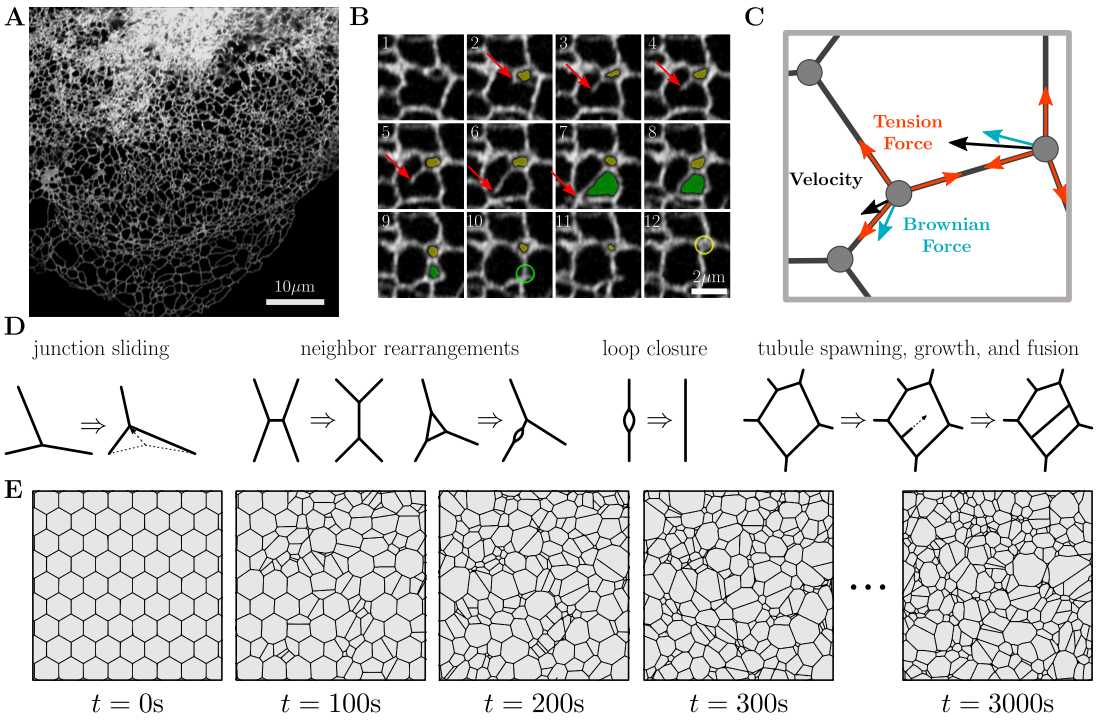

Figure 2.1. The dynamic structure of the endoplasmic reticulum is represented by a liquid network model. (A) Confocal image of COS7 cell expressing fluorescent endoplasmic reticulum (ER) marker (KDEL_mcherry), highlighting the peripheral ER network morphology. (B) Montage from same cell line illustrating the spawning of a new tubule (red arrow) and loop closure events (yellow and green shaded regions). Size of each image is 5.0×5.0 μm with a time step of 0.6 s between each frame. (C) Physical model of junctions in a liquid network. A length-independent tension force (red) and a Brownian force (blue) combine to define junction velocities (black). (D) Possible rearrangements within a liquid network include junction sliding, neighbor swapping and rearrangement, loop closure and tubule spawning, growth, and fusion. (E) Representative simulated liquid network evolves from initially uniform honeycomb lattice to a random structure, with characteristic steady-state density. Region shown is a small segment of a much larger domain.

The first term describes the deterministic response to length-minimizing tension forces along the edges, and the second term describes a random Brownian force meant to capture the noisy environment of the cytoplasm.

With the above laws of motion, liquid network junctions are frequently pulled into close contact. Within some threshold distance of one another, junctions may swap neighbors, allowing for T1 transitions that lead to a decreasing edge length. Model results are not sensitive to the choice of threshold distance (SI Appendix, Fig. S2). Example neighbor rearrangements are

shown in Fig. 2.1D. Occasionally, loops may form due to these neighbor swapping events, wherein two junctions are doubly-connected. These loops contract over time, due to there being twice as much tension pulling them together as there is pulling them apart. The network is not allowed to rupture or fragment, a process which can be induced in vitro [81] but is not observed in our data, potentially due to the high membrane tension in the ER [41].

In addition to the tension and diffusion driven motion of junctions, new tubule nucleation from existing tubules is modeled as an exponentially distributed random process with rate k (tubule spawning rate, units of $\mu m^{-1}s^{-1}$). Newly spawned tubules grow with a velocity v (μm/s), until coming into contact with an existing tubule, at which point the growth ceases and the tubules fuse, forming a stable junction.

In the endoplasmic reticulum, the velocity of growing tubules has been measured to be on the order of 1 μm/s [28, 82]. We assume that the velocities of growing tubules are fast compared to the junction mobility ($v \gg b$), so that a newly spawned tubule will span across a polygon before it substantially changes its shape. This assumption, justified via subsequently described measurements, allows us to treat tubule growth as nearly instantaneous. Additionally, the diffusive motion of junctions is assumed to be relatively small compared to experimentally observed tension-induced sliding events. With these assumptions, the behavior of the liquid network model can effectively be described by two parameters: the junction mobility, b, and the tubule spawning rate, k.

We simulate active liquid networks for a variety of parameter values, by integrating Eq. 2.1 forward in time (details in SI Appendix Methods). As seen in Fig. 2.1E, an initially uniform honeycomb network develops into a random network over time. The network continuously evolves, but after a transient initial period, the tubule density remains relatively unchanged. Thus, a steady state emerges due to the competing forces of junction motion controlled by edge tension and novel tubule spawning triggered by a random Poisson process.

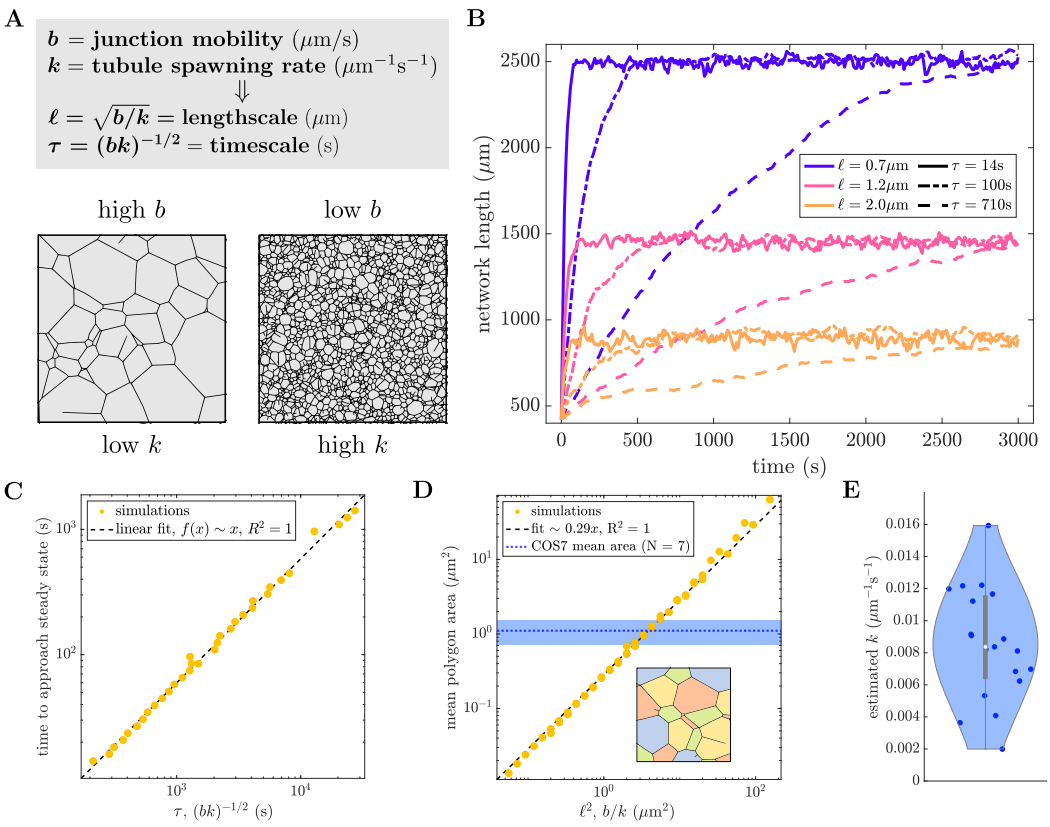

Figure 2.2. Steady-state network density and rearrangement timescales are set by two parameters. (A) Junction mobility and tubule spawning rate set the length and time scales (ℓ, τ respectively). (B) Network length over time for nine separate simulations, each starting from an initially sparse honeycomb network enclosed in a circle of radius 15 μm. The steady-state network length is set by ℓ (color) and the time to reach steady state is set by τ (line style). Other parameters are $D = 10^{-5}$ μm^2/s and $v = 1$ μm/s. (C) Timescale to approach steady state, extracted via exponential fit of curves as in (B) is proportional to the intrinsic network timescale τ. (D) The mean area of polygons in a liquid network is proportional to $\ell^2 = b/k$. Mean polygon area in COS7 cells is indicated by dotted blue line; shaded region gives inter-cell standard deviation ($N = 7$ cells). Inset: illustration of polygon extraction, different colored regions correspond to individual polygons. (E) Measured spawning rates from 19 COS7 cells, with mean and inter-cell standard deviation of $8.5 \pm 0.8 \times 10^{-3}$ μm^{-1}s^{-1}. Scatter data for (C), (D) is from simulations with mobility ranging between $0.001 - 0.1$ μm/s and spawning rate ranging between $0.0005 - 0.05$ μm^{-1}s^{-1}.

2.3.2 Steady-state density and timescales of liquid networks

Because the liquid network model is governed by only two parameters, dimensional analysis indicates there is a single characteristic length scale ($\ell = \sqrt{b/k}$) and timescale ($\tau = 1/\sqrt{bk}$) that define its behavior. Thus, changing the ratio of b and k generates networks with

varying steady-state density and changing the product of b and k affects the dynamics of the network (Fig. 2.2A, Video S2.2). To illustrate this effect, the results from nine simulations of liquid networks are shown in Fig. 2.2B. Each of the nine simulations has the same initial condition but a different combination of ℓ and τ.

The total network length approaches a steady-state value over time, and can be fit to an exponential of the form $f(x) = c\left(1 - \exp\left(t/\tau_{\text{steady}}\right)\right)$. The parameter τ_{steady} gives an estimate of the time for liquid networks to approach steady state. This extracted time scales linearly with τ over a wide parameter range, as expected for simulations with a single dominant timescale (Fig. 2.2C).

To measure steady-state density one can consider the area of polygons (minimal loops) within the network. The mean area of these polygons scales linearly with $\ell^2 = b/k$ (Fig. 2.2D). It is therefore possible to construct networks with the same density as observed in living cells simply by tuning ℓ. From a linear fit of the mean area across a range of b and k values we obtain $\langle A \rangle \approx 0.29 b/k$.

The overall steady-state density of liquid networks can be captured by a simple equation for the total network length as a function of the new tubule spawning rate k and mobility b. For simplicity, we consider a network of hexagonal polygons. The total network length L can either grow via spawning of new tubules across the polygons, or decrease due to junction sliding:

$$\frac{dL}{dt} = kL\lambda\sqrt{3} - \gamma bn. \tag{2.2}$$

Here, λ is the average edge length, $\sqrt{3}\lambda$ is the distance between parallel edges of a hexagon, n is the total number of junctions in the network, and γb describes the average sliding speed of a junction. At each individual junction, the value of γ must be between 0 and 3 depending on the angles between the adjacent tubules. The speed of growing tips is assumed to be sufficiently fast that growth events are instantaneous and there is no effect from the diffusion of junctions.

The total network length can be expressed in terms of the average edge length (λ) and

the number of junctions (n) using the fact that the number of edges (e) in a hexagonal lattice is $e = \frac{3}{2}n$. Thus, $L = \frac{3}{2}\lambda n$ and at steady state $\frac{dL}{dt} = 0$ gives an average area of:

$$\langle A \rangle = \frac{3\sqrt{3}}{2}\lambda^2 = \gamma\frac{b}{k}. \tag{2.3}$$

This predicted scaling of mean area with b/k aligns with expectations from dimensional analysis and agrees with the fit of simulation results. Notably, an analogous scaling law relating network dynamics and the average edge length is also observed for three-dimensional liquid network simulations (see SI Appendix, Fig. S1). However, such 3D networks also depend on an additional length scale (the contact radius within which a growing tube is capable of fusing into the network), which modulates network pore size and density.

The new tubule spawning rate k can be extracted directly from observations of ER dynamics in live COS7 cells (Fig. 2E, details in SI Appendix Methods). Together with the measured polygon area, this allows the effective mobility of the ER junctions in COS7 cells to be estimated as $b = \langle A \rangle k/\gamma = 0.03$ μm/s. We note that the relevant mobility is indeed much slower than the tubule growth speed ($b \ll v$), justifying our assumption of a single dominant length and time scale. One advantage of this approach is that tubule spawning rate is simple to directly measure from experimental data whereas junction mobility is a more opaque quantity. Thus, it is possible to calculate ER junction mobility via mean polygon area and spawning-rate measurements by taking advantage of the steady-state properties of liquid networks.

2.3.3 Scale-invariant network structure reproduces ER morphology

While the two parameters of the liquid network model set length and time scales, any dimensionless metric of network structure must be parameter-independent. In particular, we consider the full distribution of polygon areas for a range of ℓ values (Fig. 2.3A). As the ratio of mobility to spawning rate increases, the distributions shift to the right, indicating an increase in large areas and a decrease in small areas. However, the overall shape of the distribution

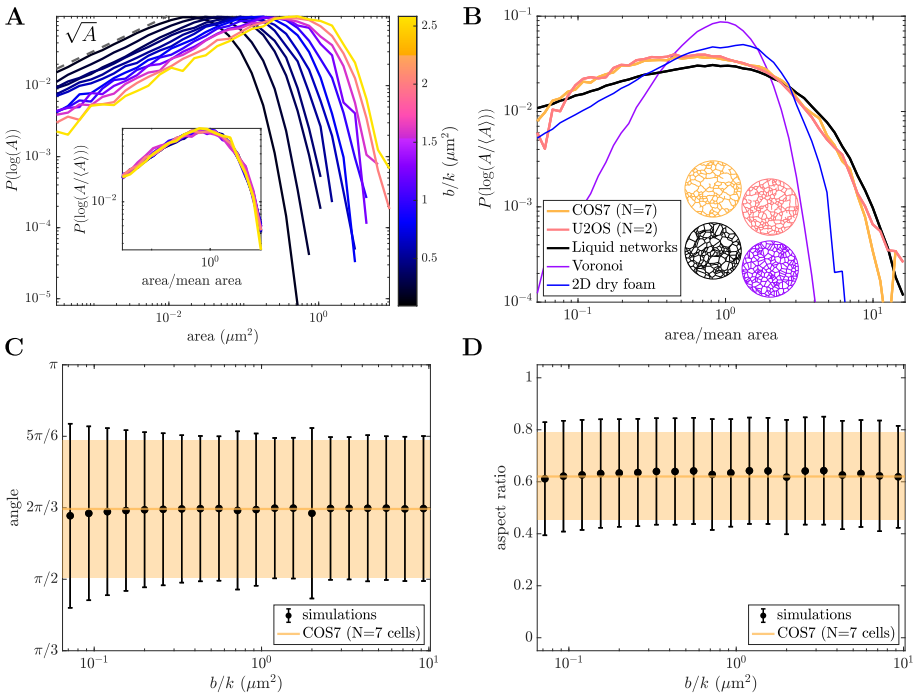

Figure 2.3. Scale-invariant liquid network model reproduces peripheral ER morphology. (A) Distribution of polygon areas in simulated liquid networks for a range of b/k values. Bin sizes are logarithmic. Inset: distributions collapse onto a single curve when normalized by mean area, revealing scale-invariant behavior of liquid networks. (B) Distribution of normalized polygon areas from the ER networks of COS7 and U2OS cells (yellow and pink, respectively) exhibit similar scaling to simulated liquid networks (black). For comparison, the distribution of areas for Voronoi networks and experimental measurements of a two-dimensional dry foam (data from [83]) are also shown (purple and blue lines). Example networks in matching color below. (C) Mean and standard deviation of angles between 3-way junctions in liquid networks (black) and the COS7 ER (yellow). (D) Mean and standard deviation of aspect ratio (shortest dimension/longest dimension) in liquid networks (black) and the COS7 ER (yellow).

remains unchanged. At low areas, the log-binned distribution scales as $\sim \sqrt{A}$ and at high areas it decays exponentially. When normalized by the mean area, the distributions collapse onto a single universal curve (Fig. 2.3A, inset), highlighting the scale-free nature of the model. Thus, increasing mobility is equivalent to "zooming in" on a patch of network, while increasing spawning rates leads to a denser network, or "zooming out."

Notably, the parameter-independent shape of the polygon area distribution for liquid networks provides a good approximation to that of the ER in living cells. In Fig. 2.3B, area distributions extracted from two different cell types commonly used to study the peripheral

ER are shown (details in SI Appendix Methods). Both COS7 and U2OS cells (monkey kidney and human osteosarcoma, respectively) exhibit remarkably similar scaling, collapsing onto a single curve. The exponential drop-off at large areas is clearly conserved across experiments and simulations. The experimental measurements exhibit a slight enhancement of small-area polygons as compared to liquid network simulations. However, limitations in imaging resolution and segmentation prohibit the extraction of a reliable power-law for small-area scaling in the distribution.

The distributions for two other families of network are provided in order to demonstrate that the close match to ER morphology is not exhibited by other commonly studied 2D networks. The area distribution of simulated Voronoi networks (purple line) is comparatively narrow and sharply peaked around the mean. Experimental imaging data of a two-dimensional dry foam [83] (blue line), shows that the area distribution of foams is broader than Voronoi networks but still narrower than the ER and liquid networks. The foam also exhibits an exponential drop-off at large areas but has a linear scaling in the logarithmic distribution of small-area polygons. We note that extending the liquid network model to three dimensions yields a distinctly different scaling for the size distribution of small pores, akin to that observed in foams and random-line networks (SI Appendix, Fig. S1).

For 2D liquid networks, it is possible to estimate the functional form of the liquid network area distribution (black line) using only the rules for polygon growth and splitting, as described in the following section.

Other metrics of shape further confirm the similarities between the liquid network model and experimental ER networks. The distribution of angles between neighboring 3-way junctions is centered at $2\pi/3$ or 120°. This is a universal property of two-dimensional networks composed of degree 3 junctions. The standard deviation of angles at 3-way junctions is also shown to be similar for simulated and ER networks across a wide range of parameter values (Fig. 2.3C). Finally, the aspect ratio of polygons (ratio of shortest dimension to longest dimension) is calculated in both simulated and experimental networks. This provides another dimensionless,

scale-free measure of shape: the mean and standard deviation of polygon aspect ratio are constant over a wide range of parameter values and approximately match experimental measurements (Fig. 2.3D). Notably, the realistic variances of the aspect ratio and junction angles arise from heterogeneity in polygon shapes and are not related to the Brownian forces on the junctions (SI Appendix, Fig. S2A-C), which are taken to be very small in the simulations.

Figure 2.4. Dynamics of liquid networks predict ER rearrangement timescales and give rise to emergent polygon area distribution. (A) Confocal images of COS7 ER with 1s interval between first and last frames (green, pink). Extracted networks overlaid in matching colors. White arrows indicate minimal distance from meshed points on final network (pink) to meshed points on the initial network (green). (B) Left panel: edge mean minimal distance (EMMD) over time for 16 peripheral ER networks of COS7 cells. Right panel: EMMD of liquid networks with $\tau = (bk)^{-1/2}$ varying across one order of magnitude and fixed $\sqrt{b/k} = 2$ μm. (C) Exponential timescale for EMMD to approach steady-state scales with τ for liquid network simulations. Yellow lines show mean value and intercellular standard deviation for COS7 cells. (D) Example polygon tracking of experimental data to quantify polygon growth and shrinking rates. Each frame is 5.0×5.0 μm with a timestep of 2 s. Red and green arrows indicate shrinking and growing polygons, respectively. (E) Non-dimensionalized growth rates normalized by mean area and network timescale for 10 liquid network simulations. Green curve indicates mean (and standard error of the mean) within coarse bins of normalized area. Dotted black curve indicates fit to Eq. 2.4, giving $\beta = 0.78,\ g = 1.69,\ h = 1.85$. (F) Mean growth rates normalized by mean area and their dependence on relative polygon size from 7 experimental COS7 peripheral ER networks. Green curve indicates mean (and standard error of the mean). Dotted black curve indicates fit to Eq. 2.4, with β fixed at 0.78 giving $g/\tau = 0.018\ \mathrm{s}^{-1}$, $h/\tau = 0.015\ \mathrm{s}^{-1}$. (G) Polygon growth timescale (defined as τ/g) from 7 COS7 cells agrees with the simulated timescales extracted from simulations. (H) Polygon survival times normalized by τ for 10 liquid network simulations. Green curve indicates mean (and standard error of the mean) within bins of area. Black curve indicates theoretical prediction. Inset: representative trajectories for shrinking and splitting polygons. (I) Distribution of normalized polygon areas in a simulated liquid network (black) compared to analytically approximated area distribution (pink). Vertical dashed line shows A^*, where small-area and large-area solutions are joined.

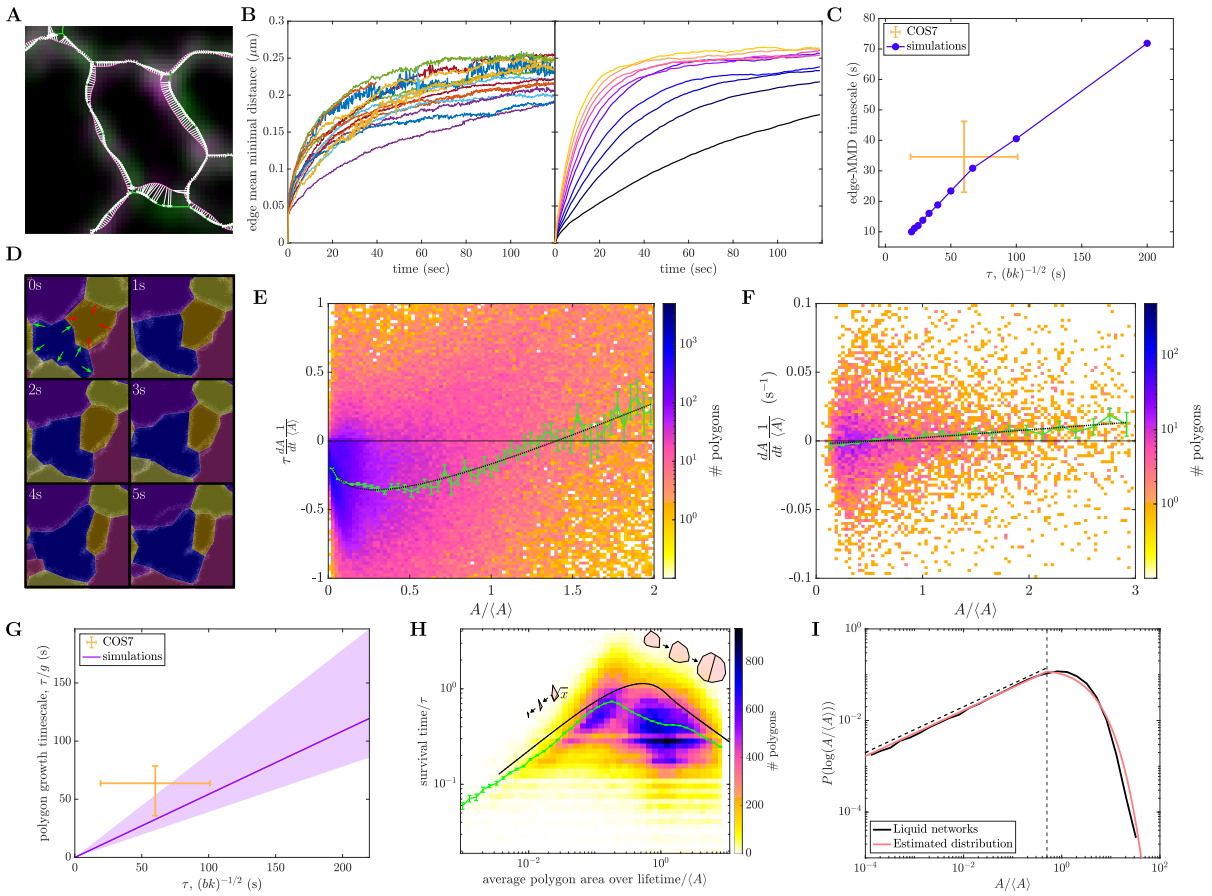
A
B
C
D
E
F
G
H
I
edge mean minimal distance (μm)
time (sec)
edge-MMD timescale (s)
COS7
simulations
τ, (bk)^{-1/2} (s)
0s
1s
2s
3s
4s
5s
polygons
A/⟨A⟩
polygon growth timescale, τ/g (s)
survival time/τ
average polygon area over lifetime/⟨A⟩
P(log(A/⟨A⟩))
Liquid networks
Estimated distribution

2.3.4 Model dynamics determine network rearrangement rates

Having demonstrated that the liquid network model approximately matches the steady-state morphology of ER networks, we next proceed to compare the dynamics of simulated and observed network structures. We consider two metrics for the dynamic rearrangement of the networks, demonstrating how parameters extracted from measuring polygon size and new tubule spawning enable accurate prediction of the time-evolution of ER network structure.

Edge mean minimal distance

To quantify the motion of individual tubules over time and the resulting changes in network structure, the edge mean minimal distance (EMMD) is calculated between the first and all subsequent networks, as described in SI Appendix Methods. Briefly, the network is meshed and for each point on subsequent networks, the minimal distance to a point on the starting network is found; these minimal distances are averaged to find the EMMD. The EMMD grows over time with an initial jump between the first and second frames that can be attributed to localization error and network segmentation artifacts (Fig. 2.4B, left panel). The same calculation is performed for simulated liquid networks with a matching average polygon size and a range of timescales.

Exponential fits of the EMMD growth over time give an effective timescale for the rearrangement of the network. As expected, this rearrangement time scales linearly with the intrinsic timescale τ of the simulations (Fig. 2.4C). The observed rearrangement timescale for the COS7 ER is 35 ± 11 s, implying that during this time edges are significantly displaced from their original location. This timescale is of similar magnitude to the time required for the ER as a whole to explore a large fraction of the cytoplasm [84]. Notably, this rearrangement timescale is consistent with the simulation model, given the parameters b and k extracted from measurements of polygon area and tubule spawning rate. Thus, the liquid network model makes it possible to connect two seemingly independent dynamic processes—new tubule growth and rearrangement of existing edges.

Polygon growth rates

An additional metric to quantify the dynamic behavior of liquid networks arises from considering the growth and shrinking rates of polygons (independent of splitting events due to new tubule growth). Polygons are tracked in time and space using conventional particle tracking software [85] (details in SI Appendix Methods). We calculate the normalized growth rate for all tracked polygons in several COS7 ER networks and simulated liquid networks. The normalized growth rate is defined to be the time-derivative of each polygon's area scaled by the average polygon area in that cell. For simulated networks, the growth rate is rescaled by the characteristic model timescale $\tau = (bk)^{-1/2}$, allowing simulations with different parameter values to be analyzed together. By determining the relationship between growth rate and polygon area the underlying laws governing the dynamics of the network can be probed.

A characteristic behavior of liquid networks is the growth of large polygons and the shrinking of small ones (Fig. 2.4E). This is similar to von Neumann's law for foams, which dictates that polygons with more than 6 sides grow while those with fewer sides shrink [72]. In liquid networks, as in foams [33] and crystal grain boundaries [35], polygons that are substantially larger than average tend to have more sides, as a greater number of average-sized neighbors can fit around them (SI Appendix, Fig. S3A). Consequently, such above-average polygons tend to have internal angles greater than 120°, causing them to grow under tension. As noted in SI Appendix, the growth and shrinking rates for a regular n-gon are expected to be proportional to its perimeter, which scales roughly as $\sqrt{A}$. For large polygons, the number of neighbors should also increase as the polygon grows, giving a steeper dependence of the growth rate on area. We fit the average simulated growth rates to the following expression: (Fig. 2.4E):

$$\tau \frac{1}{\langle A \rangle} \frac{dA}{dt} = g \left(\frac{A}{\langle A \rangle} \right)^{\beta} - h \sqrt{\frac{A}{\langle A \rangle}}, \tag{2.4}$$

where the prefactor g encapsulates the rate of large polygon growth and h describes the rate of

small-polygon shrinkage. We note that the above equation constitutes an approximate ansatz that describes the distinct dynamic behavior of polygons at the extremes of the area distribution. From the fitted function, we can extract the typical rate $k_{\text{grow}} = g/\tau$ for the growth of large polygons.

When tracking polygons in images of live ER, the average growth rate is also negative for small polygons and positive for large ones, as in the liquid network model. Due to the limited data at small polygon areas, we fix the value $\beta = 0.78$ as fitted for simulated networks, and fit the remaining coefficients in Eq. 2.4 to the experimental data (Fig. 2.4F). This enables the extraction of a growth rate for large polygons, in real time units. As shown in Fig. 2.4G, the estimated growth rate for COS7 ER falls within range of the predicted value for liquid networks with the appropriate timescale τ. Thus, by measuring the average polygon area and rate of new tubule spawning (to set parameters b, k), the liquid network model makes it possible to predict the typical growth rate of large polygons in the ER network, thereby connecting distinct dynamic processes.

These results demonstrate that liquid networks are not only able to replicate key steady-state structural features but also capture the rearrangement timescales of living ER networks, providing a connection between morphology and tubule dynamics.

2.3.5 Steady-state structure emerges from polygon dynamics

The dynamic behavior of network polygons can be abstracted still further by considering them as a population of individual aspatial entities capable of growing, shrinking, and splitting (SI Appendix, Video S2.3). The drift velocity of polygon areas $v(A) = dA/dt$ is set by Eq. 2.4. The rate of splitting is expected to be proportional to the perimeter of a polygon, which scales as the square root of the area: $k_{\text{split}} = \hat{k}\sqrt{A}$. This simplified description neglects noise in the polygon trajectories, assuming the dynamics of each is consistent with the average behavior of the population.

Polygon survival times

The normalized area of a given polygon [$\hat{A}(t) = A(t)/\langle A \rangle$] can be treated as a deterministically growing or shrinking quantity, computed through integration of Eq. 2.4. The polygon will grow if its initial normalized area is above the cutoff value of $\hat{A}_c = (h/g)^{1/(\beta-1/2)}$ and will shrink otherwise. The polygon trajectory is terminated by a stochastic event with rate k_{split}.

For a shrinking polygon with initial area $\hat{A}_0$, we can compute the time to closure as $t^* = \int_0^{\hat{A}_0} \frac{-d\hat{A}}{v(\hat{A})}$. The survival probability $S(t)$ to time $t < t^*$ is given by

$$S(t) = e^{-\hat{k}\sqrt{\langle A \rangle}\int_0^t \sqrt{\hat{A}(t')}dt'}. \tag{2.5}$$

and the average survival time can be found as

$$\tau = t^* S(t^*) - \int_0^{t^*} t' \partial_{t'} S(t') dt' = \int_0^{t^*} S(t') dt'. \tag{2.6}$$

For growing polygons, an analogous expression for the average survival time is given by replacing $t^* \to \infty$. The resulting estimate for the survival time approximately matches the behavior of polygons in liquid network simulations (Fig. 2.4H). Notably, polygons with intermediate areas have the longest survival time because they are both slow to shrink and also have a low splitting rate.

Because this simplified model of polygon dynamics does not incorporate stochastic noise in the trajectories, the approximated survival times tend to be slightly over-predicted. In simulations, some polygons with area below $\hat{A}_c$ may nevertheless be growing and some larger polygons may be shrinking. As a result, polygons spend less time trapped in the intermediate-area state where deterministic dynamics are very slow and are more likely to fluctuate to a more extreme small or large area that quickly leads to a shrinkage or a splitting event, thereby reducing the survival time.

Steady-state area distribution

Making the same approximation of deterministic dynamics for the population of polygon areas, we define $P(A)$ as the area distribution function, whose steady-state form must encompass a balance between small polygons disappearing due to shrinking and large polygons splitting into new ones.

In the limit of very small areas, the formation and disappearance of polygons due to splitting is negligible compared to the flux associated with polygon shrinking (SI Appendix). The overall rate of polygons disappearing when their area shrinks to zero can be estimated as:

$$J_0 = \lim_{A\to 0} v(A)P(A) = \lim_{A\to 0} \frac{h}{\tau} \langle A \rangle^{1/2} \sqrt{A} P(A). \tag{2.7}$$

Because this flux must be a finite non-zero value, the small-area limit of the distribution is set to $P(A) \to c_1/\sqrt{A}$, where c_1 is a constant. A logarithmic transform gives the scaling $P(\log A) \sim \sqrt{A}$, as observed in Fig. 2.3A.

In the limit of very large polygons, the distribution evolves due to area growth and splitting, and the steady-state form can be found by solving the resulting equation:

$$\frac{\partial P}{\partial t} = -\frac{\partial}{\partial A}\left[v(A)P\right] - \hat{k}\sqrt{A}P = 0 \tag{2.8}$$

$$P(A) \to c_3 c_1 A^{-\beta} e^{-c_2 A^z} \tag{2.9}$$

where $z = \frac{3}{2} - \beta$, $c_2 = -\frac{\hat{k}\langle A \rangle^{\beta-1}}{gz}$, and c_3 is a constant.

In order to construct a full approximate distribution, the two limits for small and large area are married together at some intermediate value A^*, thereby enforcing a value for the coefficient $c_3 = (A^*)^{1-z} \exp(c_2 A^{*z})$. The coefficient c_1 is obtained by normalizing $P(A)$. Furthermore, the total rate at which polygons disappear (J_0) and the rate at which new ones are produced ($J_{\text{split}} = \int_0^\infty \hat{k}\sqrt{A}P(A)dA$) must be equal at steady state. This constraint fixes the transition value $A^* \approx 0.12b/k$.

These calculations lead to a predicted average polygon area $\langle A \rangle \approx 0.23(b/k)$, similar to the fitted relationship in Fig. 2.2D. Furthermore, the overall distribution of polygon areas, with a polynomial scaling at small A and an exponential scaling at large A, approximately reproduces the observed distribution from liquid network simulations (Fig. 2.4I). We note that the only fitting parameters employed in this analysis are the values of g, h, β in the expression for polygon growth rates as a function of area (Eq. 2.4). Thus measurement of polygon dynamics can be leveraged to approximately predict the steady-state architecture of the liquid network as well as the ER network structure in live cells.

2.3.6 Pinning to static structures increases network density

We have shown how the structure and dynamics of liquid networks are governed by two parameters, the junction mobility and tubule spawning rate. In the next two sections, we explore how the cell effectively controls these parameters to modulate ER properties, first examining how junction mobility can be tuned by tethering of the ER to static structures.

The ER exists within the crowded, complex environment of the cytoplasm. It is pinned to the cytoskeleton via contacts with microtubules and actin filaments [86, 87]. The ER also forms critical contact sites with mitochondria [28, 32, 88], the plasma membrane [89], the Golgi [90, 91], endosomes [30, 36] and other organelles [7]. Quantification of ER network dynamics in plant cells has indicated that certain points along the network remain persistent over minute-long timescales [39]. To determine the effect of connections to static structures, we introduce a process for temporarily immobilizing junctions in liquid networks via pinning (rate k_p). An unpinning process (rate k_u) allows for a steady-state number of pins (Video S2.4). The ratio $n_p = k_p/k_u$ sets the average number of pins in the model. We analyze systems with variable pin densities and with a wide range of pin persistence times.

To begin, we find how mean area depends on both junction mobility and pin density, calculated as n_p divided by total simulation area (Fig. 2.4A). For a fixed mobility, increasing the density of pins leads to a denser network with smaller mean areas. This effect is most pronounced

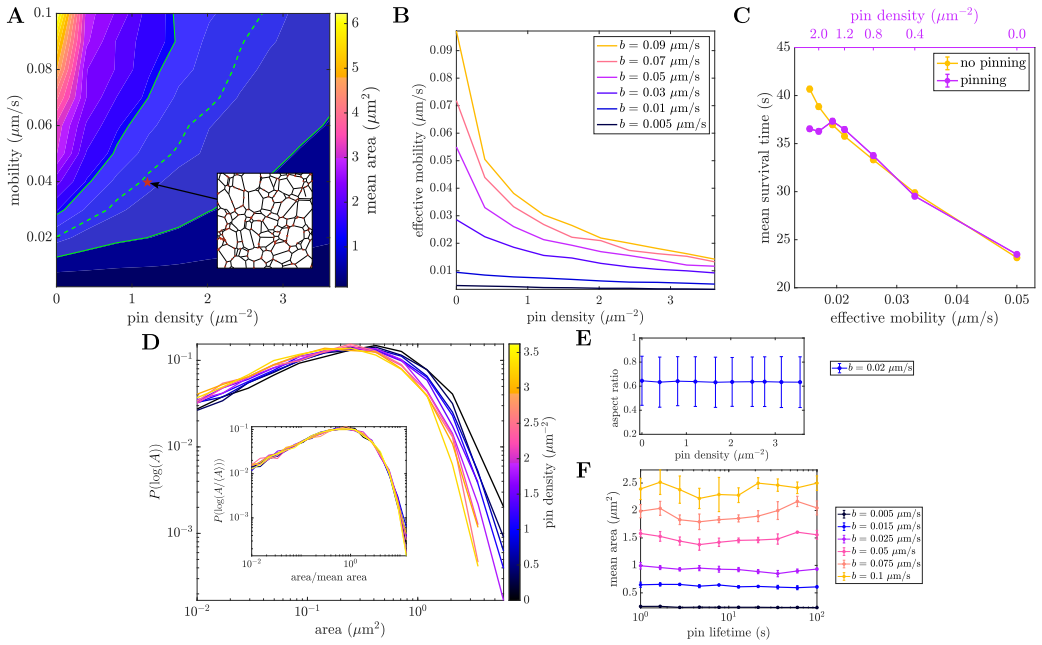

Figure 2.4. Tethering to static structures reduces effective mobility and increases network density. (A) Dependence of mean area on mobility and pin density. Dashed green line indicates contour corresponding to mean COS7 area, with shaded green region indicating standard deviation across all cells (N=7). Inset depicts an example 10×10 μm snapshot of a liquid network with pinned nodes highlighted in red. (B) Effective mobility, defined as $b_{\text{eff}} = \langle A \rangle k/\gamma$, as a function of pin density for different mobilities. (C) Mean polygon survival time for simulations with and without pinning. Yellow curve: no pinning, varying node mobility b (bottom axis). Pink curve: different pin densities (top axis), with constant mobility $b = 0.02$ μm/s, plotted against the effective node mobility b_{eff} (bottom axis). Matching effective mobilities gives similar results with and without pinning. Error bars indicate standard error of the mean. (D) Reversible pinning leads to denser networks, shifting the area distributions. Inset: normalized area distributions collapse to a single curve for all pin densities. (E) Aspect ratio is unchanged across a range of pin densities. (F) Mean area remains constant across a wide range of pin lifetimes. All results are with a tubule spawning rate of $k = 0.005$ μm^{-1}s^{-1}.

for larger mobilities, leading to a steep decrease in mean area as pin density increases. The contour corresponding to the average area across COS7 cells is shown in green, indicating a wide range of possible mobility and pin density combinations in experimental networks.

The overall effect of pinning is to reduce the rate at which the network can relax and rearrange. For any given pin density, we can define an 'effective mobility' ($b_{\text{eff}} = \langle A \rangle k/\gamma$, with $\gamma = 0.29$) by finding the value of b that would give the same average polygon area in the absence of pinned points. At low pin density, $b_{\text{eff}} \approx b$, but as the pin density grows, the effective mobility

steeply decreases (Fig. 2.4B) as the rearrangement of the network is slowed down. Notably, the effect of pinning on the survival time of individual polygons is almost completely encompassed by the accompanying change in effective mobility (Fig. 2.4C).

In liquid networks, pinning to static structures or other organelles may thus limit network mobility and increase the corresponding density of ER network tubules in critical regions of the cell. For instance, this mechanism could aid the coalescence of ER around mitochondria contact sites.

There is little effect from pinning beyond tuning the density of the network. Area distributions shift as a function of pin density, but when normalized by mean area, the data collapse onto a single curve (Fig. 2.4D) just as in the case without pinning (Fig. 2.3A). There is also no effect on the mean and variance of polygon shape, as measured by aspect ratio (Fig. 2.4E). Furthermore, altering the pinning and unpinning rates (thus probing a wide range of pin lifetimes while maintaining a fixed pin density) has no effect on the steady-state structure of liquid networks (Fig. 2.4F).

2.3.7 Tracking tubule spawning in COS7 ER reveals rate of catastrophe

Another mechanism through which cells can modulate ER network properties is by tuning tubule spawning rate. Within living cells, newly spawned tubules often cease growth and retract, a process we refer to as 'catastrophe'. Independent of the underlying mechanism of growth (e.g. ER sliding or TAC events [27, 28, 29]), we quantify ER tubule catastrophe rates in COS7 cells, and explore the effect of catastrophe on network structure.

The tips of newly spawned tubules are tracked within COS7 cells (details in SI Appendix Methods). In addition to positional data, it is also recorded whether the growth is successful in fusing with a neighboring tubule (fused) or if it ultimately retracts (not fused). Using the position of tracked tips, the average velocity until fusion or until the time of retraction is calculated. The distribution of growth speeds is broad (Fig. 2.5A), with an average and standard deviation of 1.09 ± 0.75 μm/s, consistent with previous measurements [28, 82]. No significant differences in

the distribution are observed between tubules that successfully fuse and those that do not.

We next calculate the gap size that growing tubules must traverse in order to fuse, a quantity which differs between successful and unsuccessful spawning events (Fig. 2.5B). Here, gap size is the approximate diameter of the enclosing polygon ($d = 4A/P$, with A area and P perimeter, an exact formula for the inscribed diameter of regular polygons). On average, successful growth events traverse shorter gap sizes (2.1 ± 0.5 μm) than unsuccessful events (2.4 ± 0.5 μm). This effect can also be visualized by considering the success rate of newly spawned tubules, which decreases as a function of gap size (Fig. 2.5C).

An estimate for the catastrophe rate in living ER networks can be extracted by fitting the experimental success rate to $S(d) = e^{-\alpha d/v}$ (Fig. 2.5C). Here, d is the gap size, $v = 1.1$ μm/s is the average velocity of all measured growth events, and α is the catastrophe rate and fit parameter. This gives $\alpha_{\mathrm{ER}} = 0.25 \pm 0.04$ s^{-1}.

To explore how these events affect the steady-state structure of the network, we introduce a constant-rate (Poissonian) catastrophe process for each growing tubule in the liquid network simulations. A single parameter (α) controls the rate at which a growing tip ceases forward motion and begins to retract due to membrane tension. Simulations are performed with experimentally relevant choices for mobility and spawning rate ($b = 0.02$ μm/s, $k = 0.005$ μm^{-1}s^{-1}) across a wide range of catastrophe rates, and the steady-state structural properties of the network are analyzed.

At small catastrophe rates, the mean area of polygons in the network remains relatively unchanged from the case with no catastrophe (Fig. 2.5D). As the catastrophe rate increases, it becomes more likely that growing tubules will retract before fusing, especially across larger gaps. Thus, there are fewer splitting events of large areas, leading to an increase in mean area. The larger average gap size, in turn, leads to even fewer fusion events. As the catastrophe rate grows sufficiently large, the persistence length of growth events becomes smaller than the average gap they must traverse. Mean area is then expected to diverge beyond a critical catastrophe rate, as confirmed by simulations (Fig. 2.5D).

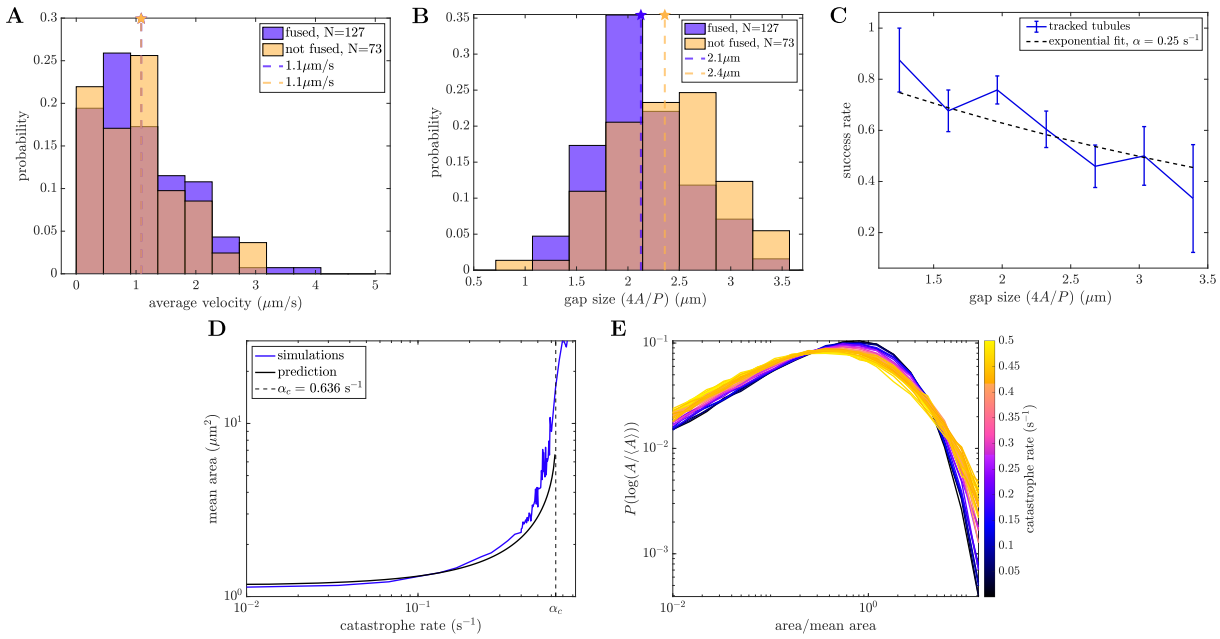

Figure 2.5. Growing tubules undergo catastrophe events that alter polygon size distributions. (A) Velocity distributions of growing tubules that lead to both successful and unsuccessful fusion. Mean of each distribution indicated by dashed line. (B) Distribution of gap sizes across which tubules are growing for both successful and unsuccessful fusion events. Mean of each distribution indicated by dashed line. $p = 0.001$ for a one-sided Student's t-test. (C) Success rate as a function of gap size d, with fit to $S(d) = e^{-\alpha d/v}$ indicated by dashed line. (D) Mean area grows as a function of catastrophe rate. Black line marks analytic prediction. Dashed vertical line shows predicted critical rate beyond which mean areas diverge. (E) Normalized area distributions for liquid networks with increasing catastrophe rates. High catastrophe rate leads to an enrichment of both small and large areas.

The average effect of catastrophe on steady-state structure in liquid networks can be analytically approximated by modifying Eq. 2.2 for the total network length to incorporate the success rate $S(d)$ of new growth events:

$$\frac{dL}{dt} = kL\lambda\sqrt{3}e^{-\sqrt{3}\alpha\lambda/v} - \gamma bn. \tag{2.10}$$

At steady state, this reduces to the following transcendental equation for λ,

$$\lambda^2 e^{-\sqrt{3}\alpha\lambda/v} = \frac{2\gamma b}{3\sqrt{3}k}. \tag{2.11}$$

The derivative of λ with respect to α approaches infinity at $\alpha_c = \frac{1}{e}(2\sqrt{3}k/\gamma b)^{1/2}$, indicating that no finite solution is possible above this critical catastrophe rate. For the simulation parameters used in Fig. 2.5D, the critical value is given by $\alpha_c = 0.64$ s^{-1}. Solving for λ numerically, the polygon mean area can be found as a function of catastrophe (black curve in Fig. 2.5D). The divergence of average area with increasing catastrophe rate is successfully predicted by this analytic model. Using this model for catastrophe (SI Appendix, Fig. S4), we additionally demonstrate that liquid networks can form quasi-stable architectures without a boundary or tethering to static structures, so long as there is sufficient growth to counteract the tension-induced shrinking.

Notably, the catastrophe process affects not only the average polygon area, but also the normalized distribution of areas (Fig. 2.5E). The altered distributions arise because catastrophes have a greater effect on large than on small polygons. Thus, normalized distributions for systems with frequent catastrophes have a fatter tail of large-area polygons that are unlikely to be split by a successful new tube fusion.

2.4 Discussion

We use a physical model of the peripheral ER as an active liquid network to capture its steady-state structural and dynamic properties. The behavior of liquid networks is effectively described by two main parameters, the junction mobility and tubule spawning rate. A characteristic network density and connectivity emerges from a balance between tubule creation and the contraction of small polygons. This model reproduces key geometric features of the peripheral ER in adherent mammalian cells, such as the typical shape and distribution of areas between tubules. We find that liquid networks are able to replicate physiological rearrangement timescales. Quantifying polygon dynamics in these systems allows us to derive the distribution of areas, thus forming a connection between emergent steady-state structure and the underlying, small-scale dynamics. Finally, by considering the effects of static tethering points and catastrophe of tubule

growth we explore how the cell can alter the effective junction mobility and tubule spawning rate to modulate network properties.

In this work, the complex protein-studded membrane structure of the peripheral ER is reduced to a spatial graph of junctions connected by one-dimensional, constant-tension, fluid-like edges. This highly simplified model is able to recapitulate much of the structural and dynamic properties of the living ER, while remaining agnostic to the specific details of membrane-shaping and dynamics at the nanometer scale. In reality, the effective tension driving the shortening of ER tubules could be modulated by varying tubule radii and by the distribution of tubule-stabilizing proteins such as the reticulons [92]. Both tubule radii and reticulon distributions are spatially heterogeneous across the network [21], potentially giving rise to tension gradients. Fluctuations in tension may also arise from cis-dimerization of membrane proteins such as atlastin [41]. More complicated ER structures, such as fenestrated sheets [80], may also influence the tension and hence the dynamics of the surrounding network. Furthermore, tubule spawning rate may be heterogeneous due to varying distributions of microtubules and motors. These effects may account for some of the spatial variability in ER density observed in cells [93].

An additional simplifying assumption inherent to the liquid network model is the ability of individual tubules to straighten on a timescale faster than the node rearrangements. While some bent tubules can be seen in the peripheral ER, their persistence length [70] is usually much longer than the typical polygon size. Thus the kinks that sometimes appear in long ER tubules are likely associated with connections to other cellular structures (analogous to the 'pinning points' discussed above). The constant, isotropic mobility coefficient for network nodes is another simplification of the model, neglecting the differences in friction associated with dragging a long tubule perpendicular to its axis, versus sliding a junction along the tubule membrane. Despite these simplifications, the liquid network model reproduces many aspects of ER structure and dynamics, helping to connect local rearrangements to the large-scale architecture of the network.

The model presented here is most relevant for two-dimensional network structures such as those observed in the peripheral ER of adherent COS7 cells. In many other cell types, the ER

forms three-dimensional networks. Such networks require an additional length scale defined by the range within which a growing tubule tip can contact and fuse into the rest of the network. This additional length scale alters the dependence of network density on the kinetic parameters b, k. While we demonstrate some basic scaling behaviors of 3D liquid networks in the SI Appendix, more detailed exploration of these networks is left for future work. Further high-resolution imaging and quantification of 3D ER network architecture will also be necessary to probe the validity of the liquid network model in 3D.

Alternative 3D models can also give rise to network-like structures. In particular, microemulsions of lipids, water, and surfactants can form bicontinuous cubic phases whose density is governed by the relative concentrations of the components [75, 74]. Such structures coexist with lamellar phases, with the balance modulated by the curvature preferences of the lipid layers [75]. These models may be particularly relevant for understanding the transition of the ER between network-like and sheet-like structures, which can be tuned by changing the distribution of preferred membrane curvatures [69]. While our liquid network model focuses on structures emerging through tension and growth, future work comparing the resultant dynamics and architecture to networks arising via phase transition may prove informative. In particular, such connections may shed light on *in vitro* observations of ER network formation in the absence of cytoskeletal filaments needed for new tubule extension [94].

Maintaining an organelle as an active, dynamic liquid network incurs a continuous energy cost for the cell. In particular, motor activity or driven microtubule polymerization is required to grow new tubules that split polygons and interrupt coarsening. Given that individual kinesin motors burn one ATP molecule per 8-nm step [95], we would expect the rate of energy consumption associated with network maintenance to scale as $\left(\sqrt{2\gamma/\sqrt{3}}\right) Lk\ell/ds$, where L is the total network length, $\ell = \sqrt{b/k}$, ds is the motor step size, and γ is the scaling factor relating average polygon area to ℓ^2. For the cells considered here this would amount to roughly 2×10^3 ATP/sec. Notably, this maintenance cost is orders of magnitude lower than the estimated energy consumption ($\sim 10^8$ ATP/sec) associated with synthesizing the proteins shipped from the ER in

the secretory pathway [96, 97, 98].

For this modest energetic cost, the dynamic network of the ER provides the cell with a number of functional benefits. As a topologically isolated space with high calcium concentration, the ER provides a compartment for the efficient folding of proteins destined for the extracellular environment [68, 2]. Its dense network structure enables the rapid and proximal delivery of calcium ions into the cytoplasm [4] during localized signaling events known as puffs or sparks [99]. The well-connected network architecture also allows for rapid search by newly folded proteins to encounter exit sites in the ER [93]. Furthermore, the density of the network makes it possible for the ER to form a plethora of contact sites for the transport of proteins, lipids, and ions to and from other organelles such as mitochondria and endo/lysosomes [32, 36, 31, 100].

The dynamic rearrangements of the network could allow for rapid structural response of the ER to local and global perturbations. For example, the increased network density associated with pinning points may aid the accumulation of ER tubules near mitochondrial contact sites, where the ER is known to play an important role in mitochondrial fission and fusion [101, 32]. Network dynamics could also allow the ER to restructure around rearranging organelles or in response to cytoplasmic deformation in motile cells [102].

The interplay between microtubules and peripheral ER [103] enables the network to maintain its structure against tension. Suppression of motor proteins that drive tubule extension results in retraction of the ER network from the cell periphery [104]. In addition, depolymerization of microtubules following nocodazole treatment leads to the withdrawal of peripheral ER tubules and an increase in perinuclear ER sheets and cisternae [105]. By maintaining the ER in a state of constant tension, poised on the verge of retraction, and controlled by driven extension along the cytoskeleton, the cell ensures that its structure can respond rapidly to changing cues. Such mechanical response may partly underlie the ability of the ER to restructure rapidly during mitosis, when it undergoes a global tubule-to-sheet conversion [106, 107].

The liquid network model not only accounts for the unique reticulated structure of the ER but also demonstrates how this architecture can emerge from and be regulated by a balance

of two simple dynamical processes: tension-driven coarsening and new tubule growth.

2.5 Materials and Methods

2.5.1 Liquid network simulations

To simulate liquid networks, the overdamped Langevin equation for network nodes (Eq. 1) is integrated forward in time using a fourth-order Runge-Kutta method implemented in Fortran 90.

After updating junction positions in each time step dt, the code checks for connected nodes which are within some threshold distance of each other, defined to be $dx = \max(\sqrt{Ddt}, bdt)$, where D is the diffusivity and b the mobility of the nodes. The threshold distance is thus comparable to the typical distance a node moves per timestep, with values typically in the range of $dx = 10^{-4} - 10^{-3}$ μm. The model is insensitive to the specific choice of threshold (Fig. S2D-F).

For connected nodes within the threshold distance, the length of all possible rearrangements of the neighbors is calculated, to determine which configuration minimizes the connected length (Fig. 1D). The minimal configuration is chosen, and edges accordingly undergo their small rearrangements. Rearrangements are taken to occur within a single timestep, consistent with the observation that rearrangement at ER junctions occurs at sub-second timescales, much faster than the time to grow or shrink a polygon.

Next, the code checks for fusion of actively growing tubule tips with existing edges by finding any crossings that may have occurred. Upon identification of a crossing event, the tubules fuse and form a stable junction node (Fig. 2.1D). Finally, the code samples from a Poisson distribution with rate k to determine the number of new tubule spawning events occurring in the current time step dt, given the current network length (excluding boundary edges). Novel spawning events occur uniformly distributed across all non-boundary edges of the network. Thus concludes one cycle of the simulation, after which the code iterates to update junction

positions. Unless stated otherwise, a time step of $dt = 0.01$ s is used, the initial configuration is a honeycomb network, and the simulation is run until steady state has been reached (as defined by the stabilization of total network length over time).

To avoid runaway growth or full collapse of the membrane, all simulations are enclosed within a circle of radius 14 μm defined by fixed immobile junctions connected via boundary edges. When a tubule growth event fuses with a boundary edge, the resulting boundary junction behaves exactly the same as junctions in the bulk except its motion is restricted to the perimeter of the boundary circle. Neighbor rearrangements and loop closure can still occur, resulting in a net balance of boundary junctions over time. The circular boundary is taken to represent the plasma membrane, which is known to make direct contacts with the peripheral ER network.

Extensions to the model include random static pinning and unpinning of bulk nodes, and the catastrophe process for tubule growth, all modeled as random Poisson distributed processes. Pinning of nodes occurs with rate k_p (s^{-1}), and unpinning of nodes occurs with rate k_u (s^{-1}). This pinning and unpinning is performed at the end of each simulation cycle. Catastrophe of each growing tubule occurs with rate α (s^{-1}). Catastrophe events are sampled every cycle after checking for tubule fusion. Boundary-free simulations are also performed, typically with a finite catastrophe rate for growing tubules. See Sec. A.1 for model details in three dimensions.

We obtain spatial network structures over time from these simulations in the form of node positions and edge connectivity. To analyze the properties of minimal loops or polygons in the two-dimensional network structures, we use publicly available code written in Matlab [108].

2.5.2 Cell culture and imaging

COS7 cells (ATCC-CRL-1651) and U2OS cells (ATCC-HTB-96) were grown in Dulbecco's modified Eagle's medium (DMEM) supplemented with 10% fetal bovine serum (FBS) and 1% penicillin/streptomycin. Prior to imaging experiments, COS7 cells were seeded in six-well, plastic bottom dishes at a density of 150,000 cells per well, about 16 hours prior to transfection of DNA plasmids. The mCh-KDEL and KDEL-venus were described previ-

ously [109] and were transfected at a standard amount of 0.2 µg for all experiments. Plasmid transfections were performed 24 hours prior to imaging with plasmid DNA in Opti-MEM (Invitrogen) with 5 µL of Lipofectamine 3000 reagent (Invitrogen) according to the manufacturer's instructions. After 5 hours of transfection, cells were seeded in 35 mm glass-bottom microscope dishes (MatTek).

All imaging experiments were performed at the Van Andel Institute Optical Microscopy Core on a Zeiss LSM 880, equipped with an Axio Observer 7 inverted microscope body, stage surround incubation, Airyscan detector, two liquid-cooled MA_PMT confocal detectors, and one 32-channel GaAsP array confocal detector. Images were acquired with a Plan-Apochromat 63x (NA 1.4) oil objective with 3x optical zoom using Zeiss Zen 2.3 Black Edition software. Cells were tracked for at least 2 minutes with constant acquisition (200 ms or 316 ms).

2.5.3 Image analysis

Extracting networks from live cell images

The machine learning segmentation toolkit ilastik [110] is used to segment ER network structures from live-cell images using the KDEL_Venus or mCherry_KDEL markers. A network structure is extracted from the probability file output by ilastik using custom code for skeleton tracing in Matlab [111]. This code is publicly available at https://github.com/lenafabr/networktools and includes data structures for storing the network as a set of nodes connected by edges with curved spatial paths.

Estimating the tubule spawning rate in living cells

All new tubule spawning events are manually counted within cropped subregions (6.3×6.3 µm) of the peripheral ER from 19 cells over the course of 40 s (Video S2.5). The number of tubule spawning events is then normalized by the average network length over all frames (as obtained via ilastik and Matlab skeletonization, see above) and the total time considered. This yields an estimate for the average tubule spawning rate, k, (units of $\mu m^{-1} s^{-1}$) in each cell.

Extracting polygons from experimental ER images

The machine learning segmentation toolkit ilastik [110] is used to accurately identify polygons in experimental images of ER networks (7 COS7 cells and 2 U2OS cells). First, images are segmented as before using the pixel classification capabilities of ilastik. Then, an object classification model is trained to identify polygons in the cell periphery using the previously generated probability file and raw image as input. Associated geometric and spatial properties of these polygons are then analyzed in Matlab.

Semi-automated tracking of new tubule growth events

Network structures are extracted from images of COS7 cells, and all degree-1 (terminal) nodes are identified. The positions of these nodes and the length of their connected edges are calculated. The terminal nodes are then tracked over time using conventional particle tracking software [85] where the particle 'amplitude' is set by the connected edge length. Tracks within 1 μm of the network boundary or with track length less than 3 frames are discarded. The tracks are manually verified and adjusted as necessary using a custom-built Matlab GUI that superimposes track data on top of image files. The fate of the growing tubule (whether or not it successfully fuses into the network) is manually identified. A total of 200 tubule tip trajectories are quantified for Fig. 6.

The average velocity is found by dividing the maximum distance a tubule travels from its spawning point by the time it takes to get there. For successfully fused tubules, this is simply the distance from spawning to fusion; for unsuccessful spawning events, it is the distance from spawning to the turnaround or catastrophe point. The area and perimeter of the polygon containing the spawning event are calculated for each tracked frame. The gap size is estimated as $d = 4A/P$ and is averaged over the whole track.

2.5.4 Quantifying network rearrangement

Edge mean minimal distance

Both simulated and experimental networks are meshed into 0.03 μm segments, and for each point on subsequent networks, the minimal distance to a point on the starting network is found. The edge mean minimal distance (EMMD) is the mean of all such distances. To extract a timescale from the experimental data, the EMMD versus time curve is fit with a double exponential function of the form $f(x) = c_1(1-e^{-t/c_2}) + c_3(1-e^{-t/c_4})$. The longer timescale (e.g. $c_2 \gg c_4$) is chosen as the representative EMMD timescale for each experimental network. Simulated data does not exhibit the same short timescale jump as experimental because there are no localization errors or network segmentation artifacts. Thus, only a single exponential (e.g. the first term of $f(x)$) is fit to the simulated EMMD curves, giving the extracted EMMD timescale for each simulated network.

Polygon growth rates

Experimental polygon positions and areas are extracted from ilastik segmented images (see above). Matlab File Exchange code for extracting minimal loops from graphs is used to find polygons in simulated networks [108]. Polygons are tracked over time using conventional particle tracking software [85]. For each tracked polygon, we also perform a change point analysis of the tracked area over time using Matlab's findchangepts function [111]. This enables identification of additional splitting events that may have been missed by the tracking software. The tracks are broken up at the change-points, allowing for robust tracking of polygon growth and shrinking dynamics between split events.

From these tracks, the area rate of change over 3 s intervals is calculated in both experiments and simulations after applying a lowess smoothing filter with span 3 s. Only tracks longer than 4s are analyzed. The normalized growth rate is obtained by dividing the extracted growth rate by the average area of all tracked polygons in that cell or simulation run. In order to collapse together simulations with different parameter values, we multiply the simulated growth rate data

by the intrinsic network timescale $\tau = (bk)^{-1/2}$, yielding a non-dimensionalized growth rate.

The mean and standard error of the mean of normalized growth rate are calculated within bins of normalized polygon area (green points in Fig. 4E, F). This provides an estimate for the average growth and shrinking behavior for polygons as a function of their area within liquid networks and the ER. The binned mean growth rates are then fitted to Eq. 4. For simulation data, β, g, h are the fitting parameters, whereas for experimental data we fix $\beta = 0.78$ (the scaling exponent obtained from the simulation fits) and only fit g, h. In both cases, the data is resampled 2000 times to estimate the error in the fitting parameters, assuming normally distributed values with mean and standard deviation obtained from binned values.

2.6 Acknowledgements

Chapter 2, in full, is a reprint of the material with minor edits as it will appear in Zubenelgenubi C. Scott, Samuel B. Steen, Greg Huber, Laura M. Westrate, and Elena F. Koslover. "The Endoplasmic Reticulum as an Active Liquid Network." Proceedings of the National Academy of Sciences, (2024)

Chapter 3

Diffusive Search and Trajectories on Tubular Networks: a Propagator Approach

3.1 Abstract

Several organelles in eukaryotic cells, including mitochondria and the endoplasmic reticulum, form interconnected tubule networks extending throughout the cell. These tubular networks host many biochemical pathways that rely on proteins diffusively searching through the network to encounter binding partners or localized target regions. Predicting the behavior of such pathways requires a quantitative understanding of how confinement to a reticulated structure modulates reaction kinetics. In this work we develop both exact analytical methods to compute mean first passage times and efficient kinetic Monte Carlo algorithms to simulate trajectories of particles diffusing in a tubular network. Our approach leverages exact propagator functions for the distribution of transition times between network nodes and allows large simulation time steps determined by the network structure. The methodology is applied to both synthetic planar networks and organelle network structures, demonstrating key general features such as the heterogeneity of search times in different network regions and the functional advantage of broadly distributing target sites throughout the network. The proposed algorithms pave the way for future exploration of the interrelationship between tubular network structure and biomolecular reaction kinetics.

3.2 Introduction

Diffusive transport in geometrically complex environments underlies a broad variety of biophysical phenomena, ranging from transcriptional regulation in the nucleus [42, 43], to reactions inside organelle structures [44, 45], to intercellular communication through a variety of channel and bridge arrangements [46]. The morphology of the confining environment is known to fundamentally alter the kinetics of diffusion-limited chemical reactions, switching between compact and non-compact search processes depending on the effective dimensionality of the domain [47, 112]. Multimolecular reaction systems such as phosphorylation cascades may acquire novel dynamic behaviors such as ultrasensitivity and bistability depending on the degree of confinement [49, 50].

A particularly important class of confined diffusion processes occurs on network structures, which have been used to describe porous media [57, 58], neuronal trees [56], and organelle morphologies [55, 39]. These 'spatial networks' are characterized by nodes and edges embedded in physical space, a restriction which limits the network topology. Encompassing a broad variety of transport and communications networks, spatial networks have limited node degree, with each node connected only to a handful of neighbors in close physical proximity [59]. There is an extensive body of literature on characterizing the behavior of random walks on general networks (see [113] for a review). Many studies focus on systems where particles exhibit a well-defined hopping time across each edge, with hops treated either as discrete time steps [60, 61] or as constant-rate Poisson processes [63, 62]. Others allow for generalized distributions of hop times that are nevertheless uniform throughout the network [114, 115]. Recently, a general theory for heterogeneous continuous-time random walks on networks has been developed [64], which incorporates transition times with arbitrary distributions that are specific to each node. A similar approach has previously been applied, modeling transitions on a network of states embedded in an energy landscape [116].

Particles diffusing along the edges of a network exhibit a broad range of inter-node

transition times, whose distribution is dependent on the edge length. Prior work focusing on simple networks of tubes and containers [117], as well as planar networks resembling percolation clusters [45], highlighted the importance of edge length in overall search times on the network. Here, we develop mathematical methodology for computing reaction mean first passage times (MFPT) on arbitrary spatial networks, with diffusion incorporated as a concrete physical transport process along each edge. Whereas past work on diffusive processes simplified individual node transitions to a single effective rate constant [63, 62], we explicitly incorporate the edge-length-dependent distribution of transition times, bridging local diffusive particle dynamics and large-scale transport on spatial networks.

For many reaction-diffusion systems, the behavior of interest requires quantities beyond the mean first passage time and other low-order moments of the first-passage distribution. For example, biochemical processes may rely on extreme value statistics that dictate the time-scales for the first of many signaling particles to reach a target [65]. Activation cascades can be modulated by processive rebinding processes wherein one enzyme can return repeatedly to the same target after its first encounter [49]. Targets that themselves undergo diffusive motion are prevalent in most biomoleculear reaction systems. Modeling of these more complex processes requires moving beyond analytically tractable methods to leverage stochastic simulations of diffusing particles on network structures.

A family of agent-based simulation methods, known as kinetic Monte Carlo [66] or Green's function reaction dynamics [118, 119] are particularly well suited for simulating sparse populations of particles diffusing in complex geometries. These methods rely on analytically determined propagator functions to evolve individual particles within 'protective domains' – regions where they do not come in contact with other particles. By sampling from an appropriate propagator, such simulations allow time steps that are tuned to the local structure of the domain, minimizing the computational time involved in propagating a particle through empty space. Several general propagators have been developed for three-dimensional regions [120], and this approach has been employed for simulating systems such as kinase cascades [49], target search

by DNA-binding proteins [43], and multi-modal transport of peroxisome vesicles in fungal hyphae [121]. In this work we develop exact analytical propagators for the passage of diffusing particles between network nodes. By allowing for step sizes comparable to the local edge length, these propagators enable simulations that can be run much more efficiently than classical Brownian dynamics. We thus present an efficient propagator-accelerated algorithm optimized for stochastic simulations of diffusing particles confined in spatial networks.

We focus specifically on tubular networks similar to those formed by intracellular reticulated organelles. The peripheral endoplasmic reticulum is one such network; it forms a dynamic web of interconnected tubules with a topologically continuous lumen, spread throughout the cell periphery[9]. The ER hosts a variety of biochemical reaction pathways and plays a crucial role in calcium dynamics, lipid delivery, and protein synthesis and quality control [122]. Another reticulated organelle structure is formed by the fusion of mitochondria in yeast and many mammalian cell types [123, 124]. Mitochondrial network structures share many topological features with geographical transportation networks [55] and are thought to reside in the percolation regime, exhibiting just barely enough connectivity to form a large cell-spanning connected cluster [124]. The functional role of mitochondrial network formation remains a topic of much debate [125], but is thought to include complementation of mtDNA defects [126], quality control through selective fusion and mitophagy [127, 128], and enhanced energy transmission [129].

In both the ER and mitochondrial networks, critical biomolecular reactions require individual diffusive components to find each other within the extensive network architecture. Some functions, such as the packaging of newly synthesized secretory proteins into ER exit sites or the regulation of transciption in mitochondrial nucleoids, rely on proteins reaching relatively stationary punctate target sites in the network. Although some recent evidence indicates the possibility of directed transport for ER luminal proteins driven by local fluid flow [130], the major form of transport within organelle networks is still believed to be diffusive.

In this work, we develop new algorithms for quantifying target search and reaction kinetics inside tubular network structures similar to those exhibited by reticulated cellular

organelles. Specifically, our approach is well suited to spatial networks with well-defined edge lengths and low node degrees (typically 3 or less for ER [39] and mitochondrial networks [55]). Furthermore, we rely on the simplifying assumption that motion along tubular edges, rather than trapping at voluminous nodes, dominates diffusive transport times. Our overarching goal is to be able to accurately compute the distribution of search and encounter times for diffusive particles within network morphologies. To this end, we employ both analytical methods to extract low-order moments (mean and variance) of the search times, as well as describing an efficient algorithm for agent-based stochastic simulations that can incorporate mutually reactive diffusing particles. The result is a mathematical framework optimally suited for modeling the kinetics of a broad variety of molecular processes confined in tubular networks.

3.3 Model development and transition time distributions

We consider the diffusive motion of particles on a network embedded in physical space. Specifically, the network structure consists of point-like nodes $(i, j, \ldots)$, connected by one-dimensional edges of length ℓ_{ij}. The edges can be curved, and thus longer than the Euclidian distance between the connected nodes, but can only connect to other edges at a node.

Particles diffuse in one dimension along these edges, with diffusivity D. They do not spend any finite time trapped at the nodes themselves, which serve merely as point-like edge intersections. A particle that starts at such an intersection will diffuse around the edges adjacent to that node (a 'node neighborhood') until it hits an adjacent node. It will then continue to diffuse in the neighborhood of the new node. We can thus consider the particle as moving from neighborhood to neighborhood with a certain distribution of transition times between adjacent neighborhoods. It is important to note that the current neighborhood of a particle is defined not by the edge on which it is located but rather by the last node that it has crossed (Fig. 3.1). With this definition, the motion of the particle can be treated as a Markov state model [131], with each Markov state corresponding to a neighborhood. Transitions between neighborhoods are

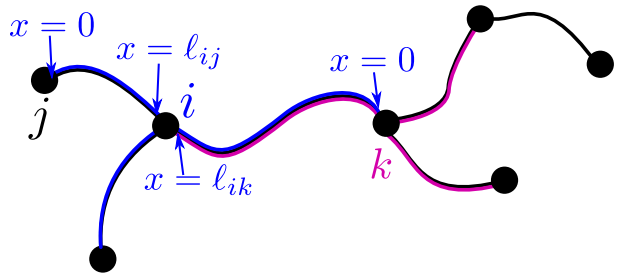

Figure 3.1. Model schematic, showing small section of an example network. Blue lines show the neighborhood of node i; magenta lines show the neighborhood of node k. The coordinate system for two edges within neighborhood i is labeled, with x going from 0 (at adjacent node) to ℓ_{ij} (at node i itself).

memoryless – once a particle hits a given node, its subsequent distribution is no longer dependent on the previous nodes it has passed through. However, unlike prior applications of Markov state models [131] or 'discrete path sampling' [62, 132] in the context of molecular rearrangements, the transition times between states are not Poisson distributed. Instead, this model falls in the category of heterogeneous continuous time random walks, which can be analyzed on arbitrary networks for arbitrary distributions of transition times [64].

To quantify the behavior of such a system, we need to know the local transition time distribution $P_{ik}(t)$, which gives the probability density that a particle which starts at node i at time 0 will first hit an adjacent node k between time t and $t+dt$, without first reaching any other nodes in the meantime. We note that in contrast to previous analyses of random walks on networks [113, 64], the distribution of waiting times to leave the neighborhood and the splitting probability of which node is next encountered are not independent random variables (*i.e.* the conditional distribution of first passage times differs depending on which of the adjacent nodes is reached first). To calculate the local transition time distributions, we generalize a well-known approach for finding the flux of diffusive particles to the edges of a linear segment with absorbing boundaries [133]. A one-dimensional coordinate system ($0 \leq x \leq \ell_{ik}$) is placed along each edge attached to node i, with $x = 0$ corresponding to node k and $x = \ell_{ik}$ corresponding to the junction node i where the particle starts (see Fig. 3.1).

Along each edge ik of the neighborhood, the Green's function distribution $c_{ik}(x,t)$ of a

diffusing particle obeys the usual diffusion equation:

$$\frac{\partial c_{ik}}{\partial t} = D\frac{\partial^2 c_{ik}}{\partial x^2}, \tag{3.1a}$$

$$c_{ik}(x,0) = \frac{1}{d_i}\delta\left(x-\ell_{ik}\right), \tag{3.1b}$$

$$c_{ik}(0,t) = 0, \tag{3.1c}$$

where d_i is the degree of the i^{th} node in the network. Equation 3.1b gives the initial condition, indicating that the particle distribution is concentrated in a Dirac-delta function at the junction node. Equation 3.1c gives the boundary conditions, with each neighboring node treated as an absorbing boundary. The transition time distibution function is then given by the flux into each of these boundaries:

$$P_{ik}(t) = D\left.\frac{\partial c_{ik}}{\partial x}\right|_{x=0}. \tag{3.2}$$

Integrating each P_{ik} over time gives the probability that a particle will hit adjacent node k before any other (ie: the splitting probability from node i). An additional boundary condition at each edge is set by enforcing continuity of the particle distribution function at the junction node: $c_{ik}(\ell_{ik},t) = c_{ij}(\ell_{ij},t)$, for all adjacent nodes k, j.

Equation 3.1 can be solved by way of a Laplace transform $t \to s$, which gives the following equation for the transformed Green's function $\widehat{c}_{ik}$

$$s\widehat{c}_{ik} - c_{ik}(t=0) = D\frac{\partial^2 \widehat{c}_{ik}}{\partial x^2}. \tag{3.3}$$

The homogeneous solution is

$$\widehat{c}_{ik}(x,s) = A\sinh(\alpha x)\prod_{j\neq k}\sinh\left(\alpha\ell_{ij}\right), \tag{3.4}$$

where $\alpha = \sqrt{s/D}$, loo and the product is over all edges attached to node i, other than edge k. The prefactor A is set by the initial condition, and can be found by integrating Eq. 3.3 over an infinitesimally small interval around the junction node. This gives

$$\begin{aligned} -1 &= -D \sum_{k=1}^{d_i} \left. \frac{\partial \widehat{c}_{ik}}{\partial x} \right|_{\ell_{ik}}, \\ A &= \frac{1}{\alpha D} \left(\prod_{j=1}^{d_i} \sinh \alpha \ell_{ij} \right)^{-1} \left(\sum_{k=1}^{d_i} \coth \alpha \ell_{ik} \right)^{-1}, \end{aligned} \tag{3.5}$$

where the sums and products are over all edges attached to node i. Finally, the flux to the absorbing boundaries is given by

$$\widehat{P}_{ik} = \left(\sinh \alpha \ell_{ik} \sum_{j=1}^{d_i} \coth \alpha \ell_{ij} \right)^{-1} \tag{3.6}$$

Equation 3.6 gives the Laplace-transformed distribution of times for a particle starting at junction node i to first reach adjacent node k without hitting any other neighboring node. We can also define the survival time distribution $Q_i(t)$—the probability that the particle has not reached any of the neighboring nodes by time t. Its Laplace-transformed form is:

$$\widehat{Q}_i = \frac{1 - \sum_{k=1}^{d_i} \widehat{P}_{ik}}{s} \tag{3.7}$$

Expanding around $s = 0$ gives the splitting probability to each neighboring node (P_{ik}^*) and the overall average waiting time (Q_i^*) before the particle hits one of the neighboring nodes. Specifically,

$$P_{ik}^* = \lim_{s \to 0} \widehat{P}_{ik}(s) = \frac{1/\ell_{ik}}{\sum_{j=1}^{d_i} 1/\ell_{ij}} \tag{3.8a}$$

$$Q_i^* = \lim_{s \to 0} \widehat{Q}_i(s) = \frac{1}{2D} \cdot \frac{\sum_{j=1}^{d_i} \ell_{ij}}{\sum_{j=1}^{d_i} 1/\ell_{ij}} \tag{3.8b}$$

The next higher-order term for small s can be used to calculate the variance in the transition time to one of the neighboring nodes (see Sect. 3.4.1).

The above expressions enable propagation of particles that start specifically on a node to the neighboring nodes. In many applications it is useful instead to consider particles that start distributed along the edges of the network. Such a particle must first be propagated to one of the nodes bounding that edge, after which its behavior can again be described by the node-to-node propagator (Eq. 3.6.) For a particle starting at position x_0 along edge m, of length ℓ_m, the Laplace-transformed flux to either of the two boundaries has the well-known form [133]

$$j_- = \frac{\sinh\left[\alpha(\ell_m - x_0)\right]}{\sinh\left[\alpha\ell_m\right]}, \quad j_+ = \frac{\sinh\left[\alpha x_0\right]}{\sinh\left[\alpha\ell_m\right]}. \tag{3.9}$$

If the particle starts uniformly distributed along edge m, the corresponding flux to each of the bounding nodes ($\widehat{P}_{mj}^{(E)}$) and the survival probability on the edge ($\widehat{Q}_m^{(E)}$) are given by

$$\begin{aligned} \widehat{P}_{mj}^{(E)} &= \frac{1}{\alpha\ell_m}\tanh\left(\frac{\alpha\ell_m}{2}\right) \\ \widehat{Q}_m^{(E)} &= \frac{1}{\alpha^2 D}\left[1 - \frac{2}{\alpha\ell_m}\tanh\left(\frac{\alpha\ell_m}{2}\right)\right]. \end{aligned} \tag{3.10}$$

Expanding around $s = 0$ gives the trivial splitting probability for a particle starting uniformly on the edge: $P_{mj}^{(E*)} = 1/2$, and the average waiting time to leave the edge:

$$\widehat{Q}_m^{(E*)} = \ell_m^2/(12D) \tag{3.11}$$

The splitting probabilities and survival times enable the calculation of mean first passage times on the network (Sect. 3.4). In order to sample from the full distribution of transition times, an inverse Laplace transform must be applied to the propagators in Eqs. 3.6 and 3.10, as discussed in Sect. 3.5.

3.4 Computing mean and variance of first passage times

3.4.1 Diffusion-limited reactions

We next present an analytic approach for calculating low-order moments of the reaction time distribution for particles that react instantaneously upon reaching a set of target nodes in the network. We note that the derivation in this section largely reiterates previously published work [64, 116, 45], but is presented here for completeness and consistency of notation.

The probability that a particle starting at node i at time 0 is in the neighborhood of node j at time t is defined by $G_{ij}(t)$. The Laplace-transformed form of this propagator has been previously derived, both for general continuous-time random walks on networks [64] and for specific applications involving diffusive motion of particles in interconnected tubules [45] or over multi-state energy landscapes [116, 132]. It can be expressed as

$$\widehat{G}_{ij} = \left[\left(\mathbf{I} - \widehat{\mathbf{P}}\right)^{-1}\right]_{ij} \widehat{Q}_j, \tag{3.12}$$

where the elements of matrix $\widehat{\mathbf{P}}$ are given by Eq. 3.6 if two nodes are connected by an edge in the network, and are zero otherwise. The propagator $G_{ij}(t)$ gives the probability that the particle last hit node j sometime before time t and has not yet left the neighborhood of that node.

To calculate the distribution of first passage times to any set target of nodes $\{k\}$ in the network, we treat those nodes as being perfect absorbers. That is, whenever the particle first hits node k, it instantaneously vanishes from the network. The case of finite reaction rates in localized network regions is treated separately in the next section. We remove all rows and columns corresponding to the target neighborhoods from the matrix $\widehat{\mathbf{P}}$ as well as the vector $\widehat{\vec{Q}}$. As a result, the time a particle spends in the neighborhood of any network node is not altered, but when the particle leaves that neighborhood by moving to a target node, it is removed entirely from the network rather than continuing to propagate further [116, 45]. The survival probability that a particle starting at node i has not left the network by time t is $H_i(t) = \sum_{k=1}^{N} G_{ik}(t)$, where

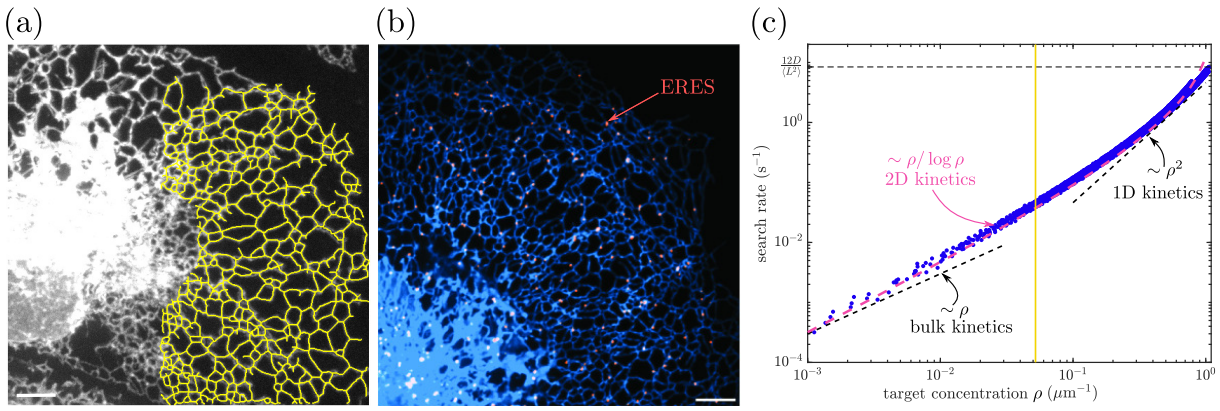

Figure 3.2. Target search rate on peripheral ER networks. (a) Network structure (yellow) extracted from confocal image of the COS7 cell peripheral ER network. (b) Peripheral ER network (blue) and ER exit sites (red, marked by fluorescently labeled Sec23a, a COPII protein). Scale bars in (a) and (b) are 5μm. (c) Dependence of search rate (inverse of mean first-passage time) on target concentration (per tube length) in nine distinct ER network structures. Each dot shows the average over 100 realizations of a fixed number of target nodes uniformly distributed over a single network structure. Black dashed lines indicate appropriate scaling for mass-action kinetics ($\sim \rho$) and one-dimensional search rates($\sim \rho^2$). The pink dashed line indicates expected behavior for two-dimensional kinetics [$k = D\rho_{2D}/\log(a\sqrt{\rho_{2D}})$, where a is taken as average ER edge length and ρ_{2D} is the two-dimensional target concentration]. Horizontal dotted line shows limiting case of average search rate on a network composed entirely of target nodes. Yellow line gives ERES density extracted from (b). Particles are assumed to have a diffusivity of $D = 1\mu m^2/s$.

the summation is over all nodes on the network. For particles initially distributed over nodes, with V_i the probability of starting at node i, the survival probability is given by the following matrix expression:

$$\widehat{H}(s) = \overrightarrow{V} \cdot \left(\mathbf{I} - \widehat{\mathbf{P}}\right)^{-1} \cdot \widehat{\overrightarrow{Q}}. \tag{3.13}$$

The central inverted matrix is a normalized form of a weighted discrete Laplacian over the network, which is used in a broad class of problems involving random walks on networked structures [64, 113].

A natural extension is to consider particles starting on the edges of the network, with probability W_m of starting (uniformly distributed) along edge m. In this case, the Laplace-

transformed survival probability can be expressed as

$$\widehat{H}^{(E)}(s) = \overrightarrow{W} \cdot \left[\widehat{\overrightarrow{Q}}^{(E)} + \mathbf{P}^{(E)} \cdot \left(\mathbf{I} - \widehat{\mathbf{P}} \right)^{-1} \cdot \widehat{\overrightarrow{Q}} \right]. \tag{3.14}$$

Here, the first term represents particles that never leave their initial edge and the second term includes a propagator for moving from the edge to one of its bounding nodes, convolved with the propagators for moving across all node-to-node paths through the network, and finally the survival probability of remaining at some final node neighborhood. Columns of $\widehat{\mathbf{P}}^{(E)}$ corresponding to target nodes are again removed from the matrix. The elements of $\widehat{\mathbf{P}}^{(E)}$ and $\widehat{\overrightarrow{Q}}^{(E)}$ are given in Eq. 3.10.

Regardless of whether particles start on nodes or edges of the network, the mean first passage time to encounter the set of targets is given by

$$\tau = \lim_{s \to 0} \widehat{H}(s), \tag{3.15}$$

which can be evaluated directly with the aid of Eq. 3.8a, 3.8b, and 3.11. Similarly the variance in the time to find a target is given by

$$\sigma^2 = \langle \tau^2 \rangle - \langle \tau \rangle^2, \tag{3.16}$$

where

$$\langle \tau^2 \rangle = -2 \left. \frac{\partial \widehat{H}}{\partial s} \right|_{s=0}. \tag{3.17}$$

From this, the mean square first passage time is expressed as

$$\begin{aligned} \langle \tau^2 \rangle = -2 \overrightarrow{V} \cdot \Bigg[& \left(\mathbf{I} - \widehat{\mathbf{P}} \right)^{-1} \cdot \frac{\partial \widehat{\mathbf{P}}}{\partial s} \cdot \left(\mathbf{I} - \widehat{\mathbf{P}} \right)^{-1} \cdot \widehat{\overrightarrow{Q}} \\ & + \left(\mathbf{I} - \widehat{\mathbf{P}} \right)^{-1} \frac{\partial \widehat{\overrightarrow{Q}}}{\partial s} \Bigg], \end{aligned} \tag{3.18}$$

where the derivatives of $\widehat{\mathbf{P}}$ and $\widehat{\vec{Q}}$ are

$$\left.\frac{\partial \widehat{P}_{ik}(s)}{\partial s}\right|_{s=0} = -\frac{1}{6D}\left(\frac{\ell_{ik}}{\sum_j 1/\ell_{ij}} + \frac{2/\ell_{ik}\left(\sum_j \ell_{ij}\right)}{\left(\sum_j 1/\ell_{ij}\right)^2}\right) \tag{3.19a}$$

$$\left.\frac{\partial \widehat{Q}_{i}(s)}{\partial s}\right|_{s=0} = -\frac{1}{24D^2}\left(\frac{\sum_j \ell_{ij}^3}{\sum_j 1/\ell_{ij}} + \frac{8\left(\sum_j \ell_{ij}\right)^2}{\left(\sum_j 1/\ell_{ij}\right)^2}\right). \tag{3.19b}$$

Example: target search times in the endoplasmic reticulum

As an example application of the calculations above, we consider network structures extracted from confocal images of the peripheral endoplasmic reticulum in COS7 cells. A data set of 9 peripheral ER images, obtained as described in prior work [45], was used to extract tubular network structures (Fig. 3.2a; details in B.2). For these biologically important tubular networks, we consider how the distribution of times to find target nodes varies with the target concentration. This question is particularly important in the context of the early secretory pathway. Proteins destined for secretion are co-translationally inserted into the ER membrane or lumen, undergo folding and quality control [68, 134], and must leave the ER through punctate ER exit sites (ERES). These ERES are largely immobile sites scattered throughout the network [37] (Fig. 3.2b) and proteins are assumed to diffuse to one of these sites for capture and packaging into vesicles that enable them to leave the ER and proceed to further steps of secretory processing [135, 136].

It is interesting to consider what ERES density is sufficient to enable diffusing proteins to rapidly encounter exit sites. In a three-dimensional continuum, reaction rates are proportional to the concentration of the target. However, in a geometry that is less than or equal to two-dimensional, the usual assumption of mass-action kinetics ceases to hold, and we expect a steeper dependence of rates upon target concentration [47].

For each individual ER network structure, we randomly distribute different numbers of target nodes across the network and compute the mean first passage time (MFPT) for a diffusive particle to first hit a target. The particles are assumed to start uniformly distributed over the

edges of the network, with $W_m = \ell_m / \sum_n \ell_n$ the probability of starting on edge m. In Fig. 3.2c we plot the search rate, defined as the inverse of the averaged mean first passage time for many choices of target node location. Across a wide range of target concentrations ρ, we see a search rate scaling as $\rho / \log \rho$. This scaling indicates the ER is well-connected and behaves largely as a two-dimensional system, with a logarithmic correction factor to the linear concentration scaling expected for mass action kinetics. A limit is reached when $1/\rho$ becomes comparable to the typical edge length of the ER network structures: $\ell \approx 1.2 \pm 0.1 \mu$m (expected value of starting edge length for uniformly distributed particles, with standard error of the mean computed over different networks). In this limit, particles need only diffuse along a single edge before encountering a target site. This gives rise to effectively one-dimensional kinetics or ρ^2 scaling. It should be noted that the estimated physiological exit site density (yellow line in Fig. 3.2c) is in a range where the search rate is super-linearly dependent on ERES concentration. Increasing the number of target sites should thus disproportionately speed up the encounter process.

Variability of arrival times

One important question in considering kinetics on complex geometries is the extent to which the mean first passage time can be used to characterize the full distribution of reaction times. For compact diffusive search on fractal geometries of dimension less than two, the first passage time distribution is known to exhibit a broad range of relevant time-scales, so that the search process is not well-characterized by the MFPT [137, 47]. Although the search for very sparse targets in ER networks appears to be effectively two-dimensional, signatures of geometry-controlled kinetics (such as a strong dependence on source and target position [47]) are nevertheless observed. In particular, the mean first passage time varies substantially depending on the distance of the starting node from the target (Fig. 3.3). Nodes at similar spatial (Euclidean) distances can also exhibit very different mean first passage times, due to the heterogeneous nature of the ER network connectivity. Because diffusing particles explore many paths from the source to the target, the MFPT can also be very different for nodes with similar values of

the ‘network distance’, defined as the shortest distance between two points measured along the network edges. Furthermore, the standard deviation of the arrival time from a given starting node can be substantially larger than the mean first passage time itself, particularly for nodes located close to the target (Fig. 3.3c). This effect again arises from the multiple time-scales associated with particles following a variety of different paths to the target site.

These observations imply that diffusion-limited reactions within the ER network deviate from the expectations of bulk kinetics, where arrival times generally represent a Poisson process with a well-characterized MFPT and a comparable standard deviation. Instead, particles starting in regions nearby and well-connected to the target arrive much faster than particles from far away. Furthermore, even for a given starting point, some particles travel rapidly directly to the target, while others meander away to explore the rest of the network, leading to broadly distributed first passage times.

3.4.2 Finite reaction rates

First passage times to perfectly absorbing network nodes represent purely diffusion-limited kinetics, where a reaction occurs as soon as the particle finds its target. A biologically relevant complication to this model would include finite reaction rates in certain regions of the network. Such rates become relevant when a reaction requires particles to undergo rearrangements, rotations, or conformational changes in addition to simply finding each other diffusively. If those rearrangements occur on a timescale that is relatively slow compared to the time for the reactants to diffusively separate again, then the reaction kinetics cannot be simply treated as first passage to a perfectly absorbing target site. Instead, the target site is assumed to have a particular rate of reacting with the particle, that is applicable only when the particle is within some minimal contact distance from the target. Models with spatially localized finite reaction rates have previously been employed in quantifying the kinetics of multi-conformation DNA-binding proteins searching for their genomic target sites [138], and of vesicles encountering cytoskeletal filaments to initiate motor-driven transport [139]. For one-dimensional models of a tubular geometry, finite

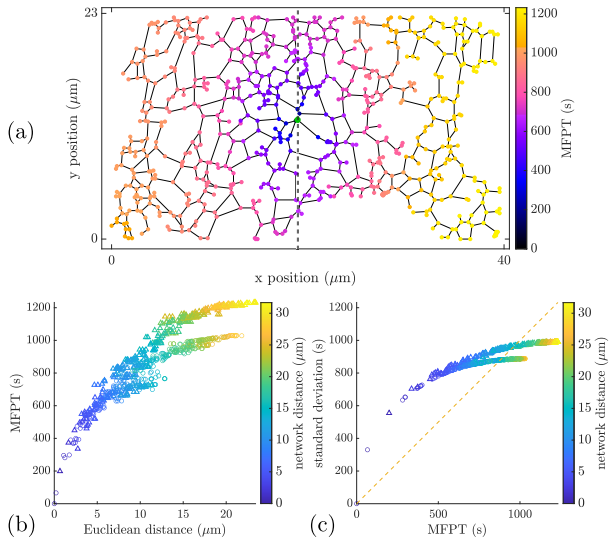

Figure 3.3. Plot of mean first-passage time (MFPT) versus starting distance from target. (a) ER network structure with a single target (green) and color indicating the MFPT to the target for particles starting at each node. (b) Dependence of MFPT on Euclidean distance from the target for each node; color indicates network distance of each node to the target; circles and triangles indicate nodes to the left and right of the target, respectively. (c) Analogous plot showing standard deviation for the first passage time distribution. Dashed line shows standard deviation for a constant-rate Poisson process ($\sigma_{\mathrm{FPT}} = \mathrm{MFPT}$) for comparison. A diffusivity of $D = 1\mu\mathrm{m}^2/s$ is assumed.

reaction rates can also be used as a simplification to account for the radial diffusion time required to find a target by a particle that approaches its axial position [140].

In our model of diffusion on tubular networks, particles spend all their time on network edges, with nodes serving only as intersections that allow transitions between edges. We therefore consider reaction rates that are associated with each edge of the network, defining γ_{ij} as the reaction rate on the edge connecting nodes i and j. Reactions near a particular node can be represented by setting the reaction rates in all edges around that node. If necessary, additional degree-2 nodes can be inserted along the edge to confine the reactive area still further.

To solve for the mean reaction time in this model, we first consider the propagation of the particle from a single neighborhood (i). The Laplace-transformed probability distribution on each edge around node i, $\widehat{c}_{ik}$, obeys a modified form of Eq. 3.3. Namely,

$$s\widehat{c}_{ik} - c_{ik}(t=0) = D\frac{\partial^2 \widehat{c}_{ik}}{\partial x^2} - \gamma_{ik}\widehat{c}_{ik}. \tag{3.20}$$

This can be solved to find the flux into each of the adjacent nodes:

$$\widehat{P}_{ik} = \alpha_{ik}\left(\sinh\alpha_{ik}\ell_{ik}\sum_{j=1}^{d_i}\alpha_{ij}\coth\alpha_{ij}\ell_{ij}\right)^{-1}, \tag{3.21}$$

where $\alpha_{ij} = \sqrt{(s+\gamma_{ij})/D}$. The splitting probability P^*_{ik} of hitting an adjacent node before any reaction occurs is given by plugging $s=0$ into the expression above. The probability of reacting before leaving the neighborhood of node i can then be calculated as $1-\sum_k P^*_{ik}$.

The Laplace-transformed probability that the particle is still in the neighborhood by a certain time (having neither reacted nor reached an adjacent node) is given by

$$\widehat{Q}_i = \sum_{k=1}^{d_i}\int_0^{\ell_{ik}}\widehat{c}_{ik}dx = \frac{1}{D}\frac{\sum_{j=1}^{d_i}\frac{1}{\alpha_{ij}}\tanh(\frac{\alpha_{ij}\ell_{ij}}{2})}{\sum_{j=1}^{d_i}\alpha_{ij}\coth(\alpha_{ij}\ell_{ij})}. \tag{3.22}$$

Evaluating this expression at $s=0$ gives the average waiting time to leave the neighborhood.

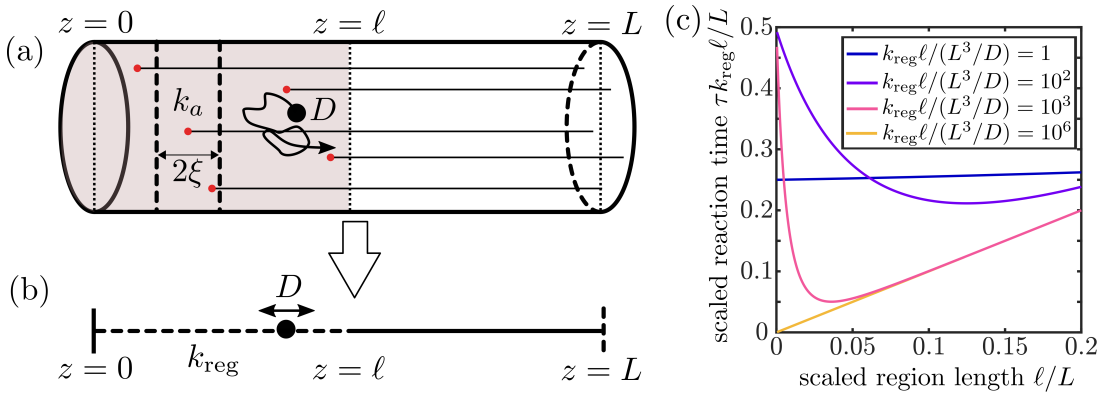

Figure 3.4. Reaction times for localized finite reactive region in one dimension. (a) Schematic of cylindrical domain representing a cellular projection (such as a neuronal axon), with reactive points representing microtubule tips distributed over a region of length ℓ, with k_a the absorbance rate for a particle that reaches an axial position within distance ξ of a tip. (b) The cylindrical system is mapped to a one-dimensional model, with effective reaction rate k_{reg} in the region where microtubule tips are distributed, a reflecting boundary at $z = 0$ representing the distal tip of the projection, and an absorbing boundary at $z = L$ representing the cell body. (c) Scaled mean absorption time for particles originating at $z = 0$ and diffusing in the partially reactive one dimensional domain.

Similarly, for particles starting uniformly distributed along network edge m, we can find the flux into one of the bordering nodes j (defined as $\widehat{P}_{mj}^{(E)}$) and the survival probability on the edge ($\widehat{Q}_m^{(E)}$) using Eq. 3.10, where we replace α with the edge-dependent α_m.

These expressions can then be plugged directly into Eq. 3.13 or Eq. 3.14 to compute the mean first passage time to leave the network through either the finite-rate reactions along network edges or through reaching a perfectly absorbing target node. To find the MFPT in the presence of perfectly absorbing targets, all elements corresponding to the target nodes should be removed from the matrix expressions as before, so that reaching the targets is treated as permanently leaving the network.

Example: Extended absorbing region in one dimension

A simple example of the calculations described above involves particles on a one-dimensional interval containing a region with a finite reaction rate k_{reg}. Such a system can be thought of as a simplified representation of a tubular cellular domain, such as a fungal hypha

or neuronal axon [141]. Organelles such as signaling endosomes and autophagosomes that are produced at the distal end of this domain must be loaded onto microtubules to be delivered in a retrograde fashion to the nuclear region [142, 143]. There is evidence that some cellular cargos begin their retrograde journeys by binding preferentially to microtubule plus-end tips, which accumulate high concentrations of dynein motors and associated activator proteins to form a 'loading zone' at the distal cell tip [144, 145]. An interesting question then arises regarding how the distribution of microtubule tips near the distal end affects the overall rate of loading the organelles. If all tips are localized right at the distal end, particles originating at the distal end will have a chance to bind as soon as they are formed. However, any particles that diffuse axially past the tips may end up exploring the full domain over long time periods without returning to the distally localized tips. On the other hand, a broader distribution of tip positions may make particles more likely to latch on before diffusing away.

We explore this trade-off by mapping the distribution of microtubule tips in a cylindrical domain to an effective one-dimensional model (Fig. 3.4a, b), where ℓ represents the length of the region over which microtubule tips are distributed. The overall attachment rate in this region can be approximated as $k_{\text{reg}} = nk_a\xi/\ell$, where n is the number of microtubule tips, ξ is the contact radius for binding a tip, and k_a is an effective binding rate that incorporates rapid radial diffusion to encounter the tip while at the appropriate axial position. We assume a reflecting boundary at $z = 0$ representing the distal end, and an absorbing boundary at $z = L$ representing the region near the nucleus that serves as the target for the particles. Particles are initiated at $z = 0$ and diffuse with diffusivity D until they are either absorbed in the reactive region or reach the soma through diffusion alone. For simplicity, we neglect the motor-driven transport time to reach the soma after loading on the microtubules, focusing instead on the optimal dispersion of microtubule tips to minimize the loading time. For a given number of microtubules, $k_{\text{reg}}\ell$ is expected to be constant and we explore how distribution over different region lengths ℓ affects the first passage time to loading.

Treating the 1D simplified system (Fig. 3.4b) as a network with only two edges, one

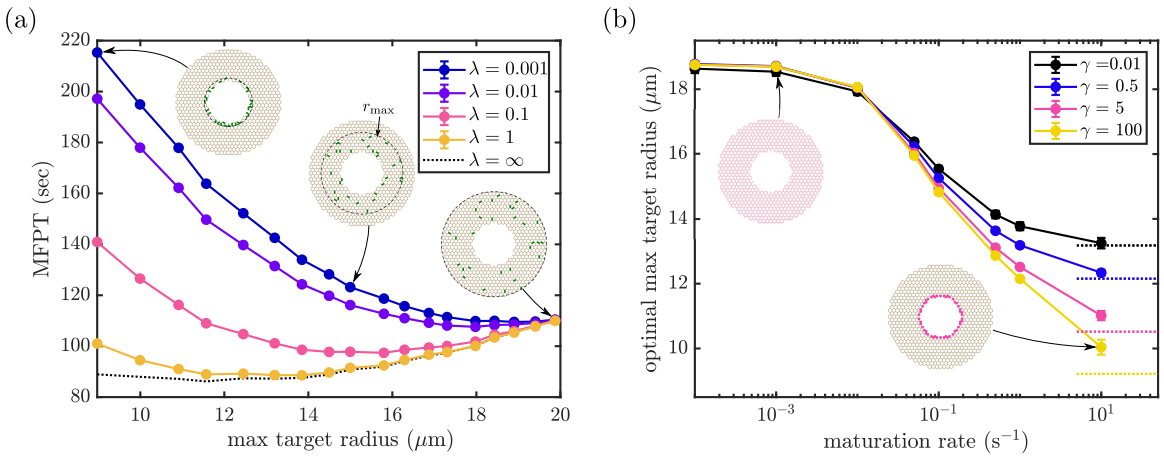

Figure 3.5. Mean first passage times on synthetic honeycomb networks with dimensions similar to the ER in COS7 cells. (a) The relationship between MFPT of particles initiated on interior nodes and maximum radial distance of 30 absorbing edges ($\gamma = 1\text{s}^{-1}$) for various maturation rates, λ. Each dot shows the MFPT averaged over 500 different combinations of absorbing edges within the maximum target distance (errorbars included but not visible at this scale.) Example networks are shown for small, medium and large maximum target distance, with target edges highlighted in green. Dashed black line shows the case with no maturation process ($\lambda = \infty$). (b) The effect of maturation rates, λ, on the optimal maximum target distance, with various absorption rates, γ. Dashed lines indicate optimal maximum target distance in limiting case of instantaneous maturation ($\lambda = \infty$). Inset networks illustrate particle distribution at time of maturation for two different choices of maturation rate.

of which is absorbing, we plot (in Fig. 3.4c) the mean first passage time for a particle to either react with the microtubule tips or reach the far end of the domain. Interestingly, an optimum is observed with respect to the length ℓ over which the absorbing tips are distributed, indicating that it is advantageous to spread out microtubule tips in the distal region rather than placing them all as near as possible to the distal end. The optimum value of ℓ increases as the overall reactivity goes down. When the tip reaction rate k_a is very rapid, then $\ell_{\text{opt}} \to 0$ as no particle can make it past the most distal tips. By contrast, when k_a is very low, the optimum disappears entirely as particles have the chance to explore the entire domain and reach the distal absorbing boundary without ever binding in the absorbing region, regardless of its size.

Example: Target distribution on a 2D network

Similar to the one-dimensional case described in the previous section, we can explore how the distribution of reactive regions in a two-dimensional network such as the peripheral endoplasmic reticulum affects diffusive search times. Here, we use a synthetic network consisting of a honeycomb lattice structure in a circular band with dimensions comparable to the peripheral ER in COS7 cells (Fig. 3.2, insets). The network has an edge length 0.8μm (equal to average edge length for ER networks used in this study), an inner radius of 8μm representing the nucleus, and an outer radius of 20μm representing the cell boundary.

Most protein synthesis in the ER is thought to occur in the ribosome-studded perinuclear sheets [9], so we consider particles that are initiated at the innermost nodes of the network. Localized reactive regions are distributed over the network edges to represent ER exit site structures. A finite reaction rate on each exit-site edge accounts for any additional process that a particle must undergo after reaching an exit site before it can be stably captured. Such processes could include rotation, molecular rearrangement, or entry into a narrow-necked ERES structure [136].

One question of particular interest is whether there is any functional advantage to scattering ERES throughout the peripheral network, rather than concentrating them in the perinuclear region where proteins are initially translated. Given that both luminal and membrane proteins have been shown to penetrate throughout the peripheral tubular structure [9], one possible advantage to well-dispersed ERES is to efficiently capture proteins that happen to diffuse deeply into the periphery. We therefore consider how the average reaction time varies when a fixed number of reactive sites are distributed across regions of different width surrounding the interior boundary where particles are initiated.

Interestingly, unlike the one-dimensional case in Fig. 3.4, there is very little advantage to dispersing reaction regions over a broader region of the two-dimensional lattice network. The dashed black line in Fig. 3.5a shows the MFPT for a network with 30 edges with reaction

rate $\gamma = 1\text{s}^{-1}$, spread out over increasingly broad regions of the network. While there is a slight optimum when the reactive edges are allowed to spread to a radial distance of 12μm, the difference between this system and one where targets are placed in the innermost region of the network (in the same location where particles originate) is less than 3%. Higher values of reactivity γ make it even more advantageous to concentrate all reactive sites closer to the inner radius, while lower values of γ make the system independent of the reactive edge distribution (data not shown), much as in the one-dimensional case. In no case does there appear to be a substantial advantage to spreading out the reactive edges.

This result underscores a fundamental distinction between a well-connected 2D network and a 1D interval. In the network, moving target sites out from the central region where particles are initiated necessitates spreading those sites out over a longer band, leaving gaps for particles to be able to diffuse through without hitting any target. Particularly in the case of high reactivity γ, such gaps allow escape of particles into the periphery that would not be possible if the targets were concentrated near the inner radius of the network. This effect counterbalances the advantage to capturing particles which do manage to disperse through the network. As a result, there is no substantial benefit to placing target sites further out in the periphery for the 2D network case.

However, the dispersed placement of reactive sites can greatly enhance kinetics in the case where newly synthesized particles are incapable of reacting immediately upon production, as discussed in the subsequent section.

Example: Maturing particles

Another potentially important complication for a variety of biomolecular search processes is the existence of a 'maturation time,' during which particles diffuse through the domain but are not able to undergo the relevant reactions. For example, newly manufactured proteins in the ER must undergo folding and quality control processes that can take from minutes to hours before they are able to be loaded at ER exit sites for export [146, 134]. Such particle maturation can be easily incorporated in our model as a Poisson process of rate λ that occurs simultaneously

with diffusion. While the particle is maturing, it is not capable of reacting even if it reaches the reactive edges. As soon as the particle matures, reactivity is enabled and the particle's mean first passage time can be determined from its maturation point using an extension of the usual techniques outlined above.

Specifically, we define $\psi_m(x,t)$ as the overall density of particles on edge m at time t. Its Laplace-transformed form is given by

$$\widehat{\overrightarrow{\psi}}_m(x,s) = \overrightarrow{V} \cdot \left(\mathbf{I} - \widehat{\mathbf{P}}\right)^{-1} \cdot \widehat{\mathbf{c}}\,(x,s)\,, \tag{3.23}$$

where the entries $\widehat{c}_{im}\,(x,s)$ contain the Laplace transformed particle densities along edge m defined for the node neighborhood i, as given by Eq. 3.4.

This approach allows for nonuniform particle densities along each edge. In order to find mean first passage time after maturation, we need to compute the overall survival probability, $H_m^{(E)}(x,t)$, for a particle starting at position x on edge m. Such a particle can remain on the edge until time t, react during that time, or hit either of the bounding nodes (i,j) before time t. In the latter case, its survival probability can be obtained by convolving with the expression in Eq. 3.13 for particles initiated on a node. The overall Laplace-transformed survival probability is obtained as

$$\begin{aligned}\widehat{H}_m^{(E)}(x,s) = \widehat{Q}_m^{(E)}(x,s+\gamma_m) + \widehat{P}_{m,i}^{(E)}(x,s+\gamma_m)\widehat{H}_i(s) \\ + \widehat{P}_{m,j}^{(E)}(x,s+\gamma_m)\widehat{H}_j(s).\end{aligned} \tag{3.24}$$

Here, $\widehat{Q}_m^{(E)}(x,s)$ and $\widehat{P}_{m,i}^{(E)}(x,s)$ are the survival probability and flux to the bounding node, respectively, given the particle starts at x. These quantities can be obtained using the standard solutions for diffusion on a one-dimensional interval with two absorbing boundaries [133] (*i.e.:* from Eq. 3.9).

The overall mean first passage time after maturation (not including the maturation time

of $1/\lambda$ itself) is then

$$\tau(\lambda) = \lambda \sum_m \int_0^{\ell_m} \widehat{\psi}_m(x,\lambda)\widehat{H}_m^{(E)}(x, s=0)dx, \tag{3.25}$$

where the sum is over all edges in the network.

Again considering the synthetic honeycomb networks, we can investigate the effect of particle maturation on mean first passage time, and probe the functional advantage of widely-distributed ER exit sites. In Fig. 3.5a we see that by adding a maturation process (*e.g.* $\lambda \leq 0.1\text{s}^{-1}$), the MFPT of particles starting at the inner boundary exhibits a pronounced minimum when the reactive regions are spread out over a broader region of the network. As the maturation rate becomes slower (*e.g.* $\lambda = 0.001\text{s}^{-1}$,) the particles have time to spread uniformly across the network before maturing and it becomes advantageous to disperse targets over the entire network structure.

The interplay of maturation and local reactivity is highlighted in Fig. 3.5b. For lower maturation rates, it is best to distribute reactive regions throughout the network, regardless of local reaction rate γ. For higher maturation rates, we see the optimal distance vary depending on reactivity. For rapid absorption ($\gamma = 100\text{s}^{-1}$) concentrating targets near the inner boundary is advantageous, as most particles can be captured shortly after maturation before they have a chance to explore the network. For slower reactivity, many particles have a chance to explore the full network structure and placing the target regions more broadly dispersed throughout the network becomes advantageous.

These results highlight how the placement of reactive regions in a tubular network can lead to non-trivial effects on the overall reaction rate. The analytic approach described here allows for rapid, easily implemented calculations of the mean and variance of reaction times. This approach thus makes practical an extensive exploration of how network morphology and the distribution of target positions and/or reaction rates modulate kinetic processes involving stationary network structures.

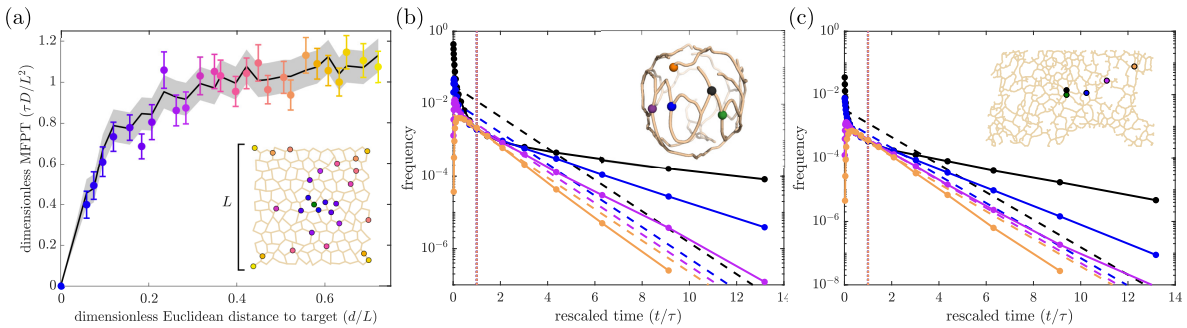

Figure 3.6. First passage times to a stationary target obtained with exact kinetic Monte Carlo simulations. (a) Mean first passage times for particles starting at different source nodes on a synthetic planar network to reach the target (green), plotted versus Euclidean distance from source to target. Error bars give standard error of the mean ($n = 150$ particles simulated). Black line and shaded region give mean and expected standard error from corresponding analytical calculations. Diffusivity is set to $D = 1\mu\text{m}^2/s$; length units are non-dimensionalized by network size L and time units by L^2/D. (b) Distribution of first passage times to a target node (green), scaled by the MFPT (τ), on a yeast mitochondrial network. Color corresponds to different starting nodes. Dashed lines show expected exponential decay for a Poisson process with the same mean. (c) Analogous plot for particles diffusing on a peripheral ER network structure.

3.5 Simulating particle trajectories

The analytic first passage time calculations described in the previous section are limited in several important aspects. First of all, they directly provide only the low-order moments (mean and variance) of first passage time distributions, without enabling the exploration of more detailed features, such as the extreme statistics for the earliest and latest arriving particles, which are important in a variety of biological signalling processes [65]. In the complex, compact geometry of a reticulated network, the relevant arrival timescales can be very broadly distributed, and are not necessarily well-characterized by the mean and variance alone [137, 47]. Furthermore, our calculations thus far have been restricted to immobile targets or reactive regions within the network. Modeling the behavior of more complex reaction-diffusion processes, which may involve interaction between multiple mobile particles, can be achieved by switching from analytically tractable methods to agent-based stochastic simulations.

Agent-based simulations are particularly relevant when the reacting molecules are present in small copy numbers and substantial fluctuations of local concentration make mean-field de-

scriptions of particle concentrations inaccurate. The simplest such reaction-diffusion simulations rely on Brownian dynamics, with particles taking very small discrete time steps and checking for a reaction on each step [147]. A series of alternate schemes have been developed to minimize the computational cost of propagating particles when they are far away from each other or the domain boundaries. Such methods, which have been variously termed Green's Function Reaction Dynamics or first-passage kinetic Monte Carlo [118, 119, 66, 120], leverage analytically computed propagator functions to move individual particles over large time steps within a 'protected domain' where interaction with other particles or structures does not occur. They thus enable rapid propagation in regions where particle motion is purely diffusive, interspersed with a finer time-resolution in regions where reactions may take place. The main required assumption is that each propagated step of the particle is Markovian (memory-less) and that there are no reactions, obstacles, or interactions with other particles while the particle is propagating within the protected region.

Kinetic Monte Carlo approaches all rely on sampling the time interval for the next event of interest to occur, from an appropriate distribution of transition times. Original schemes relied on exponentially distributed transition times [148], while the more recent approaches sample from the analytically known distributions of first passage times in simple domains such as a one-dimensional interval or three-dimensional sphere [66, 120]. Here, we leverage our diffusive propagator between network node neighborhoods (Sect. 3.3) to develop an efficient kinetic Monte Carlo simulation algorithm optimized for diffusive particles on tubular networks. In this section, we focus on instantaneous reactions with perfectly absorbing target nodes, although the method can easily be expanded to include finite reactivity on edges.

3.5.1 Single particle propagator

For a single particle propagating on a network, we consider the particle starting at node i at time $t = 0$. A protected domain can then correspond to the local neighborhood, containing all the edges connected to node i. The distribution of times to leave this domain is given by the flux

into all the neighboring nodes, which are treated as absorbing boundaries. Specifically, we begin by sampling which neighboring node k is first reached by the particle, from the discrete splitting probability P_{ik}^* given in Eq. 3.8a. The distribution of times to first hit this node, conditional upon not previously leaving the neighborhood, can then be obtained by the Laplace inversion of the flux $\widehat{P}_{ik}$ (Eq. 3.6), normalized by P_{ik}^*.

To perform the Laplace inversion, we first numerically calculate the poles of $\widehat{P}_{ik}$. These poles occur at discrete values s_p, which fall on the negative real axis and can be expressed as $s_p = -Du_p^2$, where the u_p satisfy the following equation

$$\sin(\ell_{ik}u_p)\sum_{j=1}^{d_i}\cot\left(\ell_{ij}u_p\right) = 0. \tag{3.26}$$

The residues $r_p^{(ik)}$ at the poles can be found by evaluating the derivative of Eq. 3.26 with respect to s, yielding

$$\frac{1}{r_p^{(ik)}} = \frac{\sin(\ell_{ik}u_p)}{2Du_p}\sum_{j=1}^{d_i}\ell_{ij}\csc^2\left(\ell_{ij}u_p\right). \tag{3.27}$$

Finally, we evaluate the inverse Laplace tranform using the standard Bromwich integral together with the Cauchy residue theorem [149]:

$$P_{ik}(t) = \sum_p r_p^{(ik)} e^{-Du_p^2 t}. \tag{3.28}$$

In a kinetic Monte Carlo simulation, we initiate a particle on node i, sample the next neighboring node to be reached (k) according to probabilities P_{ik}^*, and then use inverse transform sampling to select the time interval Δt to first reach this node according to the normalized probability distribution $\Delta t \sim P_{ik}(\Delta t)/P_{ik}^*$. Details of the sampling procedure are provided in B.3. To validate the simulations, we evaluate the mean and standard deviation in first passage times from different starting positions to a particular target on a 2D lattice-like network, showing a

close match to analytical predictions (Fig. 3.6a).

Examples: first passage time distributions

Beyond the low-order moments, simulations allow us to explore the full distribution of first passage times to a target node. Fig. 3.6b, c shows such distributions from several different starting nodes on an example yeast mitochondrial network [55] and a peripheral ER network from a COS7 cell. These distributions are compared to the exponential distribution expected for a constant-rate Poisson process with the corresponding average time. For particles starting far from the target (orange curves), there is a peak "most likely" time of target encounter. Shorter search times are precluded by the need to traverse a substantial distance in the network before ever hitting the target. Particles that start near the target (black curves) exhibit long tails in the first passage time distribution, which are a known signature of compact search processes [47]. These tails highlight the multiple timescales that contribute to the search, as some particles move towards the target immediately while others follow long meandering paths over the network before reaching the target. The deviation from a Poisson distribution, for both nearby and distant starting locations, indicate that reaction kinetics on these networks should have qualitatively different behaviors than would be expected in a bulk three-dimensional continuum.

Another application of stochastic particle hopping simulations is to explore the extreme arrival time—the average time for the first of many particles to find a target on the network. Such calculations are relevant to signaling processes where one or a few molecules are sufficient to trigger a response, so that the shortest rather than the mean arrival times set the timescale of signal initiation [65]. In Fig. 3.7, we run simulations of N independent particles starting from a given position on the network and show the time for the first of these particles to hit a particular target node. For a small number of simulated particles, the average first hitting time scales roughly as $\sim 1/N$, as would be expected in a bulk continuum. In other words, the reaction rate is approximately proportional to the particle concentration. However, for large numbers of particles, we observe a $\delta^2/\log N$ dependence, where δ is the minimal distance along the

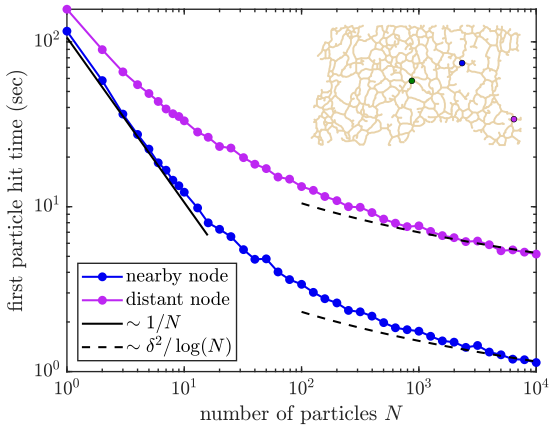

Figure 3.7. Extreme arrival statistics on an ER network structure. Plotted is the average first passage time for the first of N particles to hit a target node (green), starting from either a nearby source (blue) or a distant source (magenta). Scaling laws are shown for the small N limit (solid, $\sim 1/N$) and large N limit (dashed, $\sim \delta^2/\log N$, where δ is the minimal network distance between start node and target). Diffusivity is set to $D = 1\mu\text{m}^2/s$.

network between the starting point and the target. These results are consistent with extreme first passage statistics in one-dimensional or two-dimensional systems [150, 151], and are similar to previous simulations of particle hopping on networks which assumed a single timescale for each individual hop [63].

Synchronizing trajectories

In certain applications, it is desirable to calculate snapshots of the particle position at prespecified times. For example, such trajectory information is needed to compute the mean squared displacement of a particle over different time intervals, a common analysis tool for quantifying the rate of diffusive spread. In this case, during each step of the kinetic Monte Carlo procedure, we check whether the time point $t + \Delta t$ exceeds the next save-time t_s. If that is the case, the particle needs to be propagated first over a time interval $\delta t = t_s - t$. To achieve this, we leverage a spatial 'no-passage' propagator within the neighborhood of node i, which gives the distribution of particle positions conditional on not leaving the neighborhood by time δt. For a particle that starts on node i at time 0, and does not leave the neighborhood, the probability that it is on the edge connecting i to k, between position x and position ℓ_{ik}, at time δt is defined as

$Y_{ik}(\delta t)$. The Laplace transform of this spatial cumulative distribution is:

$$\begin{aligned}\widehat{Y}_{ik}(x,s) &= \int_x^{\ell_{ik}} \widehat{c}_{ik}(x',s)dx' \\ &= \frac{1}{s}\widehat{P}_{ik}\left[\cosh(\alpha\ell_{ik}) - \cosh(\alpha x)\right]\end{aligned} \tag{3.29}$$

To invert the Laplace transform, we note that this expression has the same poles as the flux $\widehat{P}_{ik}$, so that

$$Y_{ik}(x,\delta t) = \sum_p \frac{r_p^{(ik)}}{Du_p^2}\left[\cos(u_p x) - \cos(u_p \ell_{ik})\right] e^{-Du_p^2\delta t} \tag{3.30}$$

To propagate the particle forward over a time interval δt, we first sample which edge ik the particle is positioned on, using the discrete probabilities $Y_{ik}(0,\Delta t)$. The position along the edge is then sampled according to the conditional cumulative distribution: $\mathscr{P}(x' > x) = Y_{ik}(x,\Delta t)/Y_{ik}(0,\Delta t)$.

Once the particle has been placed at position x_0 along a specific edge m (bounded by nodes i and k), we can use a Laplace inversion of Eq. 3.9 to sample the next time interval Δt for the particle to first hit either node i or node k. If this time interval would again exceed the next desired save point, the particle is propagated spatially along the edge (see B.3 for details).

Simulations of complete particle trajectories can be used to explore the mean squared displacement (MSD) of particles diffusing over a network structure. As seen in Fig. 3.8, particles on a poorly connected network with many dead ends exhibit a lower, apparently subdiffusive, MSD than particles on a lattice-like network. This result implies that MSD analysis alone may indicate subdiffusive motion even when the particles are in fact undergoing classic diffusive motion, due to confinement on a network structure with missing connectivity.

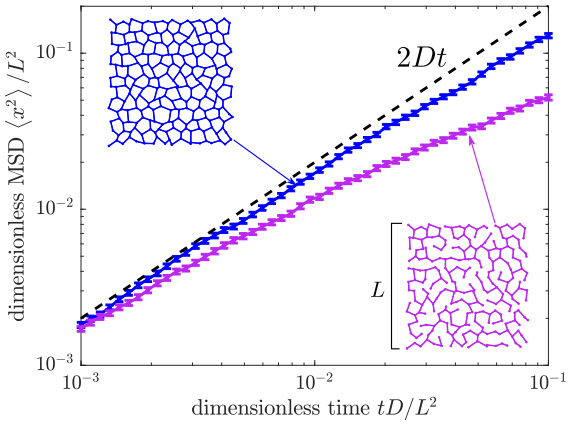

Figure 3.8. Mean squared displacement for simulated diffusing particles on two synthetic networks. Blue: Synthetic planar network with full lattice-like connectivity. Magenta: decimated network network with 27% of edges removed while maintaining a single connected component. Length units are non-dimensionalized by network size L and time units by L^2/D.

3.5.2 Simulating multiple particles

Many problems concerning reaction kinetics on networked geometries require the ability to simulate not just individual particles searching for stationary target sites, but also multiple mobile particles that encounter and react with each other. Additional complications arise in the multi-particle case because the possibility of reaction with a neighbor alters the distribution of each particle after any given time interval. This issue was addressed in previous studies by introducing 'protective domains' that break up the available space into disjoint regions wherein each particle propagates independently of the others with no chance of interaction [66, 119]. For example, on a simple 1D interval, such protective domains can be defined by placing boundaries at all points half-way between the positions of neighboring particles. This notion was refined further by noting that when two particles approach close to each other, infinitesimal time steps can be avoided by defining a single protective domain surrounding both of them and then jointly propagating the pair distribution of the two particles [66].

In our system, a protective domain around a particle has one of the following three forms (Fig. 3.9). An edge segment domain is a single linear segment with end-points on one network

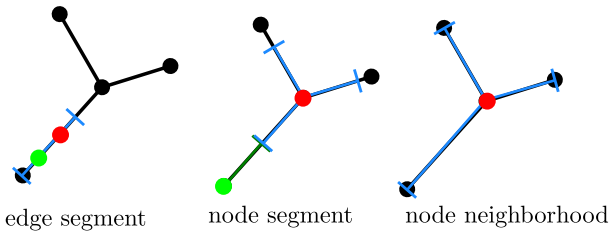

Figure 3.9. Protective domains used in multi-particle simulations. The network region is shown in black, the particle of interest in red, and the protective domain containing it in blue. An edge segment domain is confined to a single edge and can contain a pair of particles (green). A node segment domain is centered on a node, with equal-length segments along all edges; it is employed when a nearby particle with its own domain (green) prevents a direct hop onto an adjacent node. A node neighborhood domain encompasses the full edges connected to a given node, and requires the particle to start on the node itself.

edge. This domain can contain one or two particles and is made as big as possible given the edge length and the presence of any additional particles. A node segment domain is centered on a node and surrounded by equal-length segments of the adjacent edges. The segment lengths are set to the minimum of the distance to the nearest unoccupied node or half the distance to the nearest other particle along each edge. Finally, the full node neighborhood domain is employed in the case where there are no other particles on the nodes or edges adjacent to the current node. The asynchronous time propagation for multiple particles proceeds as described in [66] and summarized below.

At the start of the simulation, all particles are distributed into non-overlapping protective domains of the form illustrated in Fig. 3.9. The particles all begin synchronously with the global time set to zero. We then proceed to sample the first passage time for each particle or pair of particles to leave its protective domain, as well as the boundary through which they leave. This results in an ordered queue of times $t_i < \ldots < t_k$ for leaving the domain. The particle with the shortest leaving time t_i is propagated to one of the edges of its domain. Any other particle (j_1, j_2, etc) whose domain touches the boundary reached by particle i is also propagated forward to time t_i, using the spatial propagator appropriate to its domain (eg: Eqs. 3.30, B.9). The affected particles $i, j_1, j_2, \ldots$ are then partitioned into protective domains. New exit times are selected

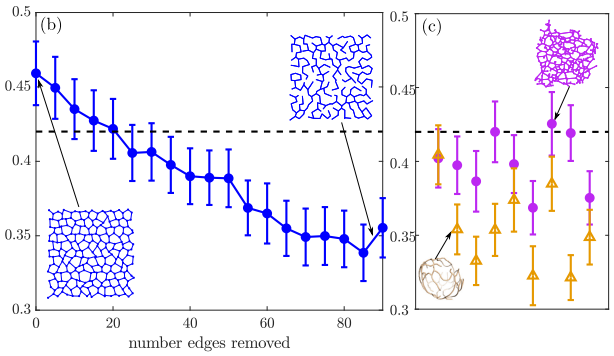

Figure 3.10. First encounter times for two diffusing particles (with same diffusivity), compared to the analytic tagMFPT to a stationary target. Target initial position is averaged over all network nodes, and particles start uniformly distributed along network edges. (a) Relative search time on network consisting of single line of nodes. Dashed black line indicates analytic expected value on a finite-length linear segment. (b) Relative search times on a lattice-like synthetic network with increasing number of edges removed, reducing connectivity. (c) Relative search times on 9 ER network structures from COS7 cells (magenta circles), 9 yeast mitochondrial network structures (orange triangles). Error bars show standard error of the mean, for simulations of 500 particles.

for these particles and added into the priority queue. Each step of the algorithm thus consists of propagating a single particle using the appropriate first-passage time distribution for its domain and one or more particles using the spatial "no-passage" distribution within their domain. The number of such no-passage particles is at most equal to two (if particle i ends on an edge) or the degree of the network node to which it has transitioned.

The first-passage and no-passage propagators for a single particle have already been derived for a node-neighborhood domain (Eqs. 3.28 and 3.30, respectively) and an edge-segment domain (Eq. B.8 and B.9). A node-segment domain, consisting of d segments of equal length ℓ, can be treated identically to a single one dimensional interval with absorbing boundaries at $(-\ell, \ell)$ and the particle starting at $x_0 = 0$. Given the symmetry of the domain, the particle has a $1/d$ chance of ending a first-passage or a no-passage step on any one of the edges. The joint propagation of a pair of particles that share an edge segment is described in B.3.4.

Example: Pair encounter times

We use simulations on a variety of network structures to compare the encounter time for two diffusive particles (τ_{enc}) versus the mean first passage of a single diffusive particle searching for a stationary target placed anywere on the network (target-averaged global MFPT, or tagMFPT). On an infinite line or plane, the separation between a pair of particles is itself diffusive, with an effective diffusivity $2D$. The pair encounter time is thus expected to be half that of the MFPT to a stationary target. In a finite domain, the pair encounter time is dependent on the initial separation between the two particles, as well as on their position relative to the domain boundaries. An exact solution for this encounter time is available for pair diffusion on a line segment [152], where averaging over starting positions gives

$$\begin{aligned}\tau_{\text{enc}}^{(1D)} &= \frac{L^2}{D}\left(\frac{1}{8}+\frac{32}{\pi^5}\sum_{k=0}^{\infty}\frac{\cos(k\pi)-\sinh\left(\left(k+\frac{1}{2}\right)\pi\right)}{(2k+1)^5\cosh\left(\left(k+\frac{1}{2}\right)\pi\right)}\right)\\ &\approx 0.42\times \text{ tagMFPT}.\end{aligned}$$

Simulation results using our algorithm reproduce this expected behavior on a simple network consisting of a line of nodes (Fig. 3.10a). We next look at pair particle behavior on a planar lattice-like network structure with degree 3 nodes and multiple edges removed to reduce network connectivity. The edges are chosen at random while keeping a single connected cluster within the network. For a full lattice network, the pair encounter time is nearly half of the tagMFPT. However, as the network connectivity decreases and approaches a tree-like loop-less structure, the pair encounter time drops substantially lower, to about 0.3 tagMFPT (Fig. 3.10b). On poorly connected networks the ability of a target to move diffusively can thus greatly speed up the encounter time, beyond what would be expected in a bulk continuum geometry. This result stems from the fact that poorly connected networks have highly heterogeneous global mean first passage times, depending on where a stationary target is placed [45]. If the target is located in regions of the network that are difficult to access, the MFPT can be several times higher than

the average over all target positions [45]. Even when averaging over different target locations, the extremely poor accessibility of some target positions leads to tagMFPTs that are more than twice as slow as the pair encounter time where both particles are diffusive and capable of leaving the hard-to-access regions.

We also compare the pair encounter time to the stationary target search time for several organelle network structures (Fig. 3.10c). Given their high connectivity, peripheral ER network structures have a pair encounter time that is, on average, $\left\langle \tau_{\text{enc}}^{(ER)}/\text{tagMFPT} \right\rangle \approx 0.40 \pm 0.007$ (standard error over networks). Even for these highly looped structures, the pair encounter time is less than half the averaged first passage time to a stationary target. Yeast mitochondrial network structures are less well connected (less looped) than the mammalian ER [45], and their pair encounter time is slightly lower: $\left\langle \tau_{\text{enc}}^{(\text{mito})}/\text{tagMFPT} \right\rangle \approx 0.35 \pm 0.009$. These results imply that diffusion of ER and mitochondrial structures such as ERES components or nucleoids may be helpful in allowing for rapid search by diffusing proteins.

3.6 Discussion

The methodology outlined in this work allows for precise modeling of the propagation of diffusive particles confined in tubular network structures. We first describe analytic calculations for the mean and variance of the first passage time to reach one of several stationary target sites. Our approach is distinct from past studies of transport on spatial networks [113, 153, 64, 63] by explicitly considering the physical process of diffusion between network nodes, allowing the exact calculation of appropriate splitting probabilities and mean hopping times between adjacent nodes, as a function of the relevant edge lengths. Applications to peripheral ER network structures indicate the effective kinetics in the ER are intermediate between those expected in a 1D *vs.* 2D geometry (Fig. 3.2), as well as highlighting the spatial heterogeneity in first passage times between different regions of a network (Fig. 3.3).

The analytic calculations are then further expanded to consider partially reactive edges

scattered throughout the network, giving spatially heterogeneous reaction rates. This model allows an exploration of how the spatial distribution of a fixed total absorbance affects reaction kinetics. In a single long tube, we show that spreading out an absorbing region over an intermediate length-scale results in optimal mean reaction times (Fig. 3.4). This result is applied to distal cargo capture by microtubule tips and implies a benefit to heterogeneous microtubule lengths in extended cell domains such as neuronal axons and fungal hyphae. In a two-dimensional lattice-like network, dispersal of partially absorbing regions away from the source of particle production is shown to be advantageous primarily when particles have a finite maturation time period before they can react (Fig. 3.5). While protein production in the endoplasmic reticulum is thought to occur largely in the perinuclear rough ER, secreted proteins must undergo a folding and maturation process over timescales of minutes to hours before they can exit the network [146]. Our results thus indicate a potential functional role for the dispersion of ER exit sites throughout the periphery, where they can catch diffusing proteins as they mature.

Complementing the analytic MFPT calculations, we also present an exact, efficient algorithm for agent-based reaction-diffusion simulations of particles on a tubular network. This algorithm constitutes a special case of kinetic Monte Carlo [66] or Green's Function Reaction Dynamics [119] approaches, tailored for a network geometry. Unlike classic Brownian Dynamics, it allows for step sizes on the order of entire edge lengths, while sampling from the exact node propagator distribution function. In contrast to a variety of prior studies of stochastic trajectories on networks [60, 154, 63], we do not assume a single well-defined timescale for each node transition and instead incorporate the full distribution of transition times and splitting probabilities based on physical diffusion over edges of arbitrary length. Such simulations allow for calculations that go beyond the mean target search time, to explore reaction time distributions (Fig. 3.6), extreme particle statistics (Fig. 3.7), spatial dispersion (Fig. 3.8), and pair encounter times between multiple diffusive particles (Fig. 3.10). Interestingly, the pair encounter times are found to be less than half the timescale for hitting a stationary target, particularly in the case of poorly-connected networks. This finding implies that allowing targets to become diffusively

mobile, rather than fixed to a specific network region, can significantly increase their encounter rates with other diffusing particles.

Our approach is relevant to any spatial network that can be described by curved one-dimensional edges (tubules) connecting nodes of negligible volume. For realistic reticulated networks the implied assumption is that particles spend a negligible amount of time in tubule junctions and are equally likely to enter any of the edges emerging from the junction. While mitochondrial networks generally have nodes that appear to simply be junctions of joining edges [55], the endoplasmic reticulum may include more complex node morphologies such as small regions of fenestrated sheets [155]. While our methods do not currently describe diffusion within such peripheral sheets, they can incorporate the dense patches of tubular intersections that have been hypothesized to comprise some such regions [80]. Including non-negligible trapping times within expanded nodal regions could serve as an important avenue for future work in modeling diffusive transport throughout the ER.

Another potential source of complication in cellular organelles is the combination of diffusive transport with other dynamic processes such as network structural remodeling and the recently postulated intra-tubule flows that may contribute to rapid motion of ER luminal proteins [130, 63]. Topological rearrangements of both mitochondria and the ER occur on the tens of seconds to minutes timescales [123, 32, 39]. Network remodeling is thus unlikely to have a substantial effect on local protein propagation but may modulate the long search times to reach poorly connected regions of the network. Putative flows in the ER lumen have been proposed to rapidly drive luminal proteins betweeen adjoining nodes, without affecting the diffusion of membrane-embedded proteins [130]. Simulations incorporating such flows would require modifying the local node-to-node propagator function for diffusion with drift along individual edges. Both time-varying flows and network rearrangements would require propagating particles forward to synchronization times when such network-level changes occur. In the case of localized changes (ie: flow reversal along a given edge, or extension of a single tubule), substantial speed-up could still be obtained using the asynchronous kinetic Monte Carlo

approach described above.

The methodology presented here has broad applicability to modeling the diffusion of particles over networks with physical edges. Our examples focus on applications to intracellular organelle networks, forming a mathematical framework for exploring diffusion-limited reaction processes in reticulated mitochondria and the ER. These two organelles host a variety of biomolecular pathways of interest, and understanding the kinetics of diffusive search is critical to investigating dynamics of such disparate cellular processes as the early secretory pathway (ER), calcium release and replenishment (ER), and mitochondrial gene transcription. The described framework for simulation and analytic computation of diffusive reaction times in reticulated structures forms an important foundation for exploring the link between morphology and function in complex biological architectures.

3.7 Acknowledgements

Chapter 3, in full, is a reprint of the material with minor edits as it appears in Zubenelgenubi C. Scott, Aidan I. Brown, Saurabh S. Mogre, Laura M. Westrate, and Elena F. Koslover. "Diffusive search and trajectories on tubular networks: a propagator approach." The European Physical Journal E 44, no. 6 (2021): 80.

Chapter 4

Endoplasmic Reticulum Network Heterogeneity Guides Diffusive Transport and Kinetics

4.1 Abstract

The endoplasmic reticulum (ER) is a dynamic network of interconnected sheets and tubules that orchestrates the distribution of lipids, ions, and proteins throughout the cell. The impact of its complex, dynamic morphology on its function as an intracellular transport hub remains poorly understood. To elucidate the functional consequences of ER network structure and dynamics, we quantify how the heterogeneity of the peripheral ER in COS7 cells affects diffusive protein transport. *In vitro* imaging of photoactivated ER membrane proteins demonstrates their non-uniform spreading to adjacent regions, in a manner consistent with simulations of diffusing particles on extracted network structures. Using a minimal network model to represent tubule rearrangements, we demonstrate that ER network dynamics are sufficiently slow to have little effect on diffusive protein transport. Furthermore, stochastic simulations reveal a novel consequence of ER network heterogeneity: the existence of 'hot spots' where sparse diffusive reactants are more likely to find one another. ER exit sites, specialized domains regulating cargo export from the ER, are shown to be disproportionately located in highly accessible regions, further from the outer boundary of the cell. Combining *in vitro* experiments with analytic

calculations, quantitative image analysis, and computational modeling, we demonstrate how structure guides diffusive protein transport and reactions in the ER.

4.2 Introduction

The eukaryotic cell contains myriad complex structures and compartments, each serving a specialized functional role. These include the tortuous interior of interconnected mitochondria [156], the stacked sheets [157] and tubular networks [22, 80] of the perinuclear and peripheral endoplasmic reticulum (ER), and the intertwined actin and microtubule networks of the cytoskeleton [158, 159, 160]. The morphology of these intracellular structures modulates the long-range active and passive transport of particles within them [161]. For example, the winding cristae of mitochondria slow down the long-range spread of particles [156], while spiral dislocations connecting ER sheets facilitate more rapid diffusive transport [157, 162].

A number of theoretical studies have demonstrated that the architecture of the domain can play an important role in determining reaction rates, a general phenomenon described as 'geometry-controlled kinetics' [47]. Emergent kinetic behaviors such as ultrasensitivity, bistability, and proofreading can be promoted or suppressed when enzyme and reactant diffusion is perturbed by crowding or by association with cellular structures [49, 50, 51]. Additional effects arise when the domain structure is dynamic, leading to time-varying effective diffusivity [52, 53] and broadening the distribution of search times [54].

One important class of intracellular geometries includes network structures, consisting of effectively one-dimensional edges connected at junction nodes. The transport properties of spatial networks [59] have been studied in a variety of contexts, from porous media [58], to neuronal maintenance [163, 56]. For instance, particles diffusing through networks of tubes and containers have been shown to exhibit novel transport properties such as wavelike concentration fluctuations [117], as well as enhanced reaction rates [164].

The peripheral ER [40, 165, 38] and the mitochondrial networks of yeast and mammalian

cells [55, 166] can both be described as spatial networks of interconnected hollow tubules. Studies of search kinetics in these networks have highlighted the importance of network connectivity, as described by the number of loops within the network [55, 45]. The connectivity of the organelles can be biologically perturbed by mutations in ER morphogens [22, 38] and mitochondrial fusion and fission proteins [55, 166]. Prior studies have focused largely on global network architecture and transport properties, such as mean first-passage times averaged over the entire network. Cellular networks, however, are not homogeneous lattices, implying that a significant amount of variability should be expected in local transport to specific regions [67]. This variability has the potential to modulate encounter kinetics and dispersal to different regions of the cell.

The dynamic, interconnected web of the ER plays an important biological role as a delivery network for proteins, ions, and lipids throughout the cell [167, 168, 9, 7]. For example, phospholipids manufactured in the ER, must diffuse through its membrane to contact sites with lipid droplets, mitochondria, and other organelles in order to be transferred to their eventual cellular destinations [5, 7]. Additionally, alteration of network structure through modulating expression of ER morphogens has been shown to affect the magnitude of calcium release, possibly due to altered transport through the ER lumen [167].

The ER also serves as a quality-control hub for newly synthesized proteins destined for secretion [68, 2]. These proteins are co- or post-translationally inserted into the ER lumen or membrane, interact with a variety of ER-resident chaperones to ensure correct folding, and exit the organelle after encountering an ER exit site (ERES). The ERES are punctate, persistent structures which package secretory cargo into COPII-coated vesicles for subsequent transport to the Golgi apparatus [10, 11, 12, 13]. While in the ER, the proteins targeted for secretion engage in diffusive transport to encounter their chaperone binding partners and to find the exit sites. Furthermore, certain steps in the protein quality control pathways are thought to occur in specialized local regions of the ER [169, 170], necessitating transport of proteins into and out of these regions. Given that many of the biological functions of the ER rely on its ability to serve as a topologically isolated transport network throughout the cell, understanding how network

architecture modulates particle transport and encounter kinetics forms an important problem in cell biology.

In this work, we focus on the spatial heterogeneity of the peripheral ER network in mammalian (COS7) cells. We demonstrate that structural variability across individual ER networks translates to heterogeneous diffusive accessibility for different ER regions within the same cell. Live-cell imaging data is used to show that locally photoactivated membrane proteins spread non-uniformly to nearby regions of the ER, in agreement with simulation results that predict preferential transport to better-connected regions of the network. The contribution of dynamic ER network rearrangements is quantified using a minimal network model [39, 40], and shown to have little effect on membrane protein spreading. Furthermore, with the aid of stochastic simulations we demonstrate that the heterogeneity of the ER leads to the formation of 'hot spots' where diffusing reactants are more likely to find each other. In live cells, we additionally find that ER exit sites are preferentially localized to regions of higher accessibility as dictated by network connectivity and proximity to the perinuclear region. By examining the impact of ER network heterogeneity on diffusion-limited reactions and local protein spread, this work sheds light on the structure-function relationship of a biologically crucial organelle.

4.3 Materials and Methods

4.3.1 DNA plasmids

ER plasmids (mCherry_KDEL, KDEL_Venus or BFP_KDEL) were described previously [109, 32, 171]. Plasmids expressing fluorescently tagged COPII proteins: GFP_Sec16s, GFP_Sec23A, GFP_Sec24D, and EYFP_Sec31A were acquired from addgene (gifts from Benjamin Glick #15775, David Stephens #66609 and #66613, Henry Lester #32678) [172, 173, 174]. Generation of PAGFP_Calnexin was performed by PCR amplification of calnexin from mEmerald_Calnexin (gift from Michael Davidson, addgene #54021) using iProof high-fidelity DNA Master mix (Bio-Rad) and primers flanked with Xho1 or BamH1 recognition sites (Primer Fwd:

5'-AGATCTCGAGCTCATGGAAGGGAAGTGGTTGCTG -3' and Primer Rev:
5'-CCGATGGATCCCGCTCTCTTCGTGGCTTTCTGTTTCT-3') according to manufacturer instructions. Amplified DNA was purified using the Monarch Gel Extraction Kit (New England Bioscience) according to manufacturer protocol and digested with Xho1 and BamH1 (NEB). The digested calnexin was then ligated into PAGFP_N1 (gift from Jennifer Lippincott-Schwartz, addgene #11909) [175] using T4 DNA ligase (NEB) according to manufacture protocols. Bacterial clones were screened for insertion of calnexin sequence and confirmed by sequencing.

4.3.2 Photoactivation experiment

COS7 cells were purchased from ATCC and cultured in Dulbecco's modified Eagle's medium (DMEM) supplemented with 10% fetal bovine serum (FBS) and 1% penicillin/streptomycin. For all imaging experiments, COS7 cells were seeded in six-well, plastic-bottom dishes at 7.5×10^4 cells/ml about 16 hours before transfection. Plasmid transfections were performed using lipofectamine 3000, as described previously [176]. The following standard DNA amounts were transfected per mL: 0.2 μg mCherry_KDEL, 0.2 μg BFP_KDEL and 0.4 μg PAGFP_Calnexin. Cells were transferred to 35mm imaging dishes (CellVis) at least 16 hours before imaging.

All photoactivation experiments were performed at the Van Andel Institute Optical Microscopy Core on a Zeiss LSM 880, equipped with an Axio Observer 7 inverted microscope body, stage surround incubation, Airyscan detector, two liquid cooled MA_PMT confocal detectors and one 32-channel GaAsP array confocal detector. Images were acquired with a Plan-Apochromat 63x (NA 1.4) oil objective with 3x optical zoom using Zeiss Zen 2.3 Black Edition software. Photoactivated target ROIs (60x60 pixel ROI) in the peripheral ER network were stimulated with 405 nm light (single pass with 0.51 μsec pixel dwell) to selectively activate defined regions within the peripheral ER. Cells were tracked for at least 2 minutes after stimulation with constant acquisition (0.629 sec/frame) to track diffusion of photoactivated signal into the surrounding ER network.

4.3.3 Image analysis and network structure extraction

The machine learning segmentation toolkit ilastik [110] is employed to segment ER network structures from live-cell images using the mcherry_KDEL marker. A custom-written skeleton tracing subroutine in Matlab [111] is used to extract a network structure from the probability file output by ilastik. This code is publicly provided at https://github.com/lenafabr/networktools and includes data structures for storing the network morphology as a set of nodes connected by edges with curved spatial paths. The networks are manually curated (using a network editing GUI provided as part of the networktools package) to remove unphysical terminal nodes arising from skeletonization artifacts.

For the calculations shown in Fig. 4.1A,C,D,F, and G a circular region of radius 20 μm is cut out from the extracted network structure. In Fig. 4.1B, eight sections of peripheral ER with radius 8.5 μm are used from three different cells. These eight extracted ER networks are again used in the pairwise reaction simulations (Fig. 4.4B-E) and in the Supplemental Material.

4.3.4 Mean first passage times on tubular and reservoir networks

In our base model, mean first passage times (MFPTs) are computed on networks consisting of edges joined at point-like nodes. Details of the computation are outlined in Ref. [67]. In short, we find the splitting probability P_{ik} and waiting time Q_i for a diffusive particle starting at node i to first reach neighboring node k:

$$P_{ik} = \frac{1/\ell_{ik}}{\sum_{j=1}^{d_i} 1/\ell_{ij}}, \quad Q_i = \frac{1}{2D} \cdot \frac{\sum_{j=1}^{d_i} \ell_{ij}}{\sum_{j=1}^{d_i} 1/\ell_{ij}}. \tag{4.1}$$

Here, d_i is the node degree and ℓ_{ik} is the length of the connecting edge. The MFPT from node i to a target node is then given by [67]:

$$\tau_i = \left[(\mathbf{I} - \mathbf{P})^{-1} \cdot \mathbf{Q} \right]_i, \tag{4.2}$$

where $\mathbf{I}$ is the identity matrix, and the matrix and vector $\mathbf{P}, \mathbf{Q}$ are defined by Eq. 4.1, with the row and column correponding to the target removed. The GMFPT is defined as the MFPT to a given target k, averaged over all starting nodes i.

In this work we also introduce a novel extension to the base model that allows calculation of search times on networks with enlarged nodes or 'reservoirs' (details in Supplemental Material Section S2). The model represents the motion of particles between disk-shaped reservoirs and connecting tubules as transitions between distinct spatial states. Waiting times for transition out of the reservoir are set by two-dimensional diffusive escape into the narrow tube entrances. The additional states associated with trapping in the reservoirs are included in the transition matrix $\mathbf{P}$ and waiting time vector $\mathbf{Q}$ to compute the MFPTs according to Eq. 4.2.

We consider two extended network models. In Supplemental Fig. S3, we randomly select nodes to be expanded into larger reservoirs. GMFPTs are computed to both the point-like remaining nodes of the network and to a central target inside each reservoir, where the radius of the target is equal to the network tubule radius. Particles are assumed to start on the nodes, in proportion to the node area. In Fig. 4.5 we introduce a single large disk-like reservoir representing the perinuclear region. GMFPTs are computed for particles starting uniformly distributed along the network edges and the reservoir, in proportion to the associated surface area for the tubules and the disk. Details for computing MFPTs for a particle starting on a network edge can be found in Ref. [67].

4.3.5 Analysis of photoactivated spreading data

Imaging datasets for 9 individual cells are selected for analysis, each of which has a photoactivation region surrounded by a well-defined tubular network structure with primarily 3-way junctions. The net signal over time is computed in 10 distinct wedge regions comprising an annulus around the photoactivation region with inner radius 3.5 μm and outer radius 6 μm. The photoactivated signal in wedge j at time i is defined as w_{ij}^{PAGFP}. The fractional signal is then given by $f_{ij}^{\mathrm{PAGFP}} = w_{ij}^{\mathrm{PAGFP}} / P_0^{\mathrm{PAGFP}}$ where P_0^{PAGFP} is the total initial signal within the

photoactivated zone. We find the slope ('signal arrival rate') of the fractional signal via a linear fit over the first 10 seconds of imaging time following photoactivation.

Two rounds of filtering are applied to ensure a meaningful relationship between the photoactivated signal dynamics and the observed network structure. The first filter removes regions with extremely rapid and/or large fluctuations in the ER signal. We calculate the time-variance in the fractional signal in each wedge as

$$V_j = \mathrm{var}_i(w_{ij}^{\mathrm{PAGFP}}/m_i^{\mathrm{PAGFP}}), \tag{4.3}$$

where $m_i^{\mathrm{PAGFP}} = \sum_j w_{ij}^{\mathrm{PAGFP}}$ is the total signal in the annular region at time i. Given the distribution of these time-variances, a threshold of $2.5 \times (\mathrm{MAD} \times 1.4826)$, where MAD is the median absolute deviation, is used to define outliers with extreme ER dynamics, in keeping with commonly used outlier detection methods [177].

The second round of filtering removes instances where network extraction does not accurately capture the underlying ER morphology. For example, small peripheral sheet regions, expanded junctions, or dense tubular matrices [80] can complicate the extraction of a well-defined network structure. Outlier regions are defined as those where the extracted total tubule length and the ER marker (mCherry_KDEL) signal levels are mismatched. Specifically, we compute the time-averaged fractional mCherry_KDEL signal for each wedge region in each cell as $s_j = \left\langle w_{ij}^{\mathrm{mCherry}}/m_i^{\mathrm{mCherry}} \right\rangle_i$. A linear fit is performed relating s_j with the total extracted network length for each wedge, averaged over time. Any wedge with a residual above $2.5 \times (\mathrm{MAD} \times 1.4826)$ is filtered out of the analysis. Wedge regions filtered out due to either criterion are shown as gray dots in Fig. 4.2E-G.

4.3.6 Simulations of photoactivation on static networks

For each frame in a photoactivation video, the ER network structure is extracted from the mCherry_KDEL fluorescence channel, as described in the Image Analysis section. On

each individual network structure, simulations of diffusing particles are conducted via a kinetic Monte Carlo method, as described in prior work [67]. Briefly, analytically computed propagator functions are used to sample the time required for each particle to transition between neighboring nodes and edges, obviating any artifacts associated with a fixed time discretization. This method allows the particle to propagate in larger timesteps than would be achievable through classic Brownian dynamics simulations on a network.

Batches of $N = 10000$ particles are initiated within the experimentally photoactivated region, a 3×3 μm patch in the peripheral ER. Particles propagate through the network with a diffusivity of $D = 1$ $\mu\text{m}^2/\text{s}$, consistent with previous measurements of ER membrane protein diffusivity [165]. All particle positions are saved at a frame rate matching the experimental imaging rate, $dt = 0.629$s.

To process the simulated data, we define individual wedge regions of the same size and location as in the experimental images and analyze the number of particles in each. Note that each simulation is run on a static network extracted from a single frame (k) of the experimental image. The simulated signal in each wedge (w_{kij}^{sim}) is then defined as the total number of particles in wedge j and time point i on the network extracted from frame k, and the fractional signal (plotted in Fig. 4.2D) is $f_{kij}^{\text{sim}} = w_{kij}^{\text{sim}}/N$.

We next average this fractional signal over the different networks, defining $f_{ij}^{\text{sim}} = \left\langle f_{kij}^{\text{sim}} \right\rangle_k$ (see Supplemental Material Fig. S2A.iii for example averaged signal vs time curves). The resulting values are used to find the signal arrival rate (slope over first 10 seconds), exactly as for experimental data. Alternative methods for incorporating the time-varying ER network structure are considered in the Supplemental Material.

The simulations make it possible to incorporate a range of values for the particle diffusivity. We accomplish this by rescaling the simulation time in our analysis, which leads to a rescaling of the diffusivity (assuming static networks). For example, to test whether $D_{\text{eff}} = 0.5$ $\mu\text{m}^2/\text{s}$ is a better representation of the protein diffusivity than $D_{\text{orig}} = 1$ $\mu\text{m}^2/\text{s}$, we can find the slope

of f_{ij}^{sim} over time $T_{\text{scale}} = \frac{D_{\text{eff}}}{D_{\text{orig}}} \times 10 \text{ s} = 5 \text{ s}$. The slope is then multiplied by $\frac{D_{\text{orig}}}{D_{\text{eff}}}$ to arrive at a simulated arrival rate with an effective diffusivity of $D_{\text{eff}} = 0.5\ \mu\text{m}^2/\text{s}$.

We perform a linear fit of the rescaled simulated rates to the experimental protein arrival rates (slopes over 10 s). Repeating over a range of effective diffusivities, the value of D_{eff} with the optimal fit indicates the best estimate of ER membrane protein diffusivity given the photoactivated spreading data.

4.3.7 Minimal model for dynamic ER networks

To estimate the effects of ER network rearrangements on particle spreading, we conduct Brownian dynamics simulations on synthetic dynamic networks. To represent the dynamic network, we use a modified version of the previously published 'minimal network model' [39, 40]. In this model, the network consists of mobile nodes connected by edges, where the node positions $\mathbf{x}_i(t)$ obey an overdamped Langevin equation

$$\frac{d\mathbf{x}_i}{dt} = -b\nabla f(\mathbf{x}_i) + \sqrt{2D_n}\eta(t), \tag{4.4}$$

where $D_n \approx 10^{-3}\ \mu\text{m}^2/\text{s}$ [40] is the node diffusivity, b is the node mobility in units of μm/s, and $f(\mathbf{x}_i)$ is the total edge length attached to each node. Specifically, $f(\mathbf{x}) = \sum_{j=1}^{d} \left|\mathbf{x} - \mathbf{y}_j\right|$, where the sum is over neighbor nodes and $\mathbf{y}_j$ are the neighbor positions. The stochastic variable $\eta(t)$ is a Gaussian distributed noise term with mean zero and standard deviation 1. This model represents a network of edges which are under a constant tension, driving a minimization of their length.

As the edges of the network shrink, neighboring nodes approach each other. When two nodes are sufficiently close together, topological rearrangements of network connectivity can occur. If the two nodes are both degree 3 junctions, they undergo a T1 rearrangement [33] if and only if this decreases the total edge length. If one of the nodes has degree 2, or if they are connected by two edges (forming a short loop), then the two nodes can fuse together into a single node. The combination of these processes allows for ring-closure events, as observed in live-cell

imaging of ER dynamics [71, 9].

To maintain a steady-state network structure, new edges are generated by a tube spawning and growth process. A new tube spawns at a fixed growth rate per existing total edge length (k, units of $s^{-1}\mu m^{-1}$). The new tube location is uniformly selected along existing edges. The nascent tube grows at a right angle from the parent edge, with fixed velocity $v = 2$ μm/s, comparable to rapid rates observed in dynamic ER images [31, 13]. When the tip of a nascent tube crosses an existing tube, it stops growing and fuses to form a new junction node.

Similar to [39], the balance between new tubule growth and shrinking due to length minimization enables the dynamic network to reach a stable steady-state. Of the parameters in the model, the diffusivity is sufficiently low ($D \ll v\ell$, where $\ell \approx 1$ μm is the characteristic edge length) to have little effect on network structure. Additionally, the tubule growth speed ($v \gg b$) is high enough that newly spawned tubules fuse much quicker than the node rearrangement timescales. The network structure is thus largely determined by the remaining two parameters k, b, which are set to match observations of COS7 ER in live-cell images.

The approximate growth rate k is extracted from videos of COS7 peripheral ER, labeled with 0.2 μg KDEL_Venus (transfected as described above) and imaged on the Zeiss LSM 880 at a frame rate of 0.315 s, by manually counting new growth events (Supplemental Video 4.3). The number of growth events in a region of size 10 μm $\times$ 10 μm is manually counted over time interval 63s. This number is normalized by the time interval and the time-averaged total segmented ER length within the region, giving: $k \approx 0.005$ $\mu m^{-1}s^{-1}$.

Dimensional analysis indicates that the average steady-state edge length in the network scales as $\ell \sim \sqrt{b/k}$. We tune the node mobility b to set a typical ER network edge length $\ell \approx 1$ μm [165], corresponding to an estimate of $b = 0.05$ μm/s.

The resulting dynamic network model thus has tubule lengths and turnover timescales that approximately represent those of the COS7 ER ('normal ER model'). For comparison, we consider also a model where b and k are both increased by $2\times$, allowing for more rapid turnover but the same steady-state structure ('fast ER model').

4.3.8 Simulating photoactivated spread on the dynamic network model

Diffusive particles ($N = 10000$) are simulated on the dynamic network using Brownian dynamics, with particles moving along the network edges in discrete timesteps $dt = 10^{-3}$ s, with diffusivity $D = 1\ \mu\text{m}^2/\text{s}$, and network structure updated at each timestep. After each network update, the particle position is projected to the closest location in the new network. The network architecture is first evolved for a total time of 1000s to allow it to reach steady state prior to initiating the diffusive particles. The particles are placed within a square $3\ \mu\text{m} \times 3\ \mu\text{m}$ region of the network and the joint simulations of particle and network evolution then proceed for an additional 15 s of simulated time.

The number of particles arriving in each wedge region surrounding the starting center is analyzed on both the dynamically evolving network and on each individual static network structure extracted at 0.6 s intervals from the simulation. The signal arrival rates are obtained as described in the previous section.

4.3.9 Paired particle simulations

Simulations of reactive particle pairs are run using the propagator-based approach, which enables particles to hop rapidly from node to node of the network until they come within the same neighborhood of each other. Details of the methodology, including the appropriate propagator functions for two reactive particles on the same edge, are provided in prior work [67]. Each simulation is run until the two particles encounter each other, and the reaction position on the network is recorded. A total of $N = 160000$ particles are simulated on each network structure. The ER network structures are extracted from COS7 cell imaging data as described in the Image Analysis section.

Two other families of network are also analyzed. Eight circular honeycomb networks are generated, each with the same diameter and total edge length as one of the eight ER structures analyzed. Mikado networks are generated by scattering N_{rod} randomly oriented rods of length

L_{rod} in a square of size L_{space} x L_{space}. The intersections of these rods define the nodes of the network, the segments of rods between intersections define the edges of the network. This algorithm generates highly heterogeneous networks with a density that is tunable by changing any of the three input parameters [178]. However, Mikado networks tend to have degree 4 junctions, whereas ER (and honeycomb) networks are composed of mostly degree 3 junctions. Our modification to the Mikado networks is thus to remove degree 4 nodes by iteratively removing 1 random edge from a randomly chosen degree 4 node until all nodes in the network have degree 3 or less. The Mikado parameters are chosen to be $N_{\text{rod}} = 80$, $L_{\text{rod}} = 12$ μm, and $L_{\text{space}} = 24$ μm and a circular portion of the network is extracted with diameter 18 μm, matching the circular ER networks. We generate many copies of these circular modified Mikado networks and select for analysis only those which have a total length within 5% of the corresponding ER network.

4.3.10 ERES localization on ER network

COS7 cells were seeded in plastic 6-well dishes and transfected as described in the photoactivation experiment section. Cells were then imaged as previously described [13]. The following standard amounts of DNA were transfected per mL: 0.1 μg GFP_Sec16s, 0.1 μg GFP_Sec23a, 0.1 μg GFP_Sec24d, 0.1 μg EYFP_Sec31a, 0.2 μg mcherry_KDEL. Images were acquired on inverted fluorescent microscope (TE2000-U; Nikon) equipped with a 100x oil objective (NA 1.4) on an electron-multiplying charge coupled device (CCD) camera (Andor). Live cell imaging was performed at 37°C following media change to pre-warmed imaging media (fluorobrite DMEM (Invitrogen) + 10% FBS).

Images of 22 different COS7 cells are analyzed as described in the Image Analysis section to extract the peripheral ER network structure. The perinuclear region is manually excised from each one. ERES locations are identified as puncta in the GFP or EYFP fluorescent signal using a previously published implementation of the standard particle localization algorithm by Crocker and Grier [179, 180]. We identify a total of 1443 peripheral and 2327 perinuclear ERES. The

peripheral puncta are projected onto the nearest point along the extracted network structure.

To convert these structures into reservoir networks (model described in Supplemental Material Section S2), the centroid of the nodes bounding the excised perinuclear region is set to be the center of the reservoir. The average distance of the bounding nodes to the centroid determines the radius of the reservoir, R_+. Each bounding node is then connected to the reservoir via a tubule of length equal to the mean edge length of the network.

The GMFPT to each projected ERES is computed for particles starting uniformly distributed across the network. For comparison, an equivalent number of target points are selected uniformly at random along the edges of each network structure, and the GMFPT is computed to each of those points individually.

4.4 Results and Discussion

4.4.1 ER network structures exhibit spatially heterogeneous accessibility

The peripheral endoplasmic reticulum forms an intricate web of tubules, with primarily three-way junctions scattered at varying densities across the cell periphery. We aim to characterize the heterogeneity of the network structure and its effects on the accessibility of different regions by particles diffusing on the network.

ER network morphologies are extracted from confocal images of the peripheral ER in cultured COS7 cells (Fig. 4.1A), where these network structures are largely planar. The network structure is simplified into effectively one-dimensional edges (not necessarily straight), connected at point-like nodes. Although more complex peripheral structures, including hole-studded sheets [155] and dense localized matrices[80], have been observed, we focus here on regions composed primarily of well-defined tubules and junctions. In Supplemental Material, we show that enlarged junctions between the tubules do not substantially affect the results (Fig. S3).

The ER density in different spatial regions can be characterized by computing the local edge length $L_{\mathrm{loc}}(x;\sigma)$, defined as the total length of network tubules that falls within distance

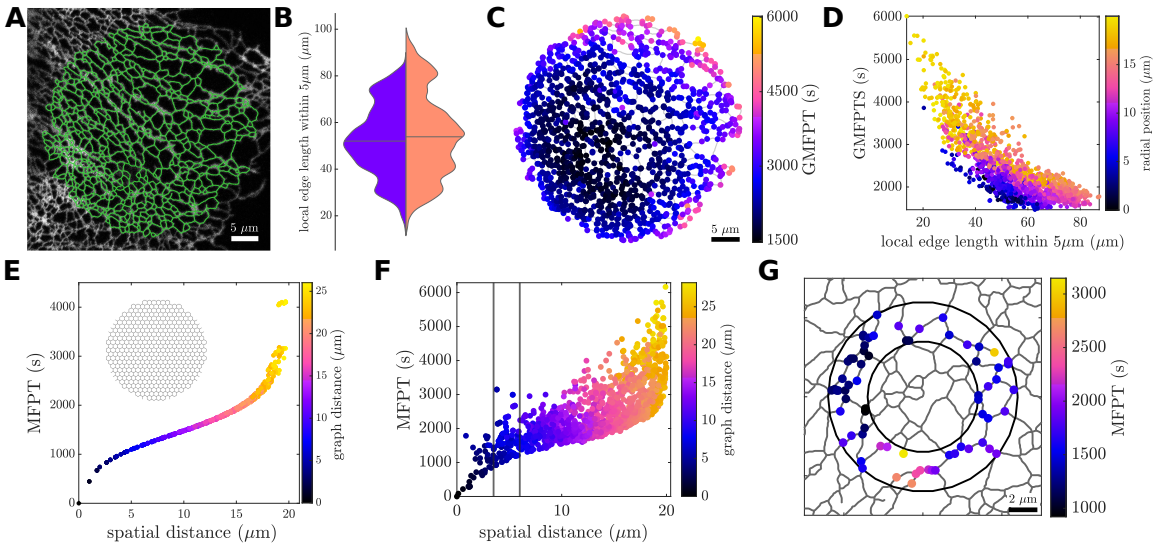

Figure 4.1. Analytic mean first passage times as a measure of accessibility for different regions of the ER. (A) Confocal image of COS7 cell expressing fluorescent ER marker (KDEL_Venus, gray) with extracted network structure overlay (green). (B) The distribution of local edge lengths in one cell (left) is similar to the corresponding distribution across multiple cells (right). (C) Global mean first passage times (GMFPTs) to nodes on the example COS7 ER network shown in A. (D) GMFPT scales inversely with local edge length, color denotes radial position from center of network. (E) MFPT to each network node for particles diffusing outward from the center of a circular honeycomb network. (F) MFPTs to all network nodes for particles diffusing outward from the center of the example ER network. Vertical lines highlight heterogeneity in a ring from $3.5-6$ μm around the center. (G) MFPTs for nodes in the ring from $3.5-6$ μm, as highlighted in F. Particle diffusivity is set to $D = 1$ $\mu\text{m}^2/\text{s}$ throughout.

$\sigma = 5$ μm of position x. We sample local edge length for random points scattered across the domain of an example network (shown in Fig. 4.1A). The values of $L_{\text{loc}}(x;\sigma)$ span one order of magnitude, demonstrating substantial spatial heterogeneity in the ER density (Fig. 4.1B). Notably, spatial variation in the local edge length within a single network is comparable to the variation between networks extracted from different cells.

While local edge length provides a purely structural metric of heterogeneity, we further consider the consequences of network variability on the diffusive transport of particles within the ER. One useful metric for quantifying search efficiency on spatial networks is the global mean first passage time (GMFPT) [45], which gives the mean first passage time for a diffusing particle to reach a given node in the network, averaged over all starting nodes. This quantity can

be computed analytically from the edge lengths and topology of the network [67] (see Methods).

The GMFPTs for different nodes in a single ER network can vary substantially (Fig. 4.1C). Nodes near the boundary have a higher GMFPT, whereas more centrally located nodes and those in denser regions of the network exhibit the lowest GMFPTs. Some of the variation in GMFPT can be explained by the local edge length surrounding a node, as well as proximity to the boundary of the domain (Fig. 4.1D), both a measure of centrality within the network [59]. However, even nodes with similar local edge lengths and radial position can have GMFPTs that vary by a factor of 2. We note that the ER networks form a highly-looped structure composed primarily of 3-way junctions, with less than 5% terminal nodes. Thus, although network search times are known to vary with node degree [181], the degree of each node is insufficient to account for the observed variability of the GMFPTs. Furthermore, we consider a modified network where a randomly selected subset of node junctions is enlarged, with a target of size comparable to the tube width placed in their center. As shown in Supplemental Fig. S3, targets inside the enlarged nodes have similar search times to targets on ordinary tubule junctions. Thus, the heterogeneity in search times appears to be dictated by the edge connectivity of the network rather than by junction size.

Individual mean first passage times (MFPTs) between pairs of nodes in the network can be used to further assess heterogeneity in local transport processes. The MFPT for a particle diffusing outward from a central point to each possible target node in a uniform honeycomb network exhibits a characteristic scaling with distance, as shown in Fig. 4.1E. Unsurprisingly, nodes that are located farther from the source tend to have higher MFPTs, with the search time increasing exponentially for the most distant population of nodes. This particular scaling of the diffusive search time relative to distance has also been observed for particles that hop actively across edges in planar network structures [63]. Similar scaling is found in diffusive search for targets on the ER (Fig. 4.1F). However, the heterogeneity of the ER network structure gives rise to a broad range of mean search times for nodes at similar distances from the source. A factor of 3 difference is observed for nodes that fall within a ring from 3.5 μm – 6 μm from the center

(Fig. 4.1F, G).

Overall, we use analytic mean first passage times as a measure of accessibility for different regions of the ER, either by particles starting throughout the network, or those originating from a localized source. This accessibility is shown to vary between different regions of an ER network, due to the heterogeneous density and connectivity patterns of the tubules.

4.4.2 Network morphology governs the nonuniform spread of photoactivated proteins

Figure 4.2. Spreading of localized bolus of particles over the ER network. (A) ER membrane protein PAGFP_Calnexin (green) is pulse-activated in a local region, while ER luminal marker mCherry_KDEL (red) serves to visualize network structure. Equidistant surrounding regions (colored wedges) are used to analyze signal spread. (B) Photoactivated signal arriving in each analyzed region, normalized by initial total signal in photoactivated zone. Gray region denotes time prior to photoactivation. (C) Snapshots of simulations on frozen ER structures extracted from first frame in A. (D) Simulated particle counts arriving in individual analysis regions, normalized by total number of particles. Gray region denotes time prior to photoactivation. (E) Correlation between signal arrival rates (slopes of signal vs time curves) for experimental and simulated data. Color indicates cell (N=9). Inset: simulated protein arrival rates best match experimental arrival rates when effective diffusivity is rescaled from $D_{\text{orig}} = 1\ \mu\text{m}^2/\text{s}$ to $D_{\text{eff}} = 1.3\ \mu\text{m}^2/\text{s}$ (dashed line). (F) Correlation of experimental signal arrival rate in individual regions versus the fraction of ER marker signal in that region. (G) Correlation of experimental signal arrival rate with the number of edges intersecting the boundary of each region. Regions removed due to filtering are shown in gray in E-G.

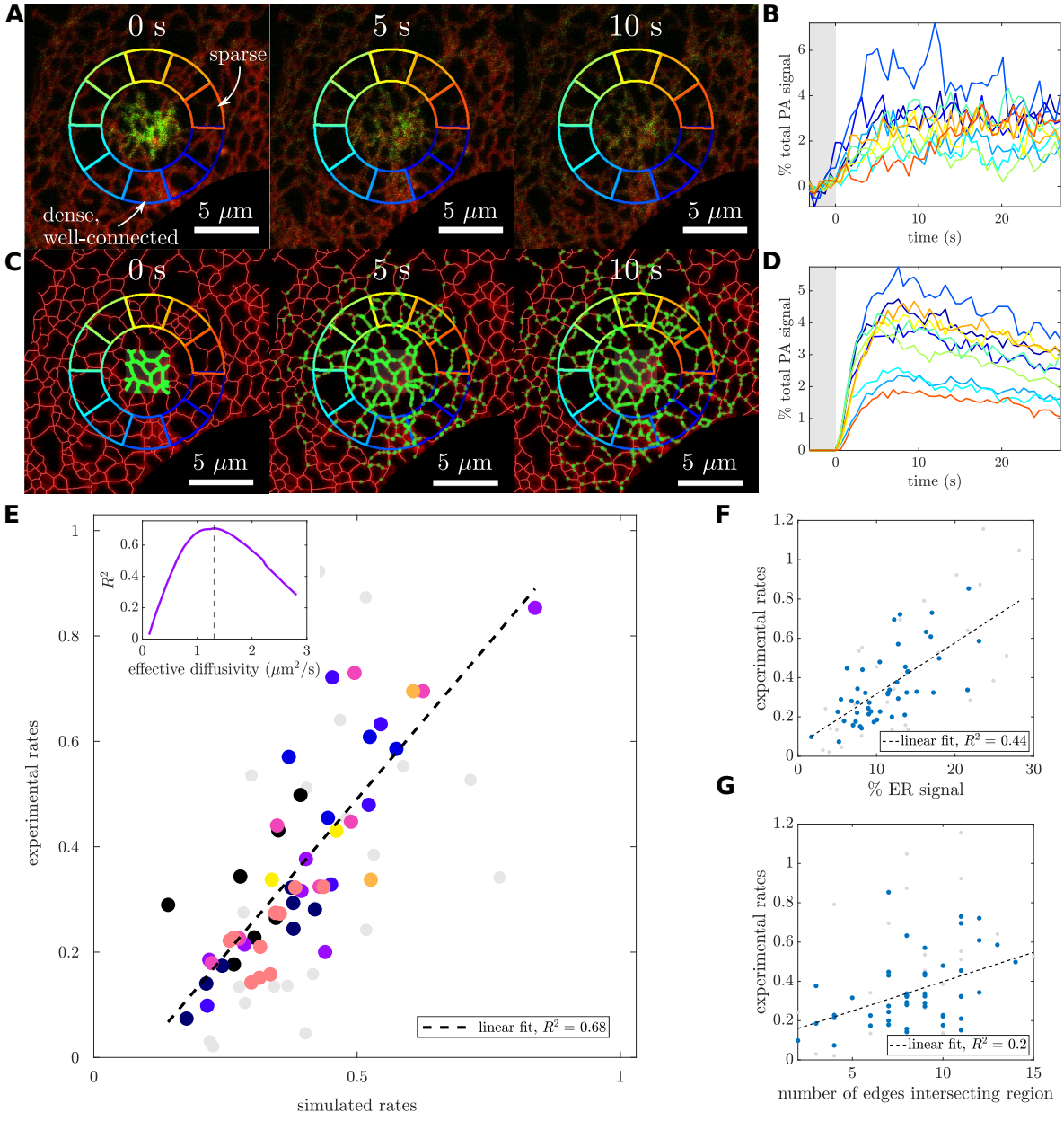
A
0 s
5 s
10 s
sparse
dense,
well-connected
5 μm
B
% total PA signal
time (s)
C
D
E
effective diffusivity (μm²/s)
R^2
experimental rates
simulated rates
linear fit, $R^2 = 0.68$
F
% ER signal
linear fit, $R^2 = 0.44$
G
number of edges intersecting region
linear fit, $R^2 = 0.2$

Although mean first passage times are a convenient, easily computed metric of diffusive accessibility, they are difficult to probe experimentally. To directly observe the heterogeneity of diffusive spreading within the ER, we consider instead the short-time rate of arrival to nearby regions surrounding a particle source. This process is visualized by photoactivating ER membrane-associated proteins within a localized region of the network and watching their spread into surrounding regions. We note that past measurements of single-particle trajectories [165] and bulk spreading [167] of several ER membrane proteins have demonstrated that they undergo diffusive dynamics along the tubules of the peripheral ER. By contrast, aqueous proteins in the ER lumen may in some cases exhibit rapid active motion between neighboring junctions [130, 167]. Such active motion can substantially alter long-range transport across a network [63], and we thus do not include luminal proteins in this study.

Cultured COS7 cells are transfected with PAGFP_Calnexin, a membrane-bound ER protein in the ER with a photoactivatable fluorescent tag, as well as mCherry_KDEL as a general marker for ER structure. A single pass photoactivating pulse is applied in a 3 μm $\times$ 3 μm square of the peripheral ER. Several frames from an example video (Supplemental Video 4.1) are shown in Fig. 4.2A with mCherry_KDEL in red and the PAGFP_Calnexin in green. The initial dense bolus of photoactivated proteins can be seen spreading outward through the network. We track the signal in individual small regions located equidistant from the photoactivation site. Diffusive spreading of particles over a homogeneous continuum would be expected to yield similar time-courses of signal arrival to each of these regions. However, the observed PAGFP fluorescence signal over time varies substantially between the individual wedges in a single cell (Fig. 4.2B). This variability can be attributed to the heterogeneous distribution and connectivity of the ER tubules. Intuitively, the blue region contains dense, highly connected tubules and has the strongest and fastest-growing photoactivation signal. By contrast, the orange region is poorly connected to the activation site and exhibits the smallest initial signal growth.

To account for the observed differences in signal arrival rates due to ER morphology, we extracted the ER network structure in the vicinity of the photoactivation site and carried

out agent-based simulations of diffusing particles initiated at the site (Fig. 4.2C, Supplemental Video 2). Quantifying the number of simulated particles accumulating in each region over time allows for a direct comparison between simulated and observed fluorescent signal. For both the experimental and simulated data, we normalize the measured signal in each region by the initial total signal within a disk of 3.5 μm radius centered on the photoactivation zone (inner circle in Fig. 4.2A,C). Thus, the reported signal traces are given in terms of the fraction of initially photoactivated particles present in a given region at a given time. The normalized simulated signal (Fig. 4.2D) exhibits similar behavior to the experimental results, with well-connected dense regions receiving more signal faster than poorly-connected and sparse ER regions.

To partially incorporate the effect of ER network rearrangement over time, the photoactivation simulations are run on network structures extracted for every frame of the experimental movie (at time interval 0.6s). The signal over time is then averaged across the ensemble of simulations on all of these different network structures. This ensemble-averaged simulated signal is used in the subsequent analysis. Analogous results using only a single network structure can be found in the Supplemental Material.

To quantitatively compare protein arrival rates in the experimental and simulated ER networks, we extract the slope of the normalized signal curves up to 10 seconds following photoactivation. These slopes (referred to as 'arrival rates') serve as a simple metric that provides information about the spatial heterogeneity of protein spreading around the photoactivation site. Because our simulations are carried out on network structures extracted from the experimental images, it is possible to directly compare the rate of signal arrival in matched regions between experimental and simulated data (Fig. 4.2E). Regions where the extracted network length was a poor match for the observed ER marker (mCherry_KDEL) fluorescence, or where the ER marker showed large fluctuations over time, were filtered out of the analysis (gray dots; see Methods for details). Notably, the variability of measured rates between regions within each individual cell (same color dots) is comparable to the inter-cell variability (different color dots), indicating that the arrival rates are similarly heterogeneous in all the observed cells. The experimental

and simulated arrival rates show a direct correlation: $R^2 = 0.68$, obtained from a linear fit. The high correlation implies that diffusive particle motion over an ER network is a good predictor of signal arrival to different regions.

Notably, the simulation time can be rescaled to effectively represent particles of different diffusivity (see Methods for details). We compare the correlation of signal arrival rates between experimental measurements and simulations with different time-scaling. The simulations which best correlate with experimental values correspond to a particle diffusivity of $D_{\text{eff}} \approx 1.3\ \mu\text{m}^2/\text{s}$ (Fig. 4.2E, inset), a value that is similar in magnitude to previous measurements of diffusivity via single-particle tracking for other ER membrane proteins [165]. This result demonstrates that particle diffusivity in the ER can be measured by quantifying signal arrival rates to different structural regions regions of network, all located relatively close to the photoactivated zone, without the need for tracking longer-range spread across the cell [167].

In order to test whether particle diffusion simulations are more predictive than simpler metrics of network structure, we also compare the experimental arrival rates to the mCherry_KDEL ER signal in each region. A linear fit (Fig. 4.2F) demonstrates there is some correlation between the two ($R^2 = 0.44$), but variation in the ER volume within each region (as measured by mCherry_KDEL signal) cannot capture the full variability in protein spreading rates. A simple metric for local connectivity, the number of edges crossing the boundary of each wedge region, is shown to be roughly correlated (Fig. 4.2G, $R^2 = 0.2$), but also does not provide a strong predictor of protein arrival rates. Thus, the distribution of protein spreading rates in live cells is best modeled by simulations which take into account not just the local ER density in a region, but also the connectivity of the surrounding network together with the dynamics of diffusive particles moving through this network.

4.4.3 Slow ER network dynamics have little effect on particle spreading

The ER network in a living cell is itself a dynamic structure, with network rearrangements occurring over tens-of-second timescales as a result of attachment to motile organelles, molecular

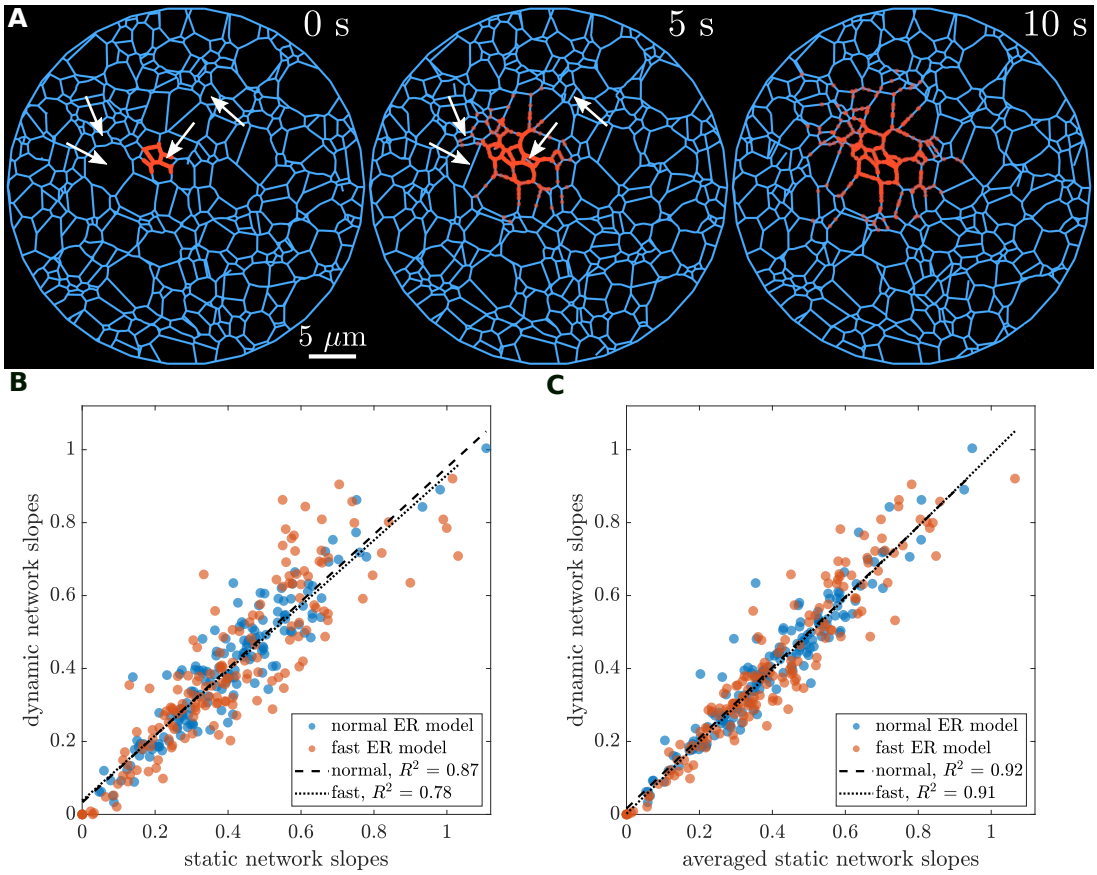

Figure 4.3. ER network dynamics does not substantially affect particle spreading. (A) Snapshots from simulation of diffusing particles spreading from a local region, on a minimal network dynamic model. Network edges are blue and a subset (500) of the simulated particles ($D = 1\ \mu\text{m}^2/\text{s}$) are shown in orange. White arrows highlight several new edges that grew between first and second snapshots. (B) Correlation of signal arrival rate (slope of signal-vs-time curves) to individual regions, comparing simulations on a single static network structure and on dynamic minimal network model with turnover timescales comparable to ER dynamics (blue) or 2× faster (red). (C) Comparison of signal arrival rates for simulation on a dynamic network versus simulations of particles diffusing on a static network, averaged over static structures from individual snapshots of the minimal network. The average static rates are obtained in the same manner as in the analysis of experimental data.

motors, and growing microtubule tips [9, 28, 31]. In comparing the measured rates of protein spread to simulations of diffusing particles (Fig. 4.2E), we account for time variation in ER architecture by averaging over network structures extracted from each frame.

To gain a better sense of how ER tubule dynamics may contribute to the spread of photoactivated proteins, we incorporate network rearrangements directly into our simulations, by

treating the ER as a 'minimal network' with tubules subject to growth and constant tension [39]. These synthetic dynamic networks (described in the Methods) mimic the rearrangements of the ER over time, including new tubule growth, junction sliding, and the merging of junctions.

The two parameters primarily responsible for determining the equilibrium properties are node mobility (units of μm/s, sets speed with which nodes rearrange) and new tubule growth rate (units of $\mu m^{-1}s^{-1}$, rate at which new tubules are pulled out of existing tubules). Other parameters, such as node diffusivity and new tubule growth speed play a secondary role in the parameter regimes considered here. Input parameters to the model are set so that network properties at equilibrium match the ER network in COS7 cells. Specifically, the modeled networks match the measured rate of new tubule formation (Supplemental Video 4.3) and the steady-state average edge length in the network. For comparison, we also ran simulations of networks that exhibit faster dynamics, with both tubule growth rate and node mobility increased by a factor of 2. These faster networks have the same steady-state network structure but rearrange twice as rapidly.

For each of these dynamic networks, 16 separate photoactivation events are simulated in different regions of the network. Particles are initiated within 33 μm $\times$ 3 μm patches and allowed to diffuse through the structure either on a static network or concurrently with the network dynamics (Fig. 4.3A, Supplemental Video 4.4). We compare the rate of particles arriving to equidistant regions surrounding the initiation zone both with and without network dynamics.

When the particle simulations are run on a single static network structure, the arrival rates are moderately well-correlated ($R^2 = 0.87$) with the rates observed for simulations on dynamic networks (Fig. 4.3B). Faster dynamics in the synthetic networks reduces this correlation to $R^2 = 0.78$. Intuitively, as the rearrangements occur more quickly, diffusive particles encounter more extensive changes in structure during the 10-second timescale of the measurement.

Notably, even when network dynamics are twice as rapid as the experimentally observed dynamics of the ER network, the static network approximation is a good predictor for particle

arrival rates. We can estimate the importance of active network rearrangements versus the diffusive motion of the particles by considering an effective Péclet number for the system. The mobility parameter for the dynamic networks ($b = 0.05$ μm/s) sets a typical velocity for tension-driven sliding. Over a length scale of 10 μm (corresponding to the diameter of the analyzed region), the corresponding Péclet number for a protein within the network is $\mathrm{Pe} = vL/D \approx 0.5$. Doubling the rate of ER rearrangement doubles this Péclet number. Because this dimensionless quantity is close to or below $\mathrm{Pe} = 1$, the motion of the particles is dominated by their diffusivity rather than by the tubule rearrangement dynamics.

The moderate effect of network dynamics on particle spreading can be partly accounted for by running simulations on many individual static network structures extracted at different points in time. We perform this analysis using snapshots of our simulated dynamic networks and averaging the signal in each region at each time point. For this ensemble-averaged data, the arrival rates on static and dynamic networks become more closely correlated (Fig. 4.3C), even in the case of rapid network rearrangements ($R^2 = 0.91$). Thus, the effect of network dynamics is almost entirely accounted for by averaging multiple static simulations on consecutive network structures. These results on synthetic dynamic networks validate the use of the same ensemble averaging approach when analyzing experimental data.

4.4.4 ER structure directs reaction locations

The endoplasmic reticulum does more than simply serve as a transport hub for proteins, lipids and ions; it also plays a role in protein synthesis and quality control [68, 170], as well as forming functionally important contact sites with other organelles [7]. The formation of reactive complexes, exit sites for protein export, and contact site assemblies requires multiple intra-ER particles to find each other within the network. In order to better understand how diffusion-mediated biochemical reactions are impacted by ER morphology, we simulate reactive particle pairs diffusing on extracted ER network structures (Fig. 4.4A). From these simulations, both the spatial locations of reactions on the network as well as the distribution of reaction times

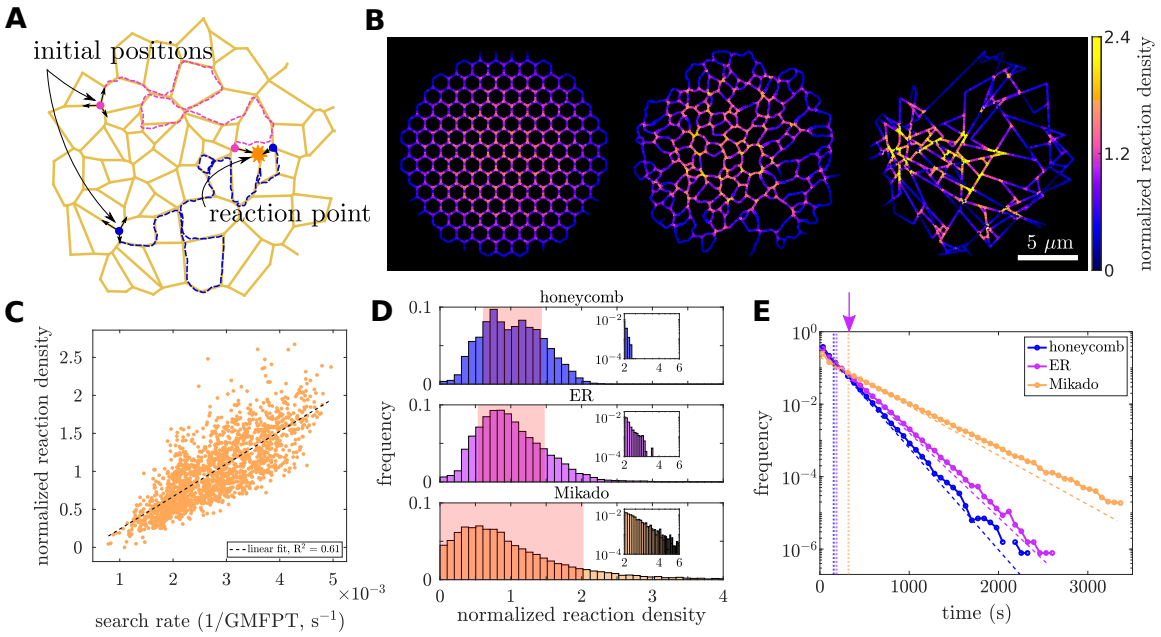

Figure 4.4. ER heterogeneity leads to hot spots of paired particle encounters. (A) Schematic of paired particle simulations. Pairs of particles (pink and blue circles) diffuse through the network (dashed lines indicate trajectories) until they encounter and react. (B) Normalized reaction density on three example networks, each with similar total edge length and spatial size. For each discretized segment of network, the fraction of simulated reactions occurring within that segment is normalized by the fraction of total edge length contained within that segment. Left panel, a homogeneous honeycomb network with the same average edge length as the ER network in the middle panel. Middle panel, ER network is extracted from a section of COS7 peripheral ER, and exhibits regions of higher reaction density than the homogeneous honeycomb (bright yellow segments). In the right panel, the normalized reaction density on a highly heterogeneous synthetic, Mikado-like network, exhibiting even more pronounced hot spots than the ER. (C) Paired reaction density on each segment of the ER is roughly correlated with the inverse of the global mean first passage time (GMFPT) to that segment. (D) Distribution of reaction rate densities for all discretized segments in honeycomb, ER, and Mikado-like networks, showing increasing heterogeneity in the densities. Insets show long tail of distribution plotted on log-log axes. Mean for each distribution is one, red overlay denotes standard deviation. (E) Distributions of paired reaction times in the three network structures. Dotted lines mark the mean reaction time. Dashed lines show exponential decay for a Poisson process with the same mean. The target-averaged GMFPT on the ER networks indicated by the purple arrow is more than twice the mean pair reaction time.

are extracted.

Many previous studies of diffusive processes on networks have focused on the temporal properties of reactions or exit times (e.g. MFPTs, extreme statistics, and full FPT distributions [67,

55, 54]), without considering in detail where those reactions occur. Here, we provide fresh insight by analyzing the spatial locations, as well as temporal distributions, of pair-wise reactions on the ER. Pairs of particles are distributed randomly across the network to begin the simulation. Each pair diffuses along the edges of the network until the two particles come into contact with one another. At this point, they react and the position and time of reaction is recorded. The network edges are meshed into segments of length $\ell \approx 0.2$ μm, and the normalized reaction density in mesh cell i is defined as:

$$\gamma_i = \frac{\text{\# of reactions in cell } i}{\text{\# of particle pairs}} \times \frac{\text{total network length}}{\ell}. \tag{4.5}$$

When averaged over an entire network, $\langle \gamma \rangle = 1$. Simulations on the ER network structure demonstrate that paired particle reaction locations are heterogeneous (Fig. 4.4B, middle panel), with some regions showing a particularly high reaction density γ. Certain tubule segments are more likely to serve as the reaction site, due to their enhanced connectivity to the rest of the network. The normalized reaction density correlates with the inverse of the GMFPT (Fig. 4.4C), indicating that these highly reactive regions are in fact easier to find by diffusing particles.

These simulations imply that heterogeneity in ER structure and accessibility is expected to result in diffusive particle reactions becoming concentrated within certain regions. For comparison, we repeat the simulations on two synthetic network structures: a homogeneous honeycomb network (Fig. 4.4B, left panel) and a highly heterogeneous modified Mikado network [178] (Fig. 4.4B, right panel; see Methods for details). Both of these networks have the same spatial extent and total network length as the extracted ER networks. This allows for a quantitative comparison of the reaction density and reaction time distributions between all three families of networks.

As expected, reaction locations are more uniformly distributed on the honeycomb network. Within this homogeneous network, reactions are slightly more likely to occur at junction nodes rather than along the edges, in keeping with past work showing random walkers are more likely

to encounter each other at higher-degree network nodes [181]. There is also a dearth of reactions at the network boundary, mirroring the increased GMFPT in the boundary region (Fig. 4.1C). The ER networks show a similar drop-off in reaction density along edges as compared to junctions, as well as at the boundary. Moreover, due to the heterogeneous network density and connectivity, reactions are more concentrated into certain junctions within the network, with a higher maximum reaction density at these select junctions than is observed in the more uniform honeycomb. Reactions are further concentrated in the modified Mikado networks, demonstrating that more heterogeneous networks exhibit a broader range of reaction densities. This effect is quantified in Fig. 4.4D, where a longer tail is visible in the distribution of normalized reaction densities for ER and Mikado networks, as compared to the honeycomb. The morphology and connectivity of a network can thus tune the spatial distribution of reaction locations.

Network structure is not only responsible for shaping the spatial profile of reaction density, but can also affect the overall reaction time [45, 55]. The distribution of pair-wise reaction times on each network exhibits exponential scaling (Fig. 4.4E), as for a Poisson process with a single dominant time-scale. As noted in previous work, the mean reaction time on the ER (dashed purple line) is less than half of the target-averaged GMFPT (purple arrow) [67]. Even though there are higher spatial reaction densities in the more heterogeneous networks, mean reaction time is lowest in the homogeneous honeycombs and highest in the modified Mikado networks (Fig. 4.4E). Thus, there is a trade-off between locally concentrating reactions in space versus minimizing overall reaction time.

4.4.5 Proximity to well-connected perinuclear ER enhances accessibility

In addition to variations in local connectivity, a further source of heterogeneity for the peripheral ER network arises from the presence of extended sheet-like structures in the perinuclear zone (Fig. 4.5A). While the morphology of the perinuclear region cannot be well resolved with confocal microscopy, electron microscopy studies have shown that the ER near the cell nucleus consists of stacks of sheet-like structures, connected with spiral ramps [157].

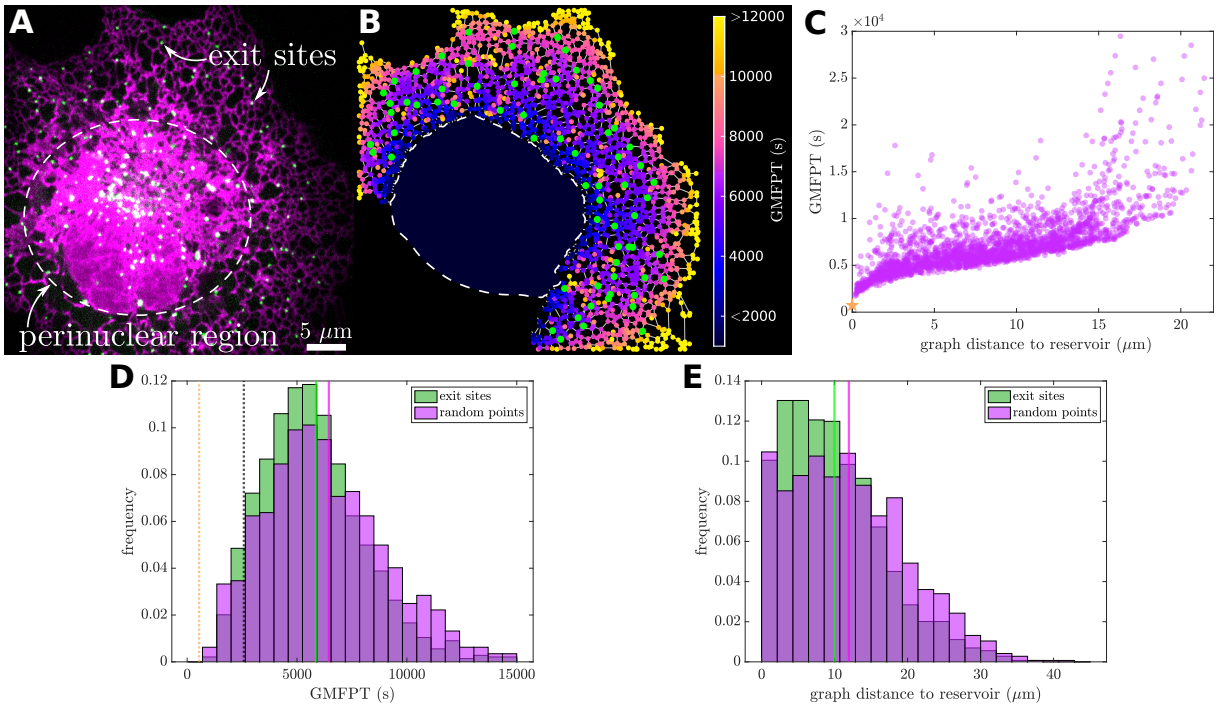

Figure 4.5. Concentration of ERES in regions of the peripheral ER with high search rate. (A) Image of the ER (magenta, mCherry_KDEL) and ERES (green, GFP_Sec24d) of a COS7 cell. (B) Extracted network structure of peripheral ER (excluding nucleus and perinuclear sheet regions). Junctions are colored by their effective search time (GMFPT, units of s). ERES positions are shown in green. Dashed line indicates excised nucleus and perinuclear sheet region, with interior color corresponding to GMFPT to a target at the center. (C) The GMFPT scales with graph distance to the perinuclear reservoir, for the example network shown in B. Orange star indicates GMFPT to target in reservoir. (D) ERES positions exhibit lower search times than random points on the network. Distributions include 1443 exit sites and the same number of random points extracted from the peripheral ER of 22 different COS7 cells. Green and magenta vertical lines indicate mean of each distribution; orange dotted line indicates the mean GMFPT (averaged over all networks) to a target in the reservoir center; black dotted line gives mean GMFPT to full population of peripheral and perinuclear ERES targets. (E) Distributions of graph distance to the reservoir for 1443 exit sites and 1443 random points extracted from the peripheral ER of 22 different COS7 cells.

We consider how the presence of a large perinuclear ER reservoir may affect search times for targets in the peripheral network. For simplicity, we do not directly model the structure of the perinuclear ER, but rather treat it as a large, flat, disk-like region connected along its boundary to the peripheral network. This approximation neglects transport between the stacked ER sheets themselves, which has previously been shown to be accelerated by spiral connecting ramps [162].

We expand our model to treat the perinuclear reservoir as an extremely large node, connected to many network tubules. We then compute the GMFPT to each peripheral node, assuming that particles can start anywhere in the peripheral network or the perinuclear region, in proportion to the available surface area. Within the perinuclear zone, particles effectively move through two-dimensional diffusion, returning to the peripheral network through narrow exits into individual tubules, as described in Supplemental Material Section S2. Due to the large area of the perinuclear zone, most particles enter this region before finding any given target on the peripheral network. As a result, targets located near the perinuclear region have lower GMFPTs. This effect leads to a gradient of accessibility for the peripheral ER as a function of distance from the perinuclear zone (Fig. 4.5B,C). A target placed in the center of the perinuclear zone has a search time comparable with the lowest values for the peripheral network.

Given the variation in search times for different regions of the peripheral ER, we next sought to examine whether certain ER-associated protein assemblies may be more likely to localize to more accessible regions. Specifically, we explore the distribution of ER exit sites (ERES), which serve as the export hubs for newly synthesized proteins in the ER [12, 13]. The mechanism underlying the distribution of exit sites on the network is not well understood, although prior work has suggested they may arise from a process of confined diffusive aggregation [182]. The ERES are found both on the perinuclear and the peripheral ER (Fig. 4.5A). Because puncta in the well-mixed perinuclear region are expected to all have similar accessibilities, we focus here on those ERES located in the peripheral network.

We extract ERES puncta locations using several different markers for the exit sites (Fig. 4.5A, details in Methods) and project the peripheral ERES locations onto the extracted ER network structure (Fig. 4.5B). We next calculate the GMFPT to each peripheral ERES position, and compare the distribution of these times to that expected for randomly selected locations along the networks (Fig. 4.5D). The distribution of search times at the exit sites (mean $\pm$ std: $5.9 \pm 2.8 \times 10^3$s) is shifted to smaller values as compared to the randomized control (mean $\pm$ std: $6.5 \pm 3.1 \times 10^3$s). Although the magnitude of the shift is modest, this difference is statistically

significant [$p << 10^{-6}$ by a one-sided student's t-test] due to the large number of ERES puncta sampled. The ERES are thus disproportionately likely to be found in more accessible regions of the peripheral network. The lower search times to peripheral ERES locations can be explained by their tendency to be located near the perinuclear zone and their depletion from the distal regions of the periphery (Fig. 4.5E). Exit sites located in the perinuclear zone itself (approximated as targets in the center of the reservoir) are expected to have the lowest search times (Fig. 4.5D, dotted orange line). Because a substantial fraction of ERES are found in the perinuclear zone, the overall average search time to the exit sites (black dotted line) is approximately two-fold lower than the search time to randomly selected peripheral targets. Overall, localization of ERES to within and nearby the perinuclear region is expected to enhance their accessibility for diffusively searching particles.

These results indicate a potential structure-function relationship for the peripheral ER network. Structural heterogeneity in the network, both in terms of connectivity and in terms to proximity to the perinuclear ER, translates to heterogeneous search times for diffusing particles. In turn, certain multi-protein assemblies within the ER network appear to be localized to the more accessible regions, where they can be more easily reached by other diffusive particles.

4.5 Conclusion

In this work, we highlight the heterogeneous connectivity of the tubular ER network and its consequences for diffusive particle transport. We extract peripheral ER network structures from live-cell confocal images of COS7 cells and analytically compute mean first passage times (MFPTs) for particles diffusing over these networks. These calculations allow us to quantify the variability in diffusive accessibility within individual ER architectures. The global MFPT (GMFPT) to individual nodes within the network is found to vary by up to 4-fold due to the heterogeneous connectivity of the network.

We then directly visualize the local spreading of ER membrane proteins from an initial

region of pulsed photoactivation. Signal arrival rates to distinct regions equidistant from the photoactivated center show marked disparities (varying by more than a factor of 4 within a single cell). We compare these measurements to simulations of diffusing particles on the visualized ER network structure, and show that the simulated rates of arrival to distinct regions show strong agreement with experimental data. These results demonstrate the importance of network structure in guiding the observed heterogeneity in protein spread.

By modifying and extending a model for 'minimal networks' driven by membrane tension and new tubule growth [39], we assess the effect of ER network rearrangements on protein spread. The substantial separation of timescales between network dynamics and protein diffusivity leads to only a marginal predicted effect of tubule rearrangement on the motion of proteins within the ER.

Additionally, we simulate pairs of reactive particles diffusing through the ER and demonstrate that the structural heterogeneity of the network gives rise to effective hot-spots where encounters are more likely to occur. The proximity of targets to the well-connected perinuclear zone provides another source of variable accessibility with the network. Notably, an analysis of ERES positions across the peripheral ER indicates that the location of these structures is biased towards the more accessible regions near the perinuclear zone and away from the less accessible distal periphery of the cell.

We note that the ER models in this study are intentionally highly simplified, reducing the complex membrane-enclosed geometry of the ER to a network of effectively one-dimensional tubules. These simplifications make it possible to focus on the role of cellular-scale network connectivity and rearrangements in particle transport. The simple structural model is sufficient to reproduce the observed heterogeneous protein arrival rates to different network regions in photoactivation experiments. More detailed structural models could include variability in tubule diameter [26, 21] as well as scattered peripheral sheets [20], which may themselves be perforated with holes [155] or composed of dense tubular matrices [80]. Exploring the effect of these structures on particle transport forms a potentially interesting avenue for future work.

The network dynamics model employed here aims to isolate the key important features governing ER rearrangements – namely, the formation of new tubules and the tension-driven movement of junctions [9, 183, 39]. Although network dynamics are shown to have little impact on protein diffusion, they are expected to play a greater role in the motion of larger and slower-moving ER-associated bodies such as the ERES [37]. Furthermore, it is possible that directed flows of luminal and / or membrane contents may be associated with the growth and shrinking of ER tubules, as implied by recent evidence that new tubule growth is followed by a delayed widening and infilling with Climp63 spacer proteins [21]. Although the spatial extent and magnitude of such flows is not currently established, they could more extensively contribute to modulating intra-ER protein motion.

The transport, quality control, and export of proteins in the ER are essential biological processes in the early secretory pathway. These processes require a variety of encounters between newly manufactured proteins, chaperones, and regulatory factors. The structural heterogeneity of the ER network implies that certain regions may allow for more efficient encounters between binding partners. Notably, however, the effect of morphology becomes important only in the regime of diffusion-limited kinetics when the particles are sparsely scattered over the network [55]. The sequestration of some quality control machinery to specific regions of the ER [170] implies that long-range diffusive search by proteins through the network may be an important factor in the kinetics of such pathways.

In addition to protein transport, the results described here apply to any diffusive particles contained in the membrane or lumen of the peripheral ER network. This includes ions such as calcium, as well as the buffer proteins which bind to them. In particular, we would expect the demonstrated structural heterogeneity of the ER to lead to more rapid calcium release in better-connected regions of the network. Given that calcium homeostasis and signaling is one of the key functional roles of the ER, heterogeneous transport could thus provide an important link between physical structure and biological function. Furthermore, it would be interesting to explore whether contacts between the peripheral ER and other cellular structures, such as

mitochondria, tend to preferentially occur at highly connected regions, which may facilitate the delivery of lipids or ions across these contacts [184, 88, 185].

Through the use of experiments paired with quantitative image analysis and computational modeling, our results demonstrate how morphology guides particle transport and reactions in the ER, with broad implications for diffusive transport in any intracellular network structure.

4.6 Acknowledgements

Chapter 4, in full, is a reprint of the material with minor edits as it appears in Zubenelgenubi C. Scott, Katherine Koning, Molly Vanderwerp, Lorna Cohen, Laura M. Westrate, and Elena F. Koslover. "Endoplasmic reticulum network heterogeneity guides diffusive transport and kinetics." Biophysical Journal 122, no. 15 (2023): 3191-3205.

Appendix A

Appendix for Chapter 2

A.1 Liquid networks in 3D

Here we briefly explore the extension of our liquid network model to three-dimensional (3D) systems. It should be noted that the peripheral ER in adherent COS7 cells is effectively a 2D network [80]; however, near the nucleus in adherent cells [80, 186, 187], and in the cell body of neuronal cells [188, 189], it can form a 3D networked structure.

A liquid network embedded in a 3D space has fundamentally different properties from the planar case. Specifically, it becomes necessary to consider a distinct length scale (r) – the effective contact distance within which a growing tip can fuse into the existing network structure. This distance is expected to be at least 0.1 μm, given the approximate 0.05 μm radius of COS7 ER tubules [92]. However, we may expect the contact distance to be substantially larger due to fluctuations, such as the thermal fluctuations of the tubules themselves (which have a typical persistence length of 8 μm [70]). Furthermore, ER tubules tend to be associated with the microtubule cytoskeleton [38, 190, 27, 28, 29], and growing tubules often hitchhike on other motor-driven organelles [191, 30, 31, 32], which may affect the fluctuations of both the nascent and existing tubules. Here, we assume contact distances that range between $0.1 - 0.25$ μm, comparable to expected sizes of vesicular organelles swinging around microtubules.

We carry out simulations of 3D networks that are analogous to our 2D model (see Materials and Methods), with a few concrete changes. Specifically, we treat all tubules as

spherocylinders, neglecting steric interactions, and allowing fusions to occur when the tip of a growing tubule comes within distance r of an existing edge. The direction of new tubule spawning is uniformly sampled from the set of directions perpendicular to the spawning edge.

All simulations take place in a sphere of radius $R_{\text{sim}} = 10$ μm. Growing nodes which reach R_{sim} cease their growth and become boundary nodes. These boundary nodes obey the same Langevin equation as other nodes, but their motion is restricted to sliding along the spherical boundary. If two boundary nodes come within the threshold distance (dx, just as in 2D) of one other and they share a neighbor, they annihilate and their common neighbor assumes their average position on the boundary. This allows for an analog of T1 rearrangements and loop closures at the boundary.

Figure A.1. Liquid network model produces stable structures in three dimensions, with steady state geometries obeying different scaling laws than in two dimensions. (A) Example snapshot of a liquid network simulation within a sphere of radius 10 μm, with tubule contact distance $r = 0.25$ μm, and $\ell = 6.3$ μm. (B) Network length over time for four simulations with different fundamental length and time scales, $\ell = \sqrt{b/k}$ and $\tau = 1/\sqrt{bk}$, and $r = 0.25$ μm. The steady-state network length is dependent on ℓ while the time required to reach steady state is set by τ. (C) Average edge length scales linearly with $\sqrt{b/k}$ for several tubule contact radii. Results from 2D networks shown in yellow for comparison; dashed black line shows $\lambda \sim \ell$ scaling. (D) Distributions of mesh sizes ξ in 2D and 3D liquid networks. Black line indicates fit to Rayleigh distribution with scale parameter $\sigma = 0.80$. (E) Mesh size $\bar{\xi}$ varies with length scale ℓ; dashed black lines indicate $\bar{\xi} \sim \ell^{3/4}$ scaling. (F) Mesh size scaling with contact distance; colors are different values of ℓ; dashed black line indicates $\bar{\xi} \sim r^{1/2}$. (G) Total network length L as a function of length scale $\ell = \sqrt{b/k}$ for several contact distances r. Dashed black line indicates ℓ^{-1} scaling for 2D networks (yellow); solid black lines indicate $\ell^{-1.5}$ scaling for 3D networks. (H) Total network length L scales inversely with tubule contact distance r, across a range of length scales ℓ (colors). Dashed black line indicates $L \sim r^{-1}$ scaling.

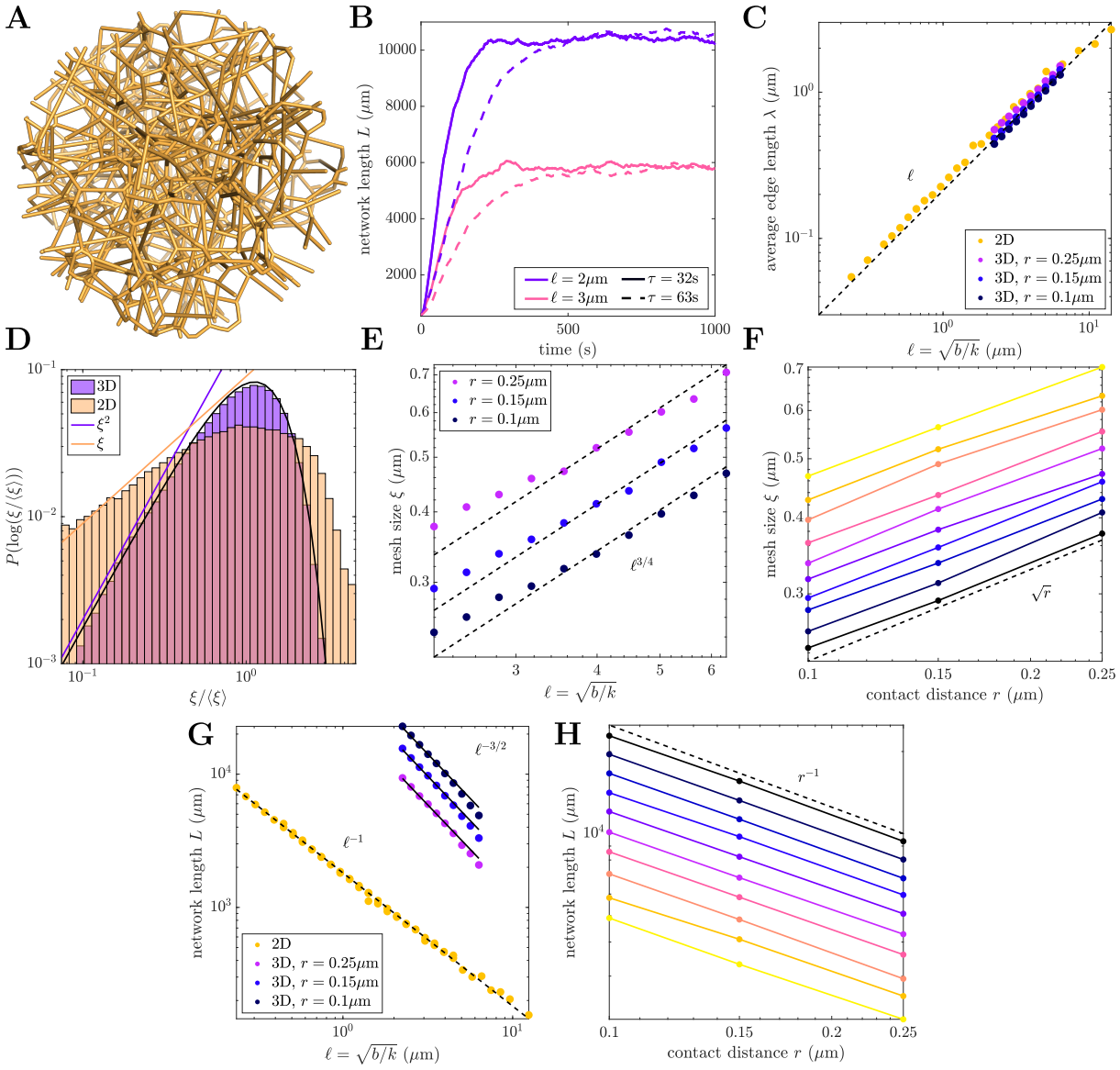
A
B
network length L (μm)
time (s)
$\ell = 2\mu$m
$\ell = 3\mu$m
$\tau = 32$s
$\tau = 63$s
C
average edge length λ (μm)
$\ell = \sqrt{b/k}$ (μm)
2D
3D, $r = 0.25\mu$m
3D, $r = 0.15\mu$m
3D, $r = 0.1\mu$m
D
$P(\log(\xi/\langle\xi\rangle))$
$\xi/\langle\xi\rangle$
3D
2D
ξ^2
ξ
E
mesh size ξ (μm)
$\ell = \sqrt{b/k}$
$\ell^{3/4}$
F
mesh size ξ (μm)
contact distance r (μm)
$\sqrt{r}$
G
network length L (μm)
$\ell = \sqrt{b/k}$ (μm)
$\ell^{-3/2}$
ℓ^{-1}
H
network length L (μm)
contact distance r (μm)
r^{-1}

These simulations generate network structures (Fig. A.1A, Video S2.6) that also reach a steady-state (Fig. A.1B) whose density varies as a function of the balance between growth (k) and tension-driven relaxation (b). Given the introduction of a new length scale (r) for 3D networks, the scaling laws governing the steady-state geometry may be expected to differ from the 2D case. In particular, we look at the scaling of the average edge length λ versus the fundamental length scale $\ell = \sqrt{b/k}$. If we assume that the typical length that a new tubule must grow before fusing into the network scales in proportion to the average edge length λ, then in analogy to Eq. 2, we have the relationship:

$$\frac{dL}{dt} = \zeta k L \lambda - \gamma b n = 0 \tag{A.1}$$

at steady-state. Neglecting numerical prefactors ζ, γ, and noting that the number of nodes scales as $n \sim L/\lambda$ gives the same predicted scaling relationship as in the 2D case: $\lambda \sim \ell$. Notably, if the average edge length is approximately independent of the total size of the domain, then dimensional analysis implies that it should not depend on any other length scale. Specifically, changing the contact distance r should have little effect on the average edge length. These predictions for the average edge length are borne out in our simulations (Fig. A.1C).

We next consider the mesh size of the network, analogous to the polygon size in the 2D case. Mesh size is determined by scattering random points ($N = 20000$) in the simulation volume and calculating the minimal distance from each point to the network [192]. The resulting distribution of mesh sizes is shown in Fig. A.1D. For the 2D case, the small-size tail of the distribution scales according to $P(\log \xi) \sim \xi$, as expected from Fig. 3A, given that $\xi \sim \sqrt{A}$. Interestingly, the 3D networks exhibit a distinctly different scaling for this small-size tail, with $P(\log \xi) \sim \xi^2$. The mesh size distribution for the 3D liquid networks is similar to the Rayleigh distribution observed in experimental studies on collagen and fibrin networks [192]. Notably, this distribution is also expected for 'Mikado' networks consisting of long, randomly distributed, disconnected lines of length much greater than the pores size [192].

The overall mesh size $\bar{\xi}$ for the network is defined as the average of this distribution. For a lattice-like network, the average mesh size is expected to scale with the average edge length, $\bar{\xi} \sim \lambda$. In an entangled, semi-flexible polymer network, there is an alternate scaling of $\bar{\xi} \sim \sqrt{\lambda r}$ [193]. In 3D liquid networks with a range of tubule contact distances, we find $\bar{\xi} \sim \ell^{3/4}$, falling between these two regimes (Fig. A.1E). We also find $\bar{\xi} \sim \sqrt{r}$, matching the scaling expected for entangled, semi-flexible polymer networks (Fig. A.1F) [193].

Putting these results together provides an estimate for how the total edge length L in the liquid network scales with the parameters. Namely, we would expect

$$L \sim \frac{R^3}{\bar{\xi}^2} \sim \ell^{-3/2} r^{-1}, \tag{A.2}$$

which agrees with simulations in a fixed-size domain of radius $R = 10$ μm (Fig. A.1G,H). In summary, increasing tubule radius has little effect on average edge length, but results in a spatially sparser network with larger pore size and less total edge length. Increasing $\ell = \sqrt{b/k}$ also leads to a sparser network, with a steeper scaling than in two dimensions.

More detailed exploration of 3D liquid network structure would require incorporation of explicit fluctuations in the ER tubules, which would be expected to increase the effective contact radius for fusion, possibly in a length-dependent manner. Furthermore, additional experimental characterization of 3D ER network structures is needed to establish typical pore sizes and edge lengths *in vitro*.

A.2 Steady state network properties are independent of junction diffusivity and minimal length scale

In this section, we demonstrate that changes to junction diffusivity and the minimal length scale for junction rearrangements have no effect on steady state network properties, within a wide range around our chosen values.

Our choice for junction diffusivity (typically 10^{-5} μm ^{2}/s) is sufficiently small to have

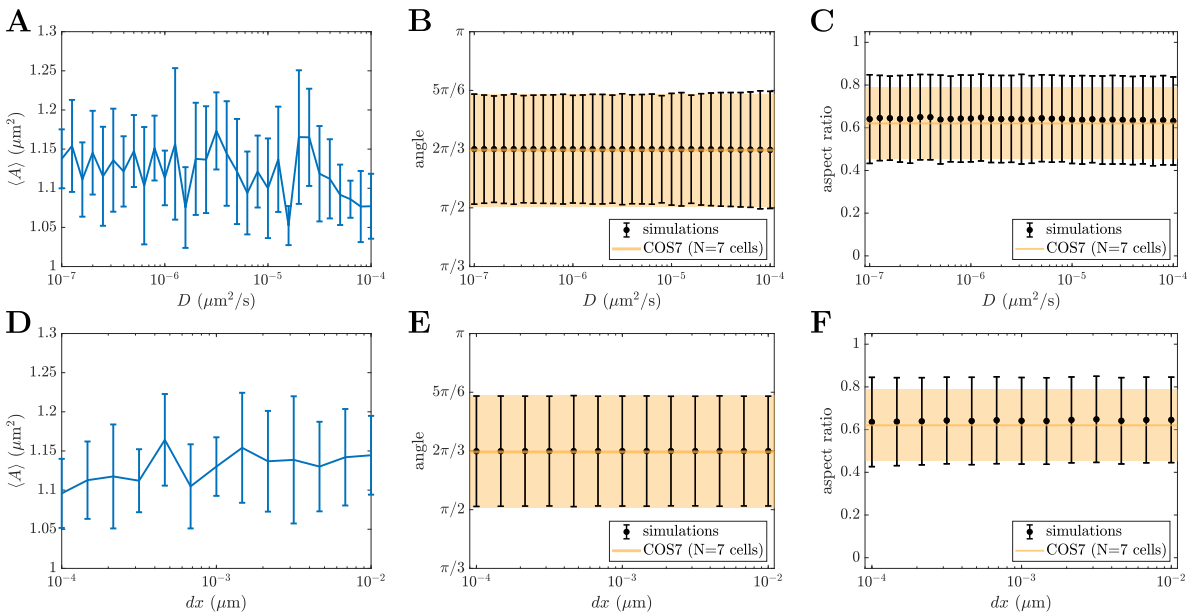

Figure A.2. Junction diffusivity and minimal length parameter do not affect liquid network properties. (A) Diffusivity of junctions is sufficiently small to have no effect on mean polygon area. Diffusivity has no effect on the mean and standard deviation of angles at three-way junctions (B) or the aspect ratio of polygons (C). Minimal length parameter dx does not substantially impact mean area of polygons (D), angles at three-way junctions (E), or the aspect ratio of polygons (F). All simulations performed with $b = 0.02$ μm/s, $k = 0.005$ μm $^{-1}$s^{-1}, and for (D)-(F), $D = 10^{-5}$ μm ^{2}/s.

no effect on polygon areas (Fig. A.2A). Additionally, the mean and standard deviation of the distributions of angles at three way junctions and polygon aspect ratios are unaffected by junction diffusivity (Fig. A.2B,C). The noise in these metrics instead arises from the random growth of new tubules and the tension-driven sliding of junctions.

In our simulations, $dx = \max(\sqrt{D \cdot dt}, b \cdot dt)$, sets the minimal length scale. When neighboring junctions are within this distance of one another, they check for possible rearrangements that would minimize the total connected edgelength. Steady state network properties, such as polygon area, junction angle and polygon aspect ratio, are insensitive to changes in dx for otherwise fixed simulation parameters (Fig. A.2D-F).

A.3 Polygon growth dynamics: regular n-gons

Informed by the equation of motion for junctions in a liquid network (Eq. 1), an approximate form for the growth law can be derived. For simplicity, we consider the growth dynamics of regular n-gons, whose outgoing connections are assumed to bisect the angle of each junction. The rate of change in area A is given by:

$$\frac{dA}{dt} = \sum_{i=1}^{n} \frac{\partial A}{\partial \vec{r}_i} \cdot \frac{d\vec{r}_i}{dt} = n \frac{\partial A}{\partial \vec{r}_1} \cdot \frac{d\vec{r}_1}{dt} = n \left(\frac{\partial A}{\partial r_u} \right) \left(\frac{dr_u}{dt} \right). \tag{A.3}$$

where $\vec{r}_i$ are the positions of each of the polygon's n identical junctions, and r_u is the component along the radial direction.

Assuming diffusion is negligible, the junction motion is determined solely by the length minimization term from Eq. 1, giving

$$\begin{aligned} \frac{dr_u}{dt} &= -b \frac{\partial f}{\partial r_u} = -b \left(2 \sin \frac{\pi}{n} - 1 \right) \\ \frac{dA}{dt} &= b \lambda n \left(\cos \frac{\pi}{n} \right) \left(1 - 2 \sin \frac{\pi}{n} \right), \end{aligned} \tag{A.4}$$

where λ is the side length of the polygon.

This predicts a negative growth rate for $3 < n < 6$ and a positive growth rate for $n > 6$. For small polygons, we would expect $n \approx 3$, and the shrinking rate should scale with the polygon perimeter ($\lambda n \sim \sqrt{A}$). For large polygons, the rate of growth can be described as $\frac{dA}{dt} \sim \sqrt{A} \xi(A)$ where $\xi(A)$ grows with the number of polygon sides. Because the number of sides is expected to grow with area, $\xi(A)$ should increase with A. We therefore make the approximation that large polygon growth rates increase as A^{β} for some approximate value of $0.5 < \beta < 1$. Overall, we take an ansatz that linearly combines the two scaling relations for small and large area polygons:

$$\frac{dA}{dt} = \hat{g} A^{\beta} - \hat{h} \sqrt{A}, \tag{A.5}$$

where normalization by the average area yields Eq. 4 in the main text. It should be noted that this analysis does not account for the irregular shape of the polygons in the liquid network and thus provides only an approximation for the growth rate as a function of area.

A.4 Derivation of the polygon area distribution from growth and splitting laws

The goal here is to determine the steady-state distribution of polygon areas in a liquid network, $P(A)$, starting from the laws for growth and splitting of individual polygons and the assumption that polygons on average take the form of a hexagon. The growth law extracted from simulations (Fig. 2.4 and the splitting rate of these polygons can be expressed as follows:

$$\frac{1}{\tau}\frac{dA}{dt} = g\langle A\rangle^{1-\beta}A^{\beta} - h\sqrt{\langle A\rangle}\sqrt{A}, \tag{A.6a}$$

$$k_{\text{split}} = \hat{k}\sqrt{A}, \tag{A.6b}$$

where A is polygon area, $\langle A\rangle$ is the average area of all polygons, g, h, and β are constants determined from a fit of simulated growth rates, and $\hat{k} = (\sqrt{2\sqrt{3}})k$ is the prefactor for splitting in terms of the spawning rate k. Equation A.6b is obtained by finding the perimeter p of a regular hexagon of area A and noting that the expected splitting rate is $k_{\text{split}} = \frac{1}{2}kp$, since new tubules can grow in either direction perpendicular to an edge.

If we make the additional assumption that polygons tend to split in half upon new tubule growth, the distribution of polygon areas, $P(A)$, would be expected to obey an effective Fokker-Planck equation:

$$\frac{\partial P}{\partial t} = -\frac{\partial}{\partial A}\left[\frac{dA}{dt}P(A)\right] - \hat{k}\sqrt{A}P(A) + 4\hat{k}\sqrt{2A}P(2A). \tag{A.7}$$

Here, the first term corresponds to the area drift associated with polygon growth and shrinking, the second term describes polygon disappearance due to splitting, and the last term corresponds

to the formation of new polygons after a splitting event [194]. We note that stochastic noise terms are neglected in this equation for simplicity. While such noise could be extracted from the breadth of the growth rate distribution in polygons of each size (Fig.4E), we choose to consider only the deterministic drift in polygon areas that shrink or grow in a size-dependent manner as the simplest possible description accounting for the observed steady-state area distribution.

A.4.1 Small area scaling

Although Eq. A.7 is not easily solvable analytically, we can analyze its behavior in the limit of very small polygons. We consider a narrow band of small polygon areas: $(0, \delta A)$. The rate at which polygons disappear from this band due to shrinking below 0 area (J_0) must equal the total rate at which polygons enter the band. This includes the shrinking of larger polygons, which enter the band at rate $v(\delta A)P(\delta A)$ and the creation of new polygons due to splitting of polygons with area between $(0, 2\delta A)$:

$$J_0 = -v(\delta A)P(\delta A) + 2\hat{k}\int_0^{2\delta A}\sqrt{a}P(a)da - \hat{k}\int_0^{\delta A}\sqrt{a}P(a)da \tag{A.8}$$

Here, the second term corresponds to 2 new polygons created by splitting and the last term accounts for the fact that the original polygon vanishes when a splitting event occurs. If we assume that the distribution function for small areas is a power law: $P(A) = A^{\mu}$, then the above equation can be expressed as:

$$J_0 = \hat{h}(\delta A)^{\mu+1/2} + \hat{k}\left(\frac{2^{\mu+5/2}-1}{\mu+\frac{3}{2}}\right)(\delta A)^{\mu+3/2} \tag{A.9}$$

When very small areas are being considered ($\delta A \to 0$), the first term is dominant, so we have $J_0 \to \hat{h}(\delta A)^{\mu+1/2}$. In order to have a finite flux of disappearing polygons, countering the production of new polygons throughout the system, we must set $\mu = -1/2$.

Therefore the distribution function for polygons of small area can be written as

$$P(A) = \frac{c_1}{\sqrt{A}} \text{ for small A,} \tag{A.10}$$

with c_1 a constant. Converting to a logarithmic distribution, $P(\log(A)) = AP(A) \sim \sqrt{A}$. This square root scaling matches the distribution of small polygon areas measured for simulations of liquid networks (Fig. 2.3A and Fig. 2.4H).

A.4.2 Large area scaling

For very large values of the area A, the polygon dynamics are described by a balance between growth and splitting. We neglect the last term in Eq. A.7, assuming that $P(2A) \ll P(A)$ so that the production of very large polygons by splitting events is rare. This assumption is self-consistent with an exponentially decaying distribution for large areas. Plugging the growth velocity from Eq. A.6a into the truncated form of Eq. A.7 gives the steady-state distribution of polygon areas as:

$$P(A) = c_3 c_1 A^{-\beta} e^{-c_2 A^z} \text{ for large A,} \tag{A.11}$$

where $c_2 = \frac{\hat{k}}{gz}\langle A \rangle^{\beta-1}$, $z = \frac{3}{2} - \beta$, and c_3, c_1 constants.

A.4.3 Full distribution by stitching together the two limits

In order to construct the complete distribution, the two limits for small and large area are married together at some intermediate area A^*. Enforcing continuity of the distribution requires $c_3 = A^{*(1-z)} e^{c_2 A^{*z}}$ and gives the following functional form for the full distribution:

$$P(A) = \begin{cases} \frac{c_1}{\sqrt{A}} & \text{for } A < A^* \\ \frac{c_3 c_1}{A^\beta} e^{-c_2 A^z} & \text{for } A \geq A^* \end{cases} \tag{A.12}$$

The remaining unknowns are c_1, A^*, and $\langle A \rangle$ (which also appears in c_2). In order to estimate A^* and $\langle A \rangle$, we first note that the total number of polygons must remain fixed at steady state. Thus, the flux of vanishing small polygons must equal the flux of newly created polygons via splitting: $J_0 = J_{\text{split}}$. The flux of vanishing polygons is:

$$J_0 \approx c_1 h \sqrt{\langle A \rangle} / \tau, \tag{A.13}$$

and the flux of newly created polygons due to splitting is:

$$\begin{aligned} J_{\text{split}} &= \int_0^\infty \hat{k} \sqrt{A} P(A) dA \\ &= \int_0^{A^*} \hat{k} c_1 dA + \int_{A^*}^\infty \hat{k} c_3 c_1 A^{\frac{1}{2}-\beta} e^{-c_2 A^z} dA \\ &= \hat{k} c_1 A^* \left(1 + \frac{1}{c_2 z} (A^*)^{-z} \right) \end{aligned} \tag{A.14}$$

Additionally, an expression for the average area is obtained via $\langle A \rangle = \int_0^\infty P(A) A dA / \int_0^\infty P(A) dA$. Through this matching of fluxes and the definition of average area, we obtain two equations:

$$\begin{aligned} h \sqrt{\langle A \rangle} / \tau &= \hat{k} A^* \left(1 + \frac{1}{c_2 z} (A^*)^{-z} \right), \\ \langle A \rangle &= \frac{\frac{2}{3} A^{*3/2} + \frac{c_3}{z c_2^{1+1/(2z)}} \Gamma\left(1 + \frac{1}{2z}, c_2 A^{*z}\right)}{2\sqrt{A^*} + \frac{c_3}{z c_2^{1-1/(2z)}} \Gamma\left(1 - \frac{1}{2z}, c_2 A^{*z}\right)}, \end{aligned} \tag{A.15}$$

where Γ is the incomplete Gamma function. These can be solved numerically for A^* and $\langle A \rangle$ using parameters g, h, and β from the effective growth law. Finally, the prefactor c_1 is set by normalizing the full distribution $\int_0^\infty P(A) dA = 1$.

Using the non-dimensionalized growth law extracted from liquid network simulations (Fig. 2.4E, Eq. 4), this gives $A^* \approx 0.12\ell^2$ and $\langle A \rangle \approx 0.23\ell^2$. We note that the predicted average area is similar to the actual value of $\langle A \rangle \approx 0.29\ell^2$ obtained for simulated liquid networks (Fig. 2.2D).

The area A^* corresponds to the peak in the area distribution function $P(A)$ (see Fig. 2.4H) and thus gives an estimate of the most 'typical' polygon area. For COS7 ER, we have the length scale $\ell \approx 1.95$ µm, giving the predicted typical area $A^* \approx 0.46$ µm ^{2} in the liquid network model. For comparison, the peak in the measured area distribution for ER polygons in COS7 cells is 0.72 ± 0.32 µm ^{2} (mean and standard deviation across cells).

A.5 Polygon neighbor counts, areas and growth rates

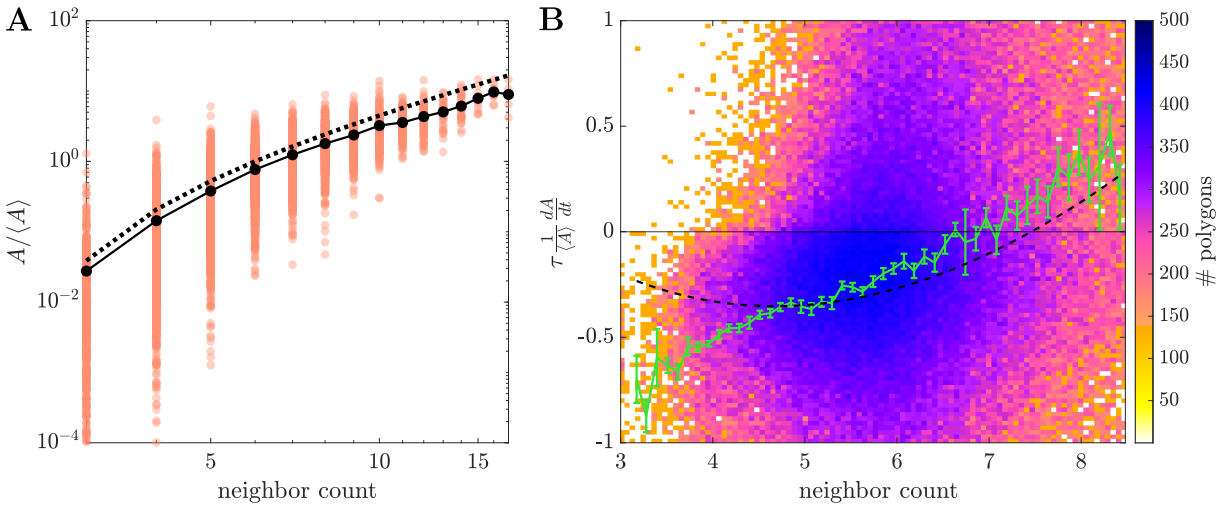

Figure A.3. Polygon area, neighbor count and growth rate are interconnected. (A) Polygon area as a function of neighbor count (same simulation data as in Fig. 4.) Solid black line gives mean area at each n, dotted black line is analytic prediction from Eq. A.16. (B) Non-dimensionalized growth rates normalized by mean area and network timescale for 10 liquid network simulations. Green curve indicates mean (and standard error of the mean) within coarse bins of normalized neighbor count. Non-integer neighbor counts arise from averaging over 3 s intervals. Dashed black line is obtained by plugging Eq. A.16 into Eq. 4, and using the fit parameters extracted from the growth rate vs area data (Fig. 4E).

In this section, we derive an approximate geometric relationship between a polygon's normalized area and its number of neighbors, and quantify the relationship between growth rates and number of neighbors. To begin, we make the simplifying assumption of regular polygons, and compute the number of average-sized neighbor polygons that can be placed around a polygon of a given area. Specifically, we imagine a regular polygon with n sides, with outgoing connections bisecting its junction angles, surrounded by neighboring regular polygons with m sides. Note

that m may not always be an integer, but it still provides an estimate for the expected relationship between side counts of the central and neighboring polygons. The internal angles of the neighbor polygons are given by $\theta = \pi\left(1-\frac{2}{m}\right)$, which must be equated to half the external angle of the central polygon: $\theta = \frac{\pi}{n} + \frac{\pi}{2}$. This gives the relationship $m = \frac{4}{1-2/n}$.

The area of a regular polygon with side length ℓ can be expressed $A = n\ell^2/\left(4\tan\frac{\pi}{n}\right)$. Assuming that all neighbor polygons are average sized, with area $\langle A\rangle$, the normalized area of the central polygon can be expressed as:

$$\frac{A}{\langle A\rangle} = \frac{n\tan\frac{\pi}{m}}{m\tan\frac{\pi}{n}} = \left(\frac{n-2}{4}\right)\left(\frac{\tan\frac{\pi(1-2/n)}{4}}{\tan\frac{\pi}{n}}\right). \tag{A.16}$$

This predicted scaling for area as a function of neighbor (or edge) count approximately captures the scaling of polygons in liquid networks (Fig. A.3A). It should be noted that this derivation assumes regular polygons — for irregular polygons the area we be expected to be slightly lower, as seen in the simulation data.

Polygon growth rates and the number of neighbors are also intimately related. As in foams [72], regular polygons with more sides have a higher internal angle, translating to a net outward motion of junctions. We note that for liquid networks there is a large variation in the growth rate among polygons with the same number of neighbors (Fig. A.3B). On average, however, the growth rate tends to scale together with the number of neighbors, with polygons that have 7 or more sides tending to grow, while those with fewer sides tending to shrink. The discrepancy from the classic von Neumann law (which predicts a cross-over from growth to shrinking at precisely 6 sides) may be due to the more irregular shape of liquid network polygons, and their tendency to change neighbor counts continuously as they grow.

Using the liquid network simulations, we can also demonstrate the consistency of the above formula for area as a function of neighbor count and the fitted ansatz for polymer growth rates vs area. Plugging Eq. A.16 into Eq. 4, provides a predicted polygon growth rate as a function of edge count. Using the fit parameters from the main text for g, h, β and the values

from fitting normalized area as a function neighbor count to Eq. A.16 gives the dashed line in Fig. A.3B. The two quantifications (growth as a function of area or growth as a function of neighbor count) appear to be relatively consistent for polygons with many neighbors. We note that the underestimate when converting to growth rate versus neighbor count may be the result of plugging averages from a noisy distribution into a nonlinear function. Polygons with 4 or fewer neighbors have limited data and thus may not provide an accurate estimate of the shrinkage rate of small polygons. In the main text, we consider the dependence of polygon dynamics on the normalized area, both because of the tighter error bars and to allow for a direct derivation of the area distribution.

A.6 Boundary-free liquid networks

Here, we demonstrate that the boundary conditions employed in the main text have no effect on the steady-state properties of liquid networks. In particular, we show that liquid networks exhibit a well-defined steady-state density even in the absence of tethering to any static structures, including the outer boundary membrane.

To this end, we perform simulations of boundary-free liquid networks with a catastrophe rate of $\alpha = 0.25\ \mathrm{s}^{-1}$, which allows for finite growth lengths of outwardly growing tubules. These networks expand their spatial footprint over time, forming complex webs evocative of *in vitro* images of reconstituted ER in Xenopus extract, which also show decreasing densities and longer tubules towards the network periphery [107].

There is no global steady-state in this system; the outer boundary continues to expand indefinitely. However, the architecture in the bulk of the network does reach a steady state. Network properties, such as average polygon area, within a region at the center of the network stabilize over time, and scale as expected with the kinetic parameters (Fig. A.4C, Eq. 11).

This variant of the liquid network model demonstrates that the network is able to support tension and achieve a steady-state architecture without any connection to stationary structures.

The length-minimizing tension is counteracted by the finite mobility of network nodes and the network density is ultimately determined by the balance between this mobility (b) and the rate of new tubule spawning (k).

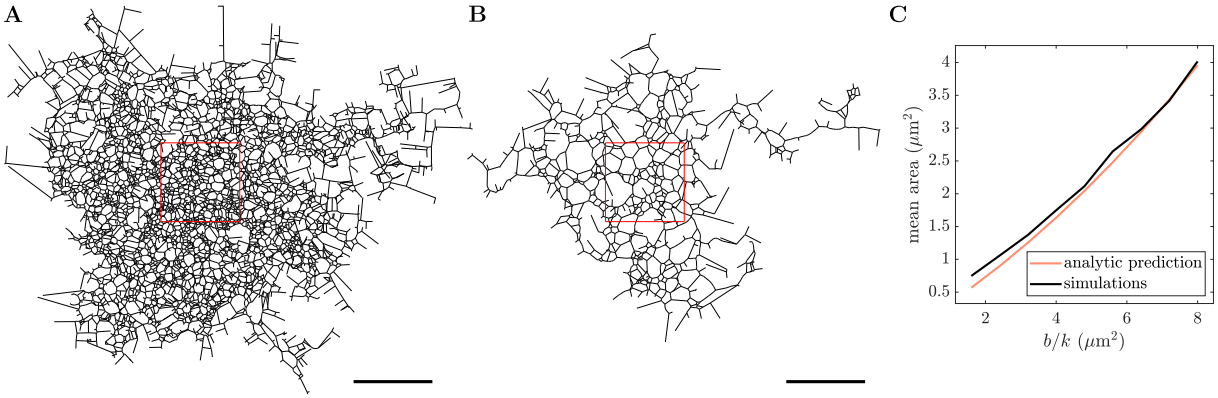

Figure A.4. Boundary-free liquid networks achieve steady state in the bulk. Example simulations after 1000s are shown with (A) low mobility, $b = 0.008$ μm/s and (B) high mobility, $b = 0.04$ μm/s. (C) Average polygon area calculated within central 20 μm $\times$ 20 μm region of boundary-free liquid networks, averaged across 10 simulations for each value of b/k. The orange curve indicates analytic prediction from Eq. 11 in the main text. In (A) and (B), scale bars and side lengths of red squares are 20 μm. Simulations performed with spawning rate $k = 0.005$ μm $^{-1}$s^{-1}, catastrophe rate $\alpha = 0.25$ s^{-1}, and over a range of mobilities $b = 0.004 - 0.04$ μm/s.

Appendix B

Appendix for Chapter 3

B.1 Code availability

Example Matlab code for carrying out the calculations described in this chapter (for both analytic calculations and simulations) is available at https://github.com/lenafabr/propagatormethods. The details of the network construction and simulation algorithms are outlined in the appendices below.

B.2 Generating network structures

B.2.1 Cellular network structures

Peripheral ER network structures were obtained from confocal imaging of live COS7 (monkey kidney) cells, labeled with KDEL venus as a fluorescent luminal marker. Cell culture and imaging was carried out exactly as described in prior work [45]. Images of nine individual cells were analyzed using Ilastik, an interactive machine-learning tool [110], to classify pixels as belonging to the ER network structure. The images were then segmented (with standard Otsu thresholding) and skeletonized using built-in algorithms in Matlab [195]. The network topology was extracted by grouping skeleton nodes in adjacent pictures and using Matlab's bwtraceboundary subroutine to trace out skeleton boundaries between groups of nodes.

Mitochondrial networks in yeast cells were taken directly from published data [55] available at https://data.mendeley.com/datasets/nshn8hhd6d/1.

B.2.2 Synthetic network structures

To create the synthetic peripheral ER networks featured in Fig. 3.5, we began with a regular honeycomb lattice, 30 lattice cells across, and excised an annular region. The inner and outer radii of the anulus were chosen to correspond with the dimensions of the nucleus (8μm) and the cell boundary (20μm) for a typical COS7 cell. The network edge length is 0.8μm, matching the average edge length ($0.78 \pm 0.02\mu$m, mean plus or minus standard error of the mean) computed for the extracted ER networks used in this study.

The synthetic networks from Figs. 3.6, 3.8, and 3.10 were also initiated as honeycomb lattice networks, 10 lattice cells across. The spatial positions of the nodes were then randomly perturbed by an amount $\delta d \in (0, 0.2\ell)$, with ℓ the minimum edge length on the network. For fig. 3.10, random sets of edges were selected for removal, such that the network retained a single connected component with each subsequent edge removed. The results are averaged over 10 different network structures generated by removing distinct sets of edges.

All edges in the synthetic networks were treated as straight lines between connected nodes.

B.3 Sampling transition times in simulations

B.3.1 Transition times between node neighborhoods

For a particle that starts at node i, we sample the distribution of times t for leaving the neighborhood of i according to the following algorithm.

First, we select the next node reached by the particle, using the discrete splitting probabilities P^*_{ik} (Eq. 3.8a). Next, consider the distribution of survival times $S_{ik}(t)$, conditional on the particle eventually leaving the neighborhood through node k:

$$S_{ik}(t) = \frac{1}{P^*_{ik}} \int_t^\infty P_{ik}(t')dt' = \frac{1}{P^*_{ik}} \sum_p \frac{r_p^{(ik)}}{Du_p^2} e^{-Du_p^2 t}. \tag{B.1}$$

The roots u_p for the Laplace inversion are precalculated for each neighborhood prior to the start of the simulation. The infinite summation is truncated to $u_p < u_{\max}$, with the maximum root for each neighborhood selected as described in B.3.2.

Sampling of the transition time is done through the inverse cumulant method, by first selecting a uniformly distributed value $w \in (0,1)$ and then numerically solving for the value of t with $S_{ik}(t) = w$.

In practice, we pre-tabulate the distributions of leaving times $S_{ik}(t)$ for each node and each adjacent edge in a network, allowing for rapid sampling of many particle transitions initiating at that node.

B.3.2 Short time asymptotic limit

Eq. 3.28 for the Laplace inversion of the leaving time distribution converges quickly for long times and short edges, with the number of required summation terms scaling as $\ell^2/(Dt)$. In the limit of short times, an alternate approach is taken for the Laplace inversion. Specifically, we expand Eq. 3.6 in the limit of $s \to \infty$ to get the lowest order terms

$$\begin{aligned} \widehat{P}_{ik} \xrightarrow{\alpha\to\infty} & \frac{2}{n}\left(e^{-\alpha\ell_{ik}} + e^{-3\alpha\ell_{ik}}\right) \\ & - \frac{4}{n^2}\sum_{j=1}^{n} e^{-\alpha(\ell_{ik}+2\ell_{ij})} \end{aligned} \tag{B.2}$$

where $\alpha = \sqrt{s/D}$ and n is the degree of node i.

We then use the relation

$$\mathscr{L}^{-1}\left(\frac{1}{s}e^{-2a\sqrt{s}}\right) = \operatorname{Erfc}\left(\frac{a}{\sqrt{t}}\right) \tag{B.3}$$

to invert the individual terms of Eq. B.2, integrated over time. This yields the final expression for the cumulative conditional probability that a particle leaves the neighborhood of node i by time t,

given it eventually leaves to node k:

$$1 - S_{ik}(t) \xrightarrow{t\to 0} \frac{2}{nP^*_{ik}}\left(\mathrm{Erfc}\left(\frac{\ell_{ik}}{2\sqrt{Dt}}\right) + \mathrm{Erfc}\left(\frac{3\ell_{ik}}{2\sqrt{Dt}}\right)\right) - \frac{4}{n^2 P^*_{ik}}\sum_j \mathrm{Erfc}\left(\frac{\ell_{ik}+2\ell_{ij}}{2\sqrt{Dt}}\right) \tag{B.4}$$

In order for this limit to be accurate, the next highest term in the expansion (Eq. B.2) needs to be sufficiently small. The next highest term for any given time is determined by the shortest edge length ($\ell_{i,\min}$) and must be at most $\mathrm{Erfc}\left[5\ell_{i,\min}/(2\sqrt{Dt})\right]$. Therefore, if we set a tolerance of ε, and define the cutoff $\xi = -\log\varepsilon$, then the expression in Eq. B.4 is accurate for all times t below

$$t^* = \frac{25\ell^2_{i,\min}}{4\xi D}. \tag{B.5}$$

For times above t^*, we can employ the converging series of Eq. 3.28. The series is truncated by considering only those poles that satisfy $Dt^* u^2_{\max} > \xi$, or equivalently

$$u_{\max} = \frac{2\xi}{5\ell_{\min}}.$$

Eq. 3.26 has poles at $m\pi/\ell_{ij}$ for all integer m and a root between every pair of consecutive poles. The maximum number of roots up to $u_{\max}$ is then given by

$$\sum_j m_{ij,\max} = \frac{2\xi}{5\pi\ell_{\min}}\sum_j \ell_{ij}. \tag{B.6}$$

The cumulative distribution function can therefore be evaluated efficiently for all values of time, so long as the ratio of longest to shortest edge length in the neighborhood is not too large.

An analogous approach can be used to find the no-passage spatial propagation of a

particle over a very short time interval, conditional on never leaving the neighborhood of the node. For a particle starting on node i that has never passed any of the adjacent nodes, the probability that after time t it is located on edge ik, between x and ℓ_{ik} can be derived from Eq. 3.29 as

$$\begin{aligned}
\widehat{Y}_{ik}(x,s) &\xrightarrow{\alpha\to\infty} \frac{2}{sn^2}\left[1-e^{-\alpha(\ell_{ik}-x)}\right]\sum_{j=1}^{n} e^{-2\alpha\ell_{ik}} \\
Y_{ik}(x,t) &\xrightarrow{t\to 0} \frac{2}{n^2}\sum_{j}\left[\operatorname{Erfc}\left(\frac{\ell_{ij}}{\sqrt{Dt}}\right)\right. \\
&\qquad \left. -\operatorname{Erfc}\left(\frac{2\ell_{ij}+\ell_{ik}-x}{\sqrt{Dt}}\right)\right]
\end{aligned} \tag{B.7}$$

This expression is normalized by $Y_{ik}(0,\Delta t)$, and allows for a sampling of the x coordinate using the inverse cumulant method.

B.3.3 Propagation on edges

For a particle starting at position x_0 on edge ik, the survival probability to time t given that it eventually leaves at one of the bounding nodes can be obtained directly via Eqs. B.1, B.4 by treating the starting position as its own node with adjacent nodes i and k connected by edges of length $\ell_{ik}-x_0$ and x_0, respectively. Analogously, Eqs. 3.30, B.7 can be leveraged to sample the spatial propagation along an edge over a time interval δt until the next save-point.

For this special case, the splitting probability and survival probability over time match to the known solutions for a particle on a one-dimensional interval with two absorbing boundaries [133, 66]. Namely, for a particle beginning at position x_0 on an edge of length ℓ_m, we

have

$$
\begin{aligned}
P_i &= x_0/\ell_m, \quad P_k = 1 - x_0/\ell_m, \\
S^{(E)}_{m,+}(t) &= \frac{2\ell_m}{\pi x_0} \sum_{p=1}^{\infty} \frac{(-1)^{(p+1)}}{p} \sin\left(\frac{p\pi x_0}{L}\right) e^{-\frac{p^2\pi^2 Dt}{\ell_m^2}}, \\
S^{(E)}_{m,-}(t) &= \frac{2\ell_m}{\pi(\ell_m - x_0)} \sum_{p=1}^{\infty} \frac{1}{p} \sin\left(\frac{p\pi x_0}{L}\right) e^{-\frac{p^2\pi^2 Dt}{\ell_m^2}},
\end{aligned}
\tag{B.8}
$$

where $S^{(E)}_{m,\pm}(t)$ correspond to the probability the particle has not left by time t, given it eventually leaves through the boundaries at ℓ_m and 0, respectively. Similarly, the no-passage spatial propagator for the particle on an edge can be expressed as,

$$
\begin{aligned}
Y^{(E)}_m(x,t) = \frac{2}{\pi} \sum_{p=1}^{\infty} \frac{1}{p} \sin\left(\frac{p\pi x_0}{\ell_m}\right) \\
\times \left[1 - \cos\left(\frac{p\pi x}{\ell_m}\right)\right] e^{-\frac{p^2\pi^2 Dt}{\ell_m^2}}.
\end{aligned}
\tag{B.9}
$$

For the short-time limit, analogous functions for a particle propagating on an edge can be derived from Eqs. B.4 and B.7.

B.3.4 Particle pair propagation

In order to avoid infinitesimally small steps when particles approach each other, it is necessary to enable two particles to share a single domain, where particle encounter is a finite-probability event within the domain. We follow the algorithm for paired particle propagation that was outlined previously in [66]. The essential points of the algorithm are presented here for completeness, and generalized to particles with arbitrary diffusivity.

Specifically, assume $x < y$ describe the coordinates of two particles along a segment with

absorbing boundaries at 0 and L. If we make the coordinate change defined by

$$\begin{aligned} u &= x - y \\ v &= \sqrt{\frac{D_y}{D_x}}x + \sqrt{\frac{D_x}{D_y}}y, \end{aligned} \tag{B.10}$$

then the time evolution for the joint distribution of the two particles can be expressed as a two-dimensional diffusion equation [196],

$$\frac{\partial c(u,v)}{\partial t} = (D_x + D_y)\left[\frac{\partial^2 c}{\partial u^2} + \frac{\partial^2 c}{\partial v^2}\right]. \tag{B.11}$$

The joint evolution of the transformed variables can thus be treated as two independent 1D diffusion processes, both with diffusivity $D_x + D_y$.

The edge segment domain containing a pair of particles is illustrated in Fig. B.1, which highlights the three boundaries for exiting the domain: $x = 0$ (first particle hits a segment boundary), $y = L$ (second particle hits a segment boundary), or $x = y$ (particles encounter each other). For simplicity of sampling we propagate the system forward within a smaller region inscribed within this two-dimensional domain. One option is to draw a rectangle (black dashed line in the figure), aligned with the x and y axes contained within the allowed domain. The particles are then propagated individually to the boundaries of the rectangle, using Eq. B.8 to find the earliest time for either particle to hit a boundary and Eq. B.9 to spatially propagate the other particle on the condition that it does not leave the rectangle. This approach, however, does not allow the particles to encounter each other and results in infinitesimally small time steps as the particles come close together. An alternate approach is to inscribe a parallelogram within the domain that has one edge on the $x = y$ line (corresponding to $u = 0$) and the other edges parallel to the v axis, along $v = a$ and $v = b$. The coordinates u and v are propagated diffusively within this parallelogram according to Eq. B.8 and B.9, and the two particle positions x, y are then recalculated accordingly. If the exit from the parallelogram happens along the line $u = 0$ then

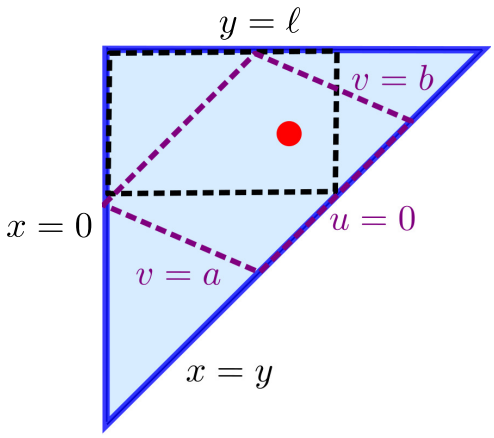

Figure B.1. Propagators used for an edge-segment protective domain containing a pair of particles. Blue lines mark absorbing boundaries in the domain. Red dot marks x_0, y_0, the initial positions of the two particles. Two propagation approaches are possible. The x and y coordinates can be propagated directly in an inscribed rectangular domain (black dashed lines). Alternately, the transformed coordinates u, v can be propagated in the region outlined in purple, allowing for particle encounter ($u = 0$) as a finite-probability outcome of the propagation step. The choice of propagation is based on greatest minimum distance to the boundary – in this case, the purple region would be used.

the particles encounter each other before leaving the domain and a reaction event is recorded.

The choice between the two subdomains (rectangle in x, y coordinates or in u, v coordinates) is made by picking the one with the biggest minimum distance of the initial pair position to the boundaries of the domain. In other words, when the particles start close together (u_0 close to 0), the u, v coordinate system is selected to allow an encounter to occur. When they are further apart, the x, y coordinate system is used to allow larger time steps in propagating to a domain boundary.

It should be noted that the time steps in this algorithm can get very small when two particles approach each other in the vicinity of a node, resulting in x and y both close to 0. However, our propagation approach allows for a substantial probability of either the particles encountering each other or one of the particles moving away from the node on a different segment, so that this unfavorable case does not persist for many time steps and does not substantially slow down the simulations when particle density is sparse.

Appendix C

Appendix for Chapter 4

C.1 Spatially heterogeneous accessibility observed for multiple ER structures

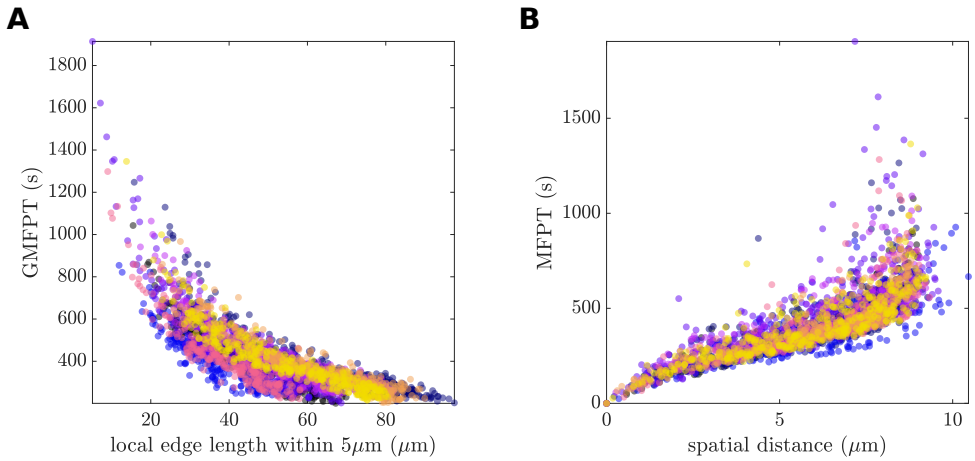

Figure C.1. Diffusive search times for extracted ER network structures. (A) Global mean first passage time (GMFPT) to each node in the network is plotted against the local network edge length (L_{loc}) within $\sigma = 5$ μm of the node. Compare to Fig. 1D. (B) Mean first passage time (MFPT) from a central node to target nodes on the ER network is plotted against Euclidean distance to the target node. Compare to Fig. 1F. In both plots, color indicates results for individual ER architectures (N=8 network regions extracted from 3 cells).

High spatial heterogeneity in network density and diffusive accessibility is observed across multiple excised ER networks. Using eight circular regions (radius 8.5 μm) of extracted ER network structure, local edge lengths and mean first passage times are calculated, as for the example network shown in Fig. 1.

The global mean first passage time (GMFPT) to every node in each network (Fig. C.1A) again scales inversely with local edge length. In individual networks, GMFPT can vary by nearly one order of magnitude with similar variation observed in the distributions of local edge length. Notably, the variation within a single network structure is comparable to the overall variation between networks extracted from different cells. Thus, even a well-connected, highly-looped structure like the ER can exhibit large spatial fluctuations in diffusive accessibility, an effect that is observed across multiple peripheral ER architectures.

We next consider a more localized search process wherein a particle begins its search from a central source node (Fig. C.1B). The mean first passage time (MFPT) to each possible target node in the ER structures exhibits the characteristic scaling with distance previously discussed in the main text and elsewhere [63]. Fluctuations in ER density and connectivity lead to large deviations from the smooth scaling seen in uniform networks (see Fig. 1E). This implies that in the ER search times for targets that are equidistant from a central source can vary substantially depending on the local geometry.

C.2 Computing mean first passage times on reservoir networks

Our base model treats regions of the ER as networks of edges connected at point-like junctions. This model assumes that the size of the network junctions is comparable to the tubule width. However, the peripheral ER can also include some sheet-like regions that are substantially larger than the tubule width [155]. Such peripheral sheet regions would form spatially expanded junctions that could serve as localized traps for diffusing particles. We therefore consider an expansion of our model that incorporates enlarged junction regions from which particles escape through narrow holes along the boundary.

In addition, the perinuclear region of the ER forms a complex structure composed of interconnected stacks of sheets. The detailed structure of the perinuclear ER cannot be resolved

with confocal microscopy, but given the large extent of the region we might also expect it to serve as a substantial trap for diffusing particles. A simplified representation of the perinuclear region would also treat it as a disk-shaped reservoir connected to many tubules around its circumference. We use the same mathematical approach to handle the large perinuclear region as we do for the enlarged junction nodes. This approach is described below.

We propose a "reservoir network" model for calculating analytic mean first passage times in a structure composed of tubes that are joined either at point-like nodes or at larger reservoirs. The approximate analytical approach for transitions between reservoirs and tubes is inspired by previous work describing diffusive escape from pores in cylindrical geometries [168].

In essence, the model represents transitions of particles between disk-shaped reservoirs and connecting tubules (Fig. C.2A) by decomposing the system into several discrete spatial states (Fig. C.2B), in a manner analogous to the classic paper on diffusion-limited reactions by Berg and Purcell [197]. By using a state-based approach, it is then possible to calculate MFPTs on these hybrid reservoir networks using the previously described graph-theoretic approach [67].

In Supplemental Section C.3 we apply this model to study the effect of scattered reservoirs on average search times on a network. Additionally, in the main text, a single reservoir representing the sheet-like ER in the perinuclear region is used to more accurately capture search times on a whole-cell scale.

C.2.1 State diagram for a single reservoir

Reservoirs are treated as disks of radius R_+, with holes in the boundary of width 2δ representing connected tubes (a typical geometry is shown in Fig. C.2A with the corresponding state diagram in Fig. C.2B). An optional target at the center with radius R_- is denoted the central state, C. When a particle enters the reservoir from an adjoining tube it is placed in the boundary state, B, a distance σ from the outer wall of the reservoir. The value of σ is chosen to be comparable to the tube size, and represents a distance from which the particle can take independent samples of the domain wall without maintaining a strong memory of the tubule

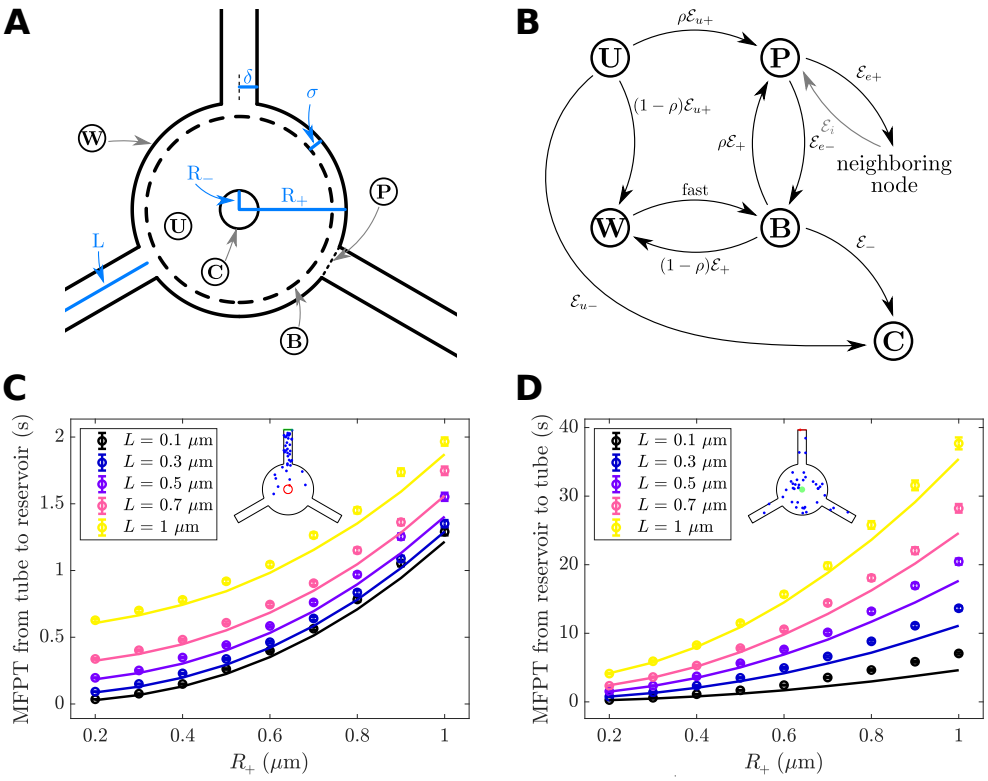

Figure C.2. Reservoir network model. (A) Representative geometry for a three-tube reservoir embedded in the network. Dimensions of the system are highlighted in light blue. The five states and their locations in space are denoted by circled capital letters. (B) The state diagram for the effective model with transition probabilities labeled. The reservoir may be embedded in a larger network, so an additional neighboring node state is depicted where the transition into P from the neighbor is given as in [67]. (C) Analytic MFPTs (lines) reproduce MFPT from BD simulations (points) of 2000 particles diffusing ($D = 1\ \mu\text{m}^2/\text{s}$) across wide range of symmetric triskelion geometries. Error bars show standard error of the mean. Inset: particles (active, blue; absorbed, red) start at the green tip of one tube and diffuse until reaching the red target at the center of the reservoir. (D) Simulations validate the reverse process. Inset: particles start at the center of the reservoir (green) and diffuse until reaching the tip of the top tube (red).

from which it came. From state B, the particle can either transition back towards the wall or take the long journey to the center of the reservoir, with splitting probabilities ($\mathscr{E}_{\pm}$) and average

waiting time until the transition (Q_B) given by:

$$\begin{aligned}
\mathscr{E}_+ &= \log\left(\frac{R_+ - \sigma}{R_-}\right) / \log\left(\frac{R_+}{R_-}\right), \\
\mathscr{E}_- &= 1 - \mathscr{E}_+, \\
Q_B &= \frac{1}{4D\log\left(\frac{R_-}{R_+}\right)}\left((R_+ - \sigma)^2 \log\left(\frac{R_+}{R_-}\right) + R_+^2 \log\left(\frac{R_-}{R_+ - \sigma}\right) + R_-^2 \log\left(\frac{R_+ - \sigma}{R_+}\right)\right).
\end{aligned} \tag{C.1}$$

Here D is the particle diffusivity, $\mathscr{E}_+$ is the probability of hitting the wall before the central target, and $\mathscr{E}_-$ is the probability of first hitting the central target. If there is no target at the center of the reservoir, then $R_- \to 0$ and $\mathscr{E}_+ = 1$. These expressions are derived from the standard solution of first passage times for the diffusion equation in cylindrical coordinates [133].

If the particle first hits the wall, it has a chance $\rho = \frac{\delta d}{\pi R_+}$ of entering a P state, where d is the number of tubules connected to the reservoir. The particle is equally likely to hit each P state (this does not mean it will reach the connected node with equal probability, which depends on the length of the intervening edge). The P state can be thought of as a network node connected to two edges: one of length L leading to the neighboring node outside the reservoir and one of length σ leading into the reservoir. The splitting probability from P to B is simply $\mathscr{E}_{e-} = \sigma/(L+\sigma)$. If the particle instead hits the wall, W (probability $1-\rho$), it rapidly transitions back to state B. Assuming σ is small compared to R_+, the waiting time in W will be negligible compared to the time spent performing searches of the bulk. This approach for exit out of a reservoir through a long tube has been previously described for cylindrical geometries [168].

Included in the state diagram is an additional state, U, an optional initial state representing a uniform distribution of particles throughout the reservoir. The splitting probabilities and waiting

times unique to state U are given by:

$$\begin{aligned}
\mathscr{E}_{u+} &= \frac{R_+^2}{R_+^2 - R_-^2} + \frac{1}{2\log\left(\frac{R_-}{R_+}\right)}, \\
\mathscr{E}_{u-} &= 1 - \mathscr{E}_{u+}, \\
Q_U &= \frac{1}{8D}\left(R_-^2 + R_+^2 + \frac{R_-^2 - R_+^2}{\log\left(\frac{R_+}{R_-}\right)}\right).
\end{aligned} \tag{C.2}$$

For simplicity, this state diagram represents a reservoir with one connected tubule. In practice, there are often multiple P states, each connected to a neighboring node. Then the transitions from U and B to each P_i would be symmetric and scaled by the degree (number of neighbors) of the reservoir.

This reservoir model can be inserted into previously described network models of the ER. Using the splitting probabilities and waiting times for each state, it is possible to calculate analytic mean first passage times for diffusive search in the reservoir as previously described in [67].

C.2.2 BD simulations in triskelion geometries validate analytic approach

The analytic model is validated through the use of Brownian dynamics simulations on triskelion geometries with a wide range of sizes (Fig. C.2C,D insets). The radius of the reservoir, R_+ is varied between $0.2 - 1.0$ μm and the length of the connected tubules is varied from $0.1 - 1.0$ μm. The radius of the tubes is fixed at $\delta = 0.05$ μm, a typical size for ER tubules in COS7 cells [155, 167]. The modified tube size, is set to $\sigma = \pi\delta/4$ as in [168, 197]. In all of these tests (and later applications), the central target has radius $R_- = \delta$ so that targets placed in either a tube or a reservoir have the same size.

Two representative search problems are analyzed on these geometries. In the first test, 2000 particles are placed at the end of a tube and allowed to diffuse until reaching an absorbing disk at the center of the reservoir (Fig. C.2C). In the second, 2000 particles begin at the center of

the reservoir and diffuse until reaching the end of a specific tube. The time step for both tests is 10^{-5} s, with particle diffusivity $D = 1\ \mu\text{m}^2/\text{s}$. The MFPT is recorded and compared to the analytic MFPT from the corresponding reservoir network (Fig. C.2C,D).

Over a wide range of scales for both R_+ and L the analytic model approximately reproduces simulated mean first passage times. Having validated a single triskelion, it is now possible to intersperse these reservoir structures throughout existing networks and obtain realistic mean first passage times on reservoir networks.

C.3 Presence of scattered reservoirs increases trapping, GMFPT

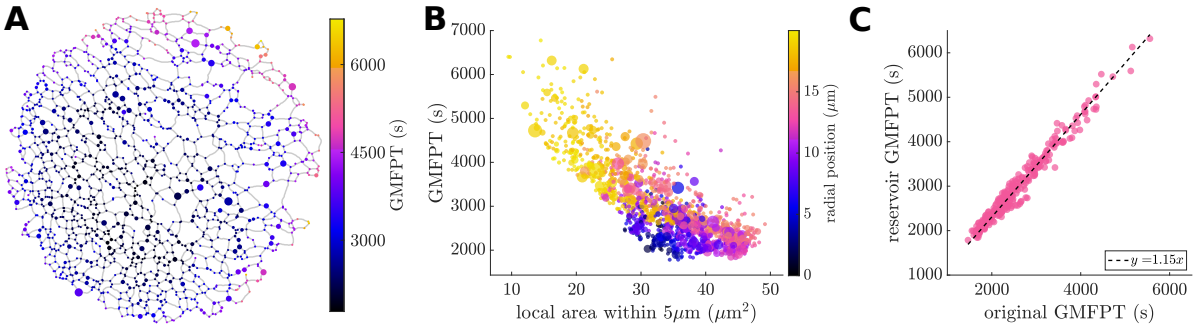

Figure C.3. Reservoir network model of a COS7 ER. (A) Global mean first passage times (GMFPTs) to targets on nodes on an example COS7 ER network (from Fig. 1A) where now 20% of network nodes are converted to reservoirs. Reservoir nodes are shown as true size, point-like nodes are plotted with a fixed minimum size for visibility. (B) GMFPT scales inversely with local network surface area. Color denotes radial position from center of network, enlarged points indicate reservoirs and their relative size. (C) The GMFPT to central targets in reservoirs scales linearly with GMFPT of the original nodes (prior to conversion to reservoir).

By treating the peripheral ER as a network of one-dimensional tubules we are able to focus on large-scale structure and connectivity. This enables us to model transport in the ER as diffusion on a network, where simple computational approaches provide powerful predictions that agree with experimental results (Fig. 2E). Here we investigate the limits of the network model by considering the effect of scattering enlarged junction reservoirs over a network.

A COS7 peripheral ER is modeled as a reservoir network by randomly selecting 20%

of its nodes and converting them into reservoirs. The reservoir radii (R_+) are set to be 0.45 of the minimum edge length connected to the node, giving an average size of 0.26 μm. Connected edges shrink to accommodate the reservoirs. This avoids unphysical overlap of reservoirs and edges and allows for a heterogeneous distribution of reservoirs to be randomly dispersed across the network. The GMFPT is calculated to targets of radius $R_- = 0.05$ μm placed in the center of each expanded node, as well as to all the ordinary point-like junctions. Because the particles are meant to represent ER membrane proteins, the starting probability for each node is set in proportion to surface area, with non-reservoir nodes assigned surface area $2\pi\delta^2$, while reservoirs have surface area $2\pi R_+^2$.

We find that even in the presence of many reservoirs, the qualitative trends for network search times are the same. GMFPT still scales with the amount of locally accessible network (in this case, surface area, Fig. C.3B). For each individual reservoir target, we compare its GMFPT in a network with many reservoirs versus the GMFPT to the same node on a network with point-like junctions only (Fig. C.3C). The main effect of enlarged junction reservoirs is a slight increase in search times. This is due to the increase in network surface area and the trapping that occurs inside of reservoirs; there is more space for particles to explore before finding any given target and thus average search times increase. Notably, the breadth of the search-time distribution does not change substantially upon the introduction of randomly scattered enlarged reservoirs. Thus, treating the ER tubule junctions as point-like connections appears to be a reasonable simplification for these network structures.

C.4 Alternative methods of incorporating network dynamics into simulations of particle diffusion

When modeling the spread of photoactivated diffusing particles from a central region, the dynamic rearrangements of the ER network need to be considered. In the main text, we incorporate the effects of the time-varying ER structure by averaging multiple simulations on

static networks extracted from individual frames of the experimental movie. Here, we analyze two alternatives: (1) simulations run only on a single network extracted from the first frame; and (2) a "project and propagate" approach incorporating many network snapshots in each simulation. In both cases, the same two rounds of filtering are applied when comparing to the experimental signal.

For approach (1), the simulated fractional signal on the network extracted from frame 1 (f_{1ij}^{sim}) is plotted in Fig. C.4A.ii. We calculate the slope of the signal in each wedge j over the first 10 seconds after photoactivation. These arrival rates are compared to the averaged simulated rates from the main text (computed from the averaged fractional signal shown in Fig. C.4A.iii). We see strong agreement between the two ($R^2 = 0.91$, Fig. C.4B, blue dots and dashed line). Consequently, this approach also does reasonably well in predicting the experimentally measured protein arrival rates (extracted from Fig. C.4A.i), with $R^2 = 0.6$ (Fig, C.4C, blue dots and dashed line). Approach 1 includes no information about the network rearrangements over time, but still captures much of the behavior of proteins in the ER.

For the project and propagate simulations, 50000 particles commence diffusion from the photoactivation region on the network extracted from the first frame of the movie. The photoactivated particles then diffuse along the first network for time $dt = 0.6$s, at which point they are projected from their location in space to the closest point on the network extracted from the second frame of the experimental movie. The projection step tends to be small compared to the diffusive (or propagation) step because the network evolves slowly in time compared to the diffusion of individual particles. The diffusive particles repeat this process, propagating and projecting, until the final frame of the experiment is reached.

One advantage of this method is that it more realistically captures the expected spatial trajectories of particles diffusing on a continuously rearranging network. As time progresses and the proteins diffuse from the photoactivation region, the network evolves in time as well, albeit with a large time step set by the experimental frame rate.

The same nine photoactivation runs are analyzed using the project and propagate simula-

tion method. We again define individual wedge regions of the same size and location as in the experimental images and analyze the number of particles in each. The simulated signal in each wedge (w_{ij}^{pp}) is then defined as the total number of particles in wedge j at time point i, and the fractional signal (Fig. C.4A.iv) is $f_{ij}^{\mathrm{pp}} = w_{ij}^{\mathrm{pp}}/N$. These fractional signals do not require averaging as in the main text, because the effects of the dynamic network are already incorporated via the project and propagate method. The fractional signals are then used to find the signal arrival rate (slope over first 10 seconds), just as before.

Again, we see strong agreement between the project and propagate simulations and the results from the main text when comparing the calculated arrival rates (Fig. C.4B). The project and propagate method is also able to predict the experimental arrival rates well: $R^2 = 0.64$ (Fig. C.4C), as compared to $R^2 = 0.68$ in the main text.

Both project and propagate and the frame-averaged approach outlined in the main text generate simulated protein arrival rates that fit the experimental rates slightly better than the static approach using the first frame only. These approaches for incorporating ER network dynamics thus help account for the time-varying tubule density and connectivity within each ER region. Thus, although ER network dynamics are shown to be quite slow, incorporation of the different network structures over time allows for a better representation of observed particle motion.

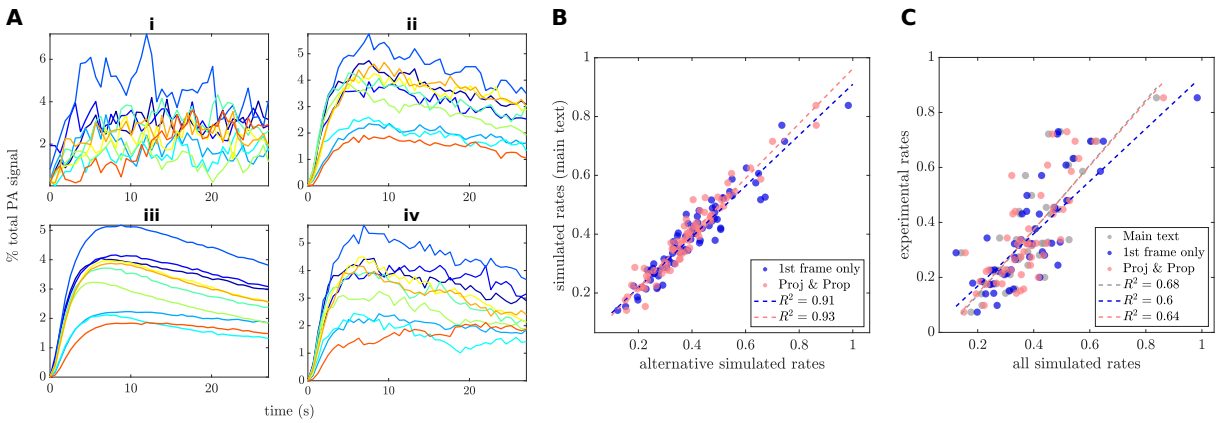

Figure C.4. Alternative simulations of diffusive spread in the ER. (A) Fractional photoactivated signal vs time curves for a single cell from experiment and simulations: (i) experimental signal, (ii) simulated signal on the network from the first frame, (iii) simulated signal averaged over networks from each frame of the experimental movie (as used in main text, Fig. 1E), and (iv) simulated signal from the project and propagate approach. (B) Correlation of signal arrival rates from alternative simulation approaches with the averaging approach used in the main text. (C) Correlations of simulated rates with experimental protein arrival rates.

Bibliography

[1] Bruce Alberts, Rebecca Heald, Alexander Johnson, David Morgan, Martin Raff, Keith Roberts, and Peter Walter. *Molecular Biology of the Cell*. WW Norton & Company, 2022.

[2] Ben P Phillips, Natalia Gomez-Navarro, and Elizabeth A Miller. Protein quality control in the endoplasmic reticulum. *Curr Opin Cell Biol*, 65:96–102, 2020.

[3] Lea Daverkausen-Fischer and Felicitas Pröls. Regulation of calcium homeostasis and flux between the endoplasmic reticulum and the cytosol. *J Biol Chem*, 298(7), 2022.

[4] Cécile C Crapart, Zubenelgenubi C Scott, Tasuku Konno, Aman Sharma, Pierre Parutto, David MD Bailey, Laura M Westrate, Edward Avezov, and Elena F Koslover. Luminal transport through intact endoplasmic reticulum limits the magnitude of localized ca2+ signals. *P Natl Acad Sci*, 121(13):e2312172121, 2024.

[5] Tamas Balla, Yeun Ju Kim, Alejandro Alvarez-Prats, and Joshua Pemberton. Lipid dynamics at contact sites between the endoplasmic reticulum and other organelles. *Annu Rev Cell Dev Bi*, 35:85–109, 2019.

[6] Julie Jacquemyn, Ana Cascalho, and Rose E Goodchild. The ins and outs of endoplasmic reticulum-controlled lipid biosynthesis. *EMBO Rep*, 18(11):1905–1921, 2017.

[7] Haoxi Wu, Pedro Carvalho, and Gia K Voeltz. Here, there, and everywhere: The importance of er membrane contact sites. *Science*, 361(6401):eaan5835, 2018.

[8] Luca Scorrano, Maria Antonietta De Matteis, Scott Emr, Francesca Giordano, György Hajnóczky, Benoît Kornmann, Laura L Lackner, Tim P Levine, Luca Pellegrini, Karin Reinisch, Rosario Rizzuto, Thomas Simmen, Harald Stenmark, Christian Ungermann, and Maya Schuldiner. Coming together to define membrane contact sites. *Nat Commun*, 10(1):1287, 2019.

[9] LM Westrate, JE Lee, WA Prinz, and GK Voeltz. Form follows function: the importance of endoplasmic reticulum shape. *Annu. Rev. Biochem*, 84(1):791–811, 2015.

[10] Charles Barlowe, Lelio Orci, Tom Yeung, Midori Hosobuchi, Susan Hamamoto, Nina Salama, Michael F Rexach, Mariella Ravazzola, Mylène Amherdt, and Randy Schekman. Copii: a membrane coat formed by sec proteins that drive vesicle budding from the endoplasmic reticulum. *Cell*, 77(6):895–907, 1994.

[11] Ken Matsuoka, Lelio Orci, Mylène Amherdt, Sebastian Y Bednarek, Susan Hamamoto, Randy Schekman, and Thomas Yeung. Copii-coated vesicle formation reconstituted with purified coat proteins and chemically defined liposomes. *Cell*, 93(2):263–275, 1998.

[12] Peter Watson, Anna K Townley, Pratyusha Koka, Krysten J Palmer, and David J Stephens. Sec16 defines endoplasmic reticulum exit sites and is required for secretory cargo export in mammalian cells. *Traffic*, 7(12):1678–1687, 2006.

[13] Laura M Westrate, Melissa J Hoyer, Michael J Nash, and Gia K Voeltz. Vesicular and uncoated rab1-dependent cargo carriers facilitate er to golgi transport. *J Cell Sci*, 133(14):jcs239814, 2020.

[14] Craig Blackstone. Cellular pathways of hereditary spastic paraplegia. *Annual review of neuroscience*, 35(1):25–47, 2012.

[15] Zeynep Öztürk, Cahir J O'Kane, and Juan José Pérez-Moreno. Axonal endoplasmic reticulum dynamics and its roles in neurodegeneration. *Frontiers in neuroscience*, 14:48, 2020.

[16] Md Golam Sharoar, Qi Shi, Yingying Ge, Wanxia He, Xiangyou Hu, George Perry, Xiongwei Zhu, and Riqiang Yan. Dysfunctional tubular endoplasmic reticulum constitutes a pathological feature of alzheimer's disease. *Molecular psychiatry*, 21(9):1263–1271, 2016.

[17] Christopher J Obara, Andrew S Moore, and Jennifer Lippincott-Schwartz. Structural diversity within the endoplasmic reticulum—from the microscale to the nanoscale. *Cold Spring Harb Perspect Biology*, 15(6):a041259, 2023.

[18] Junjie Hu, Yoko Shibata, Christiane Voss, Tom Shemesh, Zongli Li, Margaret Coughlin, Michael M Kozlov, Tom A Rapoport, and William A Prinz. Membrane proteins of the endoplasmic reticulum induce high-curvature tubules. *Science*, 319(5867):1247–1250, 2008.

[19] Gia K Voeltz, William A Prinz, Yoko Shibata, Julia M Rist, and Tom A Rapoport. A class of membrane proteins shaping the tubular endoplasmic reticulum. *Cell*, 124(3):573–586, 2006.

[20] Yoko Shibata, Tom Shemesh, William A Prinz, Alexander F Palazzo, Michael M Kozlov, and Tom A Rapoport. Mechanisms determining the morphology of the peripheral er. *Cell*, 143(5):774–788, 2010.

[21] Bowen Wang, Zhiheng Zhao, Michael Xiong, Rui Yan, and Ke Xu. The endoplasmic reticulum adopts two distinct tubule forms. *P Natl Acad Sci*, 119(18):e2117559119, 2022.

[22] Songyu Wang, Hanna Tukachinsky, Fabian B Romano, and Tom A Rapoport. Cooperation of the er-shaping proteins atlastin, lunapark, and reticulons to generate a tubular membrane network. *elife*, 5:e18605, 2016.

[23] Junjie Hu, Yoko Shibata, Peng-Peng Zhu, Christiane Voss, Neggy Rismanchi, William A Prinz, Tom A Rapoport, and Craig Blackstone. A class of dynamin-like gtpases involved in the generation of the tubular er network. *Cell*, 138(3):549–561, 2009.

[24] Genny Orso, Diana Pendin, Song Liu, Jessica Tosetto, Tyler J Moss, Joseph E Faust, Massimo Micaroni, Anastasia Egorova, Andrea Martinuzzi, James A McNew, and Andrea Daga. Homotypic fusion of er membranes requires the dynamin-like gtpase atlastin. *Nature*, 460(7258):978–983, 2009.

[25] NS Gov. Phases of membrane tubules pulled by molecular motors. *Soft Matter*, 5(12):2431–2437, 2009.

[26] Ben Zucker and Michael M Kozlov. Mechanism of shaping membrane nanostructures of endoplasmic reticulum. *P Natl Acad Sci*, 119(1):e2116142119, 2022.

[27] Marcin J Wozniak, Becky Bola, Kim Brownhill, Yen-Ching Yang, Vesselina Levakova, and Victoria J Allan. Role of kinesin-1 and cytoplasmic dynein in endoplasmic reticulum movement in vero cells. *J Cell Sci*, 122(12):1979–1989, 2009.

[28] Jonathan R Friedman, Brant M Webster, David N Mastronarde, Kristen J Verhey, and Gia K Voeltz. Er sliding dynamics and er–mitochondrial contacts occur on acetylated microtubules. *J Cell Biol*, 190(3):363–375, 2010.

[29] Clare M Waterman-Storer and ED Salmon. Endoplasmic reticulum membrane tubules are distributed by microtubules in living cells using three distinct mechanisms. *Curr Biol*, 8(14):798–807, 1998.

[30] Jonathan R Friedman, Jared R DiBenedetto, Matthew West, Ashley A Rowland, and Gia K Voeltz. Endoplasmic reticulum–endosome contact increases as endosomes traffic and mature. *Mol Biol Cell*, 24(7):1030–1040, 2013.

[31] Meng Lu, Francesca W van Tartwijk, Julie Qiaojin Lin, Wilco Nijenhuis, Pierre Parutto, Marcus Fantham, Charles N Christensen, Edward Avezov, Christine E Holt, Alan Tunnacliffe, David Holcman, Lukas Kapitein, Gabriele S Kaminski Schierle, and Clemens F Kaminski. The structure and global distribution of the endoplasmic reticulum network are actively regulated by lysosomes. *Sci Adv*, 6(51):eabc7209, 2020.

[32] Jonathan R Friedman, Laura L Lackner, Matthew West, Jared R DiBenedetto, Jodi Nunnari, and Gia K Voeltz. Er tubules mark sites of mitochondrial division. *Science*, 334(6054):358–362, 2011.

[33] D.L. Weaire and S. Hutzler. *The Physics of Foams*. Clarendon Press, 2001.

[34] Alexander G Fletcher, Miriam Osterfield, Ruth E Baker, and Stanislav Y Shvartsman. Vertex models of epithelial morphogenesis. *Biophys J*, 106(11):2291–2304, 2014.

[35] Carl V Thompson. Grain growth in thin films. *Annu Rev Mater Sci*, 20(1):245–268, 1990.

[36] Ashley A Rowland, Patrick J Chitwood, Melissa J Phillips, and Gia K Voeltz. Er contact sites define the position and timing of endosome fission. *Cell*, 159(5):1027–1041, 2014.

[37] Lorenz Stadler, Konstantin Speckner, and Matthias Weiss. Diffusion of exit sites on the endoplasmic reticulum: a random walk on a shivering backbone. *Biophys J*, 115(8):1552–1560, 2018.

[38] Maria S Tikhomirova, Avihay Kadosh, Aksel J Saukko-Paavola, Tom Shemesh, and Robin W Klemm. A role for endoplasmic reticulum dynamics in the cellular distribution of microtubules. *P Natl Acad Sci*, 119(15):e2104309119, 2022.

[39] Congping Lin, Yiwei Zhang, Imogen Sparkes, and Peter Ashwin. Structure and dynamics of er: minimal networks and biophysical constraints. *Biophys J*, 107(3):763–772, 2014.

[40] Congping Lin, Rhiannon R White, Imogen Sparkes, and Peter Ashwin. Modeling endoplasmic reticulum network maintenance in a plant cell. *Biophys J*, 113(1):214–222, 2017.

[41] Reinhard Lipowsky, Shreya Pramanik, Amelie S Benk, Miroslaw Tarnawski, Joachim P Spatz, and Rumiana Dimova. Elucidating the morphology of the endoplasmic reticulum: puzzles and perspectives. *ACS nano*, 17(13):11957–11968, 2023.

[42] Olivier Bénichou, Claire Chevalier, Bob Meyer, and Raphaël Voituriez. Facilitated diffusion of proteins on chromatin. *Phys Rev Lett*, 106(3):038102, 2011.

[43] Elena F. Koslover, Mario A. Díaz De La Rosa, and Andrew J. Spakowitz. Theoretical and computational modeling of target-site search kinetics in vitro and in vivo. *Biophys J*, 101(4):856–865, 2011.

[44] Ludvig Lizana, Zoran Konkoli, Brigitte Bauer, Aldo Jesorka, and Owe Orwar. Controlling chemistry by geometry in nanoscale systems. *Annu Rev Phys Chem*, 60:449–468, 2009.

[45] Aidan I Brown, Laura M Westrate, and Elena F Koslover. Impact of global structure on diffusive exploration of organelle networks. *Sci Rep*, 10(1):1–13, 2020.

[46] Brett G Zani and Elazer R Edelman. Cellular bridges: Routes for intercellular communication and cell migration. *Commun Integr Biol*, 3(3):215–220, 2010.

[47] Olivier Bénichou, C Chevalier, Joseph Klafter, B Meyer, and Raphael Voituriez. Geometry-controlled kinetics. *Nat Chem*, 2(6):472–477, 2010.

[48] O. Bénichou and R. Voituriez. From first-passage times of random walks in confinement to geometry-controlled kinetics. *Physics Reports*, 539(4):225–284, 2014.

[49] Koichi Takahashi, Sorin Tănase-Nicola, and Pieter Rein Ten Wolde. Spatio-temporal correlations can drastically change the response of a mapk pathway. *P Natl Acad Sci*, 107(6):2473–2478, 2010.

[50] Steven M Abel, Jeroen P Roose, Jay T Groves, Arthur Weiss, and Arup K Chakraborty. The membrane environment can promote or suppress bistability in cell signaling networks. *J Phys Chem B*, 116(11):3630–3640, 2012.

[51] Vahe Galstyan, Kabir Husain, Fangzhou Xiao, Arvind Murugan, and Rob Phillips. Proofreading through spatial gradients. *elife*, 9:e60415, 2020.

[52] Mykyta V Chubynsky and Gary W Slater. Diffusing diffusivity: a model for anomalous, yet brownian, diffusion. *Phys Rev Lett*, 113(9):098302, 2014.

[53] Rohit Jain and Kizhakeyil L Sebastian. Diffusing diffusivity: survival in a crowded rearranging and bounded domain. *J Phys Chem B*, 120(34):9215–9222, 2016.

[54] Yann Lanoiselée, Nicolas Moutal, and Denis S Grebenkov. Diffusion-limited reactions in dynamic heterogeneous media. *Nature Commun*, 9(1):1–16, 2018.

[55] Matheus P Viana, Aidan I Brown, Irina A Mueller, Claire Goul, Elena F Koslover, and Susanne M Rafelski. Mitochondrial fission and fusion dynamics generate efficient, robust, and evenly distributed network topologies in budding yeast cells. *Cell Syst*, 10(3):287–297, mar 2020.

[56] Fabio Sartori, Anne-Sophie Hafner, Ali Karimi, Andreas Nold, Yombe Fonkeu, Erin M Schuman, and Tatjana Tchumatchenko. Statistical laws of protein motion in neuronal dendritic trees. *Cell Rep*, 33(7):108391, 2020.

[57] Jean Philippe Bouchaud and Antoine Georges. Anomalous diffusion in disordered media: Statistical mechanisms, models and physical applications. *Physics Reports*, 195(4-5):127–293, 1990.

[58] Steven L Bryant, David W Mellor, and Christopher A Cade. Physically representative network models of transport in porous media. *Aiche J*, 39(3):387–396, 1993.

[59] Marc Barthélemy. Spatial networks. *Phys Rep*, 499(1-3):1–101, 2011.

[60] Jae Dong Noh and Heiko Rieger. Random walks on complex networks. *Phys Rev Lett*, 92(11):118701, 2004.

[61] S Hwang, D-S Lee, and B Kahng. First passage time for random walks in heterogeneous networks. *Phys Rev Lett*, 109(8):088701, 2012.

[62] David J Wales. Discrete path sampling. *Mol Phys*, 100(20):3285–3305, 2002.

[63] M Dora and D Holcman. Active flow network generates molecular transport by packets: case of the endoplasmic reticulum. *Proc Royal Soc B*, 287(1930):20200493, 2020.

[64] Denis S Grebenkov and Liubov Tupikina. Heterogeneous continuous-time random walks. *Phys Rev E*, 97(1):012148, 2018.

[65] Z Schuss, K Basnayake, and D Holcman. Redundancy principle and the role of extreme statistics in molecular and cellular biology. *Phys Life Rev*, 28:52–79, 2019.

[66] Tomas Oppelstrup, Vasily V Bulatov, Aleksandar Donev, Malvin H Kalos, George H Gilmer, and Babak Sadigh. First-passage kinetic monte carlo method. *Phys Rev E*, 80(6):066701, 2009.

[67] Zubenelgenubi C Scott, Aidan I Brown, Saurabh S Mogre, Laura M Westrate, and Elena F Koslover. Diffusive search and trajectories on tubular networks: a propagator approach. *Eur Phys J E*, 44(6):1–20, 2021.

[68] Lars Ellgaard and Ari Helenius. Quality control in the endoplasmic reticulum. *Nat Rev Mol Cell Bio*, 4(3):181–191, 2003.

[69] Tom Shemesh, Robin W Klemm, Fabian B Romano, Songyu Wang, Joshua Vaughan, Xiaowei Zhuang, Hanna Tukachinsky, Michael M Kozlov, and Tom A Rapoport. A model for the generation and interconversion of er morphologies. *P Natl Acad Sci*, 111(49):E5243–E5251, 2014.

[70] Hannah T Perkins, Victoria J Allan, and Thomas A Waigh. Network organisation and the dynamics of tubules in the endoplasmic reticulum. *Sci Rep*, 11(1):16230, 2021.

[71] Christopher Lee and Lan Bo Chen. Dynamic behavior of endoplasmic reticulum in living cells. *Cell*, 54(1):37–46, 1988.

[72] John von Neumann. Discussion: Shape of metal grains. *Metal Interfaces*, 108, 1952.

[73] Robert D MacPherson and David J Srolovitz. The von neumann relation generalized to coarsening of three-dimensional microstructures. *Nature*, 446(7139):1053–1055, 2007.

[74] Tsvi Tlusty, SA Safran, R Menes, and R Strey. Scaling laws for microemulsions governed by spontaneous curvature. *Physical review letters*, 78(13):2616, 1997.

[75] US Schwarz and G Gompper. Bending frustration of lipid- water mesophases based on cubic minimal surfaces1. *Langmuir*, 17(7):2084–2096, 2001.

[76] William W Mullins. Two-dimensional motion of idealized grain boundaries. *J Appl Phys*, 27(8):900–904, 1956.

[77] Michio Tateno and Shuji Ishihara. Interfacial-curvature-driven coarsening in mass-conserved reaction-diffusion systems. *Phys Rev Res*, 3(2):023198, 2021.

[78] Fridtjof Brauns, Henrik Weyer, Jacob Halatek, Junghoon Yoon, and Erwin Frey. Wavelength selection by interrupted coarsening in reaction-diffusion systems. *Phys Rev Lett*, 126(10):104101, 2021.

[79] D Weaire and S McMurry. Some fundamentals of grain growth. In *Solid state physics*, volume 50, pages 1–36. Elsevier, 1996.

[80] Jonathon Nixon-Abell, Christopher J Obara, Aubrey V Weigel, Dong Li, Wesley R Legant, C Shan Xu, H Amalia Pasolli, Kirsten Harvey, Harald F Hess, Eric Betzig, Craig Blackstone, and Jennifer Lippincott-Schwarz. Increased spatiotemporal resolution reveals highly dynamic dense tubular matrices in the peripheral er. *Science*, 354(6311):aaf3928, 2016.

[81] Robert E Powers, Songyu Wang, Tina Y Liu, and Tom A Rapoport. Reconstitution of the tubular endoplasmic reticulum network with purified components. *Nature*, 543(7644):257–260, 2017.

[82] Ilya Grigoriev, Susana Montenegro Gouveia, Babet van der Vaart, Jeroen Demmers, Jeremy T Smyth, Srinivas Honnappa, Daniël Splinter, Michel O Steinmetz, James W Putney, Casper C Hoogenraad, and Anna Akhamanova. Stim1 is a mt-plus-end-tracking protein involved in remodeling of the er. *Curr Biol*, 18(3):177–182, 2008.

[83] Anthony T Chieco, James P Sethna, and Douglas J Durian. Average evolution and size-topology relations for coarsening 2d dry foams. *Front Soft Matter*, 2:941811, 2022.

[84] Alex M Valm, Sarah Cohen, Wesley R Legant, Justin Melunis, Uri Hershberg, Eric Wait, Andrew R Cohen, Michael W Davidson, Eric Betzig, and Jennifer Lippincott-Schwartz. Applying systems-level spectral imaging and analysis to reveal the organelle interactome. *Nature*, 546(7656):162–167, 2017.

[85] Khuloud Jaqaman, Dinah Loerke, Marcel Mettlen, Hirotaka Kuwata, Sergio Grinstein, Sandra L Schmid, and Gaudenz Danuser. Robust single-particle tracking in live-cell time-lapse sequences. *Nat Methods*, 5(8):695–702, 2008.

[86] Pengli Zheng, Christopher J Obara, Ewa Szczesna, Jonathon Nixon-Abell, Kishore K Mahalingan, Antonina Roll-Mecak, Jennifer Lippincott-Schwartz, and Craig Blackstone. Er proteins decipher the tubulin code to regulate organelle distribution. *Nature*, 601(7891):132–138, 2022.

[87] Pinar S Gurel, Anna L Hatch, and Henry N Higgs. Connecting the cytoskeleton to the endoplasmic reticulum and golgi. *Curr Biol*, 24(14):R660–R672, 2014.

[88] Denis Vecellio Reane, Rosario Rizzuto, and Anna Raffaello. The er-mitochondria tether at the hub of ca2+ signaling. *Curr Opin Physiol*, 17:261–268, 2020.

[89] Jeeyun Chung, Federico Torta, Kaori Masai, Louise Lucast, Heather Czapla, Lukas B Tanner, Pradeep Narayanaswamy, Markus R Wenk, Fubito Nakatsu, and Pietro De Camilli. Pi4p/phosphatidylserine countertransport at orp5-and orp8-mediated er–plasma membrane contacts. *Science*, 349(6246):428–432, 2015.

[90] Kentaro Hanada, Keigo Kumagai, Satoshi Yasuda, Yukiko Miura, Miyuki Kawano, Masayoshi Fukasawa, and Masahiro Nishijima. Molecular machinery for non-vesicular trafficking of ceramide. *Nature*, 426(6968):803–809, 2003.

[91] Diego Peretti, Nili Dahan, Eyal Shimoni, Koret Hirschberg, and Sima Lev. Coordinated lipid transfer between the endoplasmic reticulum and the golgi complex requires the vap proteins and is essential for golgi-mediated transport. *Mol Biol Cell*, 19(9):3871–3884, 2008.

[92] Tasuku Konno, Pierre Parutto, Cécile C Crapart, Valentina Davì, David MD Bailey, Mosab Ali Awadelkareem, Colin Hockings, Aidan I Brown, Katherine M Xiang, Anamika Agrawal, Joseph E Chambers, Molly J Vander Werp, Katherine M Koning, Louis M Elfari, Sam Steen, Emmanouil Metzakopian, Laura M Westrate, Elena F Koslover, and Edward Avezov. Endoplasmic reticulum morphology regulation by rtn4 modulates neuronal regeneration by curbing luminal transport. *Cell Reports*, 43(7), 2024.

[93] Zubenelgenubi C Scott, Katherine Koning, Molly Vanderwerp, Lorna Cohen, Laura M Westrate, and Elena F Koslover. Endoplasmic reticulum network heterogeneity guides diffusive transport and kinetics. *Biophys J*, 122(15):3191–3205, 2023.

[94] Lars Dreier and Tom A Rapoport. In vitro formation of the endoplasmic reticulum occurs independently of microtubules by a controlled fusion reaction. *The Journal of cell biology*, 148(5):883–898, 2000.

[95] Mark J Schnitzer and Steven M Block. Kinesin hydrolyses one atp per 8-nm step. *Nature*, 388(6640):386–390, 1997.

[96] Friederike Thor, Matthias Gautschi, Roger Geiger, and Ari Helenius. Bulk flow revisited: transport of a soluble protein in the secretory pathway. *Traffic*, 10(12):1819–1830, 2009.

[97] Mark J Dayel, Erik FY Hom, and Alan S Verkman. Diffusion of green fluorescent protein in the aqueous-phase lumen of endoplasmic reticulum. *Biophys J*, 76(5):2843–2851, 1999.

[98] Ron Milo and Rob Phillips. *Cell biology by the numbers*. Garland Science, 2015.

[99] Ian Parker and Isabel Ivorra. Localized all-or-none calcium liberation by inositol trisphosphate. *Science*, 250(4983):977–979, 1990.

[100] Melissa J Phillips and Gia K Voeltz. Structure and function of er membrane contact sites with other organelles. *Nat Rev Mol Cell Bio*, 17(2):69–82, 2016.

[101] Robert G Abrisch, Samantha C Gumbin, Brett Taylor Wisniewski, Laura L Lackner, and Gia K Voeltz. Fission and fusion machineries converge at er contact sites to regulate mitochondrial morphology. *Journal of Cell Biology*, 219(4):e201911122, 2020.

[102] Janina Kroll and Jörg Renkawitz. Principles of organelle positioning in motile and non-motile cells. *EMBO Rep*, pages 1–16, 2024.

[103] Xinjian Wang, Chengyu Fan, Yanfen Liu, and Yan Zou. The interconnection of endoplasmic reticulum and microtubule and its implication in hereditary spastic paraplegia. *Computational and Structural Biotechnology Journal*, 21:1670–1677, 2023.

[104] Ginny G Farías, Amélie Fréal, Elena Tortosa, Riccardo Stucchi, Xingxiu Pan, Sybren Portegies, Lena Will, Maarten Altelaar, and Casper C Hoogenraad. Feedback-driven mechanisms between microtubules and the endoplasmic reticulum instruct neuronal polarity. *Neuron*, 102(1):184–201, 2019.

[105] Mark Terasaki, Lan Bo Chen, and Keigi Fujiwara. Microtubules and the endoplasmic reticulum are highly interdependent structures. *The Journal of cell biology*, 103(4):1557–1568, 1986.

[106] Lei Lu, Mark S Ladinsky, and Tom Kirchhausen. Cisternal organization of the endoplasmic reticulum during mitosis. *Mol Biol Cell*, 20(15):3471–3480, 2009.

[107] Songyu Wang, Fabian B Romano, Christine M Field, Tim J Mitchison, and Tom A Rapoport. Multiple mechanisms determine er network morphology during the cell cycle in xenopus egg extracts. *J Cell Biol*, 203(5):801–814, 2013.

[108] Matt J. spatialgraph2d. https://www.mathworks.com/matlabcentral/fileexchange/73630-spatialgraph2d. Retrieved: May 1, 2022.

[109] Amber R English and Gia K Voeltz. Rab10 gtpase regulates er dynamics and morphology. *Nat Cell Biol*, 15(2):169–178, 2013.

[110] Stuart Berg, Dominik Kutra, Thorben Kroeger, Christoph N. Straehle, Bernhard X. Kausler, Carsten Haubold, Martin Schiegg, Janez Ales, Thorsten Beier, Markus Rudy, Kemal Eren, Jaime I. Cervantes, Buote Xu, Fynn Beuttenmueller, Adrian Wolny, Chong Zhang, Ullrich Koethe, Fred A. Hamprecht, and Anna Kreshuk. ilastik: interactive machine learning for (bio)image analysis. *Nat Methods*, 16(12):1226–1232, September 2019.

[111] MATLAB. *version 9.11 (R2021b)*. The MathWorks Inc., Natick, Massachusetts, 2021.

[112] Olivier Bénichou and R Voituriez. From first-passage times of random walks in confinement to geometry-controlled kinetics. *Physics Reports*, 539(4):225–284, 2014.

[113] Naoki Masuda, Mason A Porter, and Renaud Lambiotte. Random walks and diffusion on networks. *Physics reports*, 716:1–58, 2017.

[114] Elliott W Montroll and George H Weiss. Random walks on lattices. ii. *J Math Phys*, 6(2):167–181, 1965.

[115] Itzhak Fouxon and Markus Holzner. Solvable continuous-time random walk model of the motion of tracer particles through porous media. *Phys Rev E*, 94(2):022132, 2016.

[116] Elena F Koslover and Andrew J Spakowitz. Force fluctuations impact kinetics of biomolecular systems. *Phys Rev E*, 86(1):011906, 2012.

[117] Ludvig Lizana and Zoran Konkoli. Diffusive transport in networks built of containers and tubes. *Phys Rev E*, 72(2):026305, 2005.

[118] Jeroen S. Van Zon and Pieter Rein Ten Wolde. Green's-function reaction dynamics: A particle-based approach for simulating biochemical networks in time and space. *J Chem Phys*, 123(23), 2005.

[119] Jeroen S van Zon and Pieter Rein Ten Wolde. Simulating biochemical networks at the particle level and in time and space: Green's function reaction dynamics. *Phys Rev Lett*, 94(12):128103, 2005.

[120] Thomas R Sokolowski, Joris Paijmans, Laurens Bossen, Thomas Miedema, Martijn Wehrens, Nils B Becker, Kazunari Kaizu, Koichi Takahashi, Marileen Dogterom, and Pieter Rein Ten Wolde. egfrd in all dimensions. *J Chem Phys*, 150(5):054108, 2019.

[121] Saurabh S. Mogre and Elena F. Koslover. Multimodal transport and dispersion of organelles in narrow tubular cells. *Phys Rev E*, 97(4):42402, 2018.

[122] Dianne S. Schwarz and Michael D. Blower. The endoplasmic reticulum: Structure, function and response to cellular signaling. *Cell Mol Life Sci*, 73(1):79–94, 2016.

[123] Susanne M Rafelski. Mitochondrial network morphology: building an integrative, geometrical view. *Bmc Biol*, 11(1):1–9, 2013.

[124] Valerii M Sukhorukov, Daniel Dikov, Andreas S Reichert, and Michael Meyer-Hermann. Emergence of the mitochondrial reticulum from fission and fusion dynamics. *PLoS Comput Biol*, 8(10):e1002745, 2012.

[125] Hanne Hoitzing, Iain G Johnston, and Nick S Jones. What is the function of mitochondrial networks? a theoretical assessment of hypotheses and proposal for future research. *Bioessays*, 37(6):687–700, 2015.

[126] Karin B Busch, Axel Kowald, and Johannes N Spelbrink. Quality matters: how does mitochondrial network dynamics and quality control impact on mtdna integrity? *Philosophical Transactions of the Royal Society B: Biological Sciences*, 369(1646):20130442, 2014.

[127] Gilad Twig and Orian S Shirihai. The interplay between mitochondrial dynamics and mitophagy. *Antioxid Redox Sign*, 14(10):1939–1951, 2011.

[128] Pinkesh K Patel, Orian Shirihai, and Kerwyn Casey Huang. Optimal dynamics for quality control in spatially distributed mitochondrial networks. *PLoS Comput Biol*, 9(7):e1003108, 2013.

[129] Vladimir P Skulachev. Mitochondrial filaments and clusters as intracellular power-transmitting cables. *Trends Biochem Sci*, 26(1):23–29, 2001.

[130] David Holcman, Pierre Parutto, Joseph E Chambers, Marcus Fantham, Laurence J Young, Stefan J Marciniak, Clemens F Kaminski, David Ron, and Edward Avezov. Single particle trajectories reveal active endoplasmic reticulum luminal flow. *Nat Cell Biol*, 20(10):1118, 2018.

[131] John D Chodera and Frank Noé. Markov state models of biomolecular conformational dynamics. *Curr Opin Struc Biol*, 25:135–144, 2014.

[132] Alexander M Lorenzo, M Enrique, and Elena F Koslover. Thermal fracture kinetics of heterogeneous semiflexible polymers. *Soft Matter*, 16(8):2017–2024, 2020.

[133] Sidney Redner. *A guide to first-passage processes*. Cambridge University Press, 2001.

[134] Aidan I Brown and Elena F Koslover. Design principles for the glycoprotein quality control pathway. *Plos Comput Biol*, 17(2):e1008654, 2021.

[135] Annika Budnik and David J Stephens. Er exit sites–localization and control of copii vesicle formation. *Febs Lett*, 583(23):3796–3803, 2009.

[136] Nica Borgese. Getting membrane proteins on and off the shuttle bus between the endoplasmic reticulum and the golgi complex. *J Cell Sci*, 129(8):1537–1545, 2016.

[137] Denis S Grebenkov, Ralf Metzler, and Gleb Oshanin. Strong defocusing of molecular reaction times results from an interplay of geometry and reaction control. *Communications Chemistry*, 1(1):1–12, 2018.

[138] Maria P Kochugaeva, Alexander M Berezhkovskii, and Anatoly B Kolomeisky. Optimal length of conformational transition region in protein search for targets on dna. *J Phys Chem Lett*, 8(17):4049–4054, 2017.

[139] David Ando, Nickolay Korabel, Kerwyn Casey Huang, and Ajay Gopinathan. Cytoskeletal network morphology regulates intracellular transport dynamics. *Biophys J*, 109(8):1574–1582, 2015.

[140] Saurabh S Mogre, Jenna R Christensen, Cassandra S Niman, Samara L Reck-Peterson, and Elena F Koslover. Hitching a ride: Mechanics of transport initiation through linker-mediated hitchhiking. *Biophys J*, 118(6):1357–1369, 2020.

[141] Saurabh S Mogre, Aidan I. Brown, and Elena F. Koslover. Getting around the cell: Physical transport in the intracellular world. *Phys Biol*, 17(6), 2020.

[142] Gero Steinberg. Endocytosis and early endosome motility in filamentous fungi. *Curr Opin Microbiol*, 20:10–18, 2014.

[143] Sandra Maday, Alison E Twelvetrees, Armen J Moughamian, and Erika LF Holzbaur. Axonal transport: cargo-specific mechanisms of motility and regulation. *Neuron*, 84(2):292–309, 2014.

[144] Jan-Heiko Lenz, Isabel Schuchardt, Anne Straube, and Gero Steinberg. A dynein loading zone for retrograde endosome motility at microtubule plus-ends. *Embo J*, 25(11):2275–2286, 2006.

[145] Armen J Moughamian, Gregory E Osborn, Jacob E Lazarus, Sandra Maday, and Erika LF Holzbaur. Ordered recruitment of dynactin to the microtubule plus-end is required for efficient initiation of retrograde axonal transport. *J Neurosci*, 33(32):13190–13203, 2013.

[146] Daniel N Hebert and Maurizio Molinari. In and out of the er: protein folding, quality control, degradation, and related human diseases. *Physiol Rev*, 87(4):1377–1408, 2007.

[147] Steven S Andrews and Dennis Bray. Stochastic simulation of chemical reactions with spatial resolution and single molecule detail. *Phys Biol*, 1(3):137, 2004.

[148] Daniel T Gillespie. Exact stochastic simulation of coupled chemical reactions. *J Phys Chem-us*, 81(25):2340–2361, 1977.

[149] George B Arfken and Hans J Weber. Mathematical methods for physicists, 1999.

[150] S Bravo Yuste and Katja Lindenberg. Order statistics for first passage times in one-dimensional diffusion processes. *J Stat Phys*, 85(3):501–512, 1996.

[151] K Basnayake, Zeev Schuss, and David Holcman. Asymptotic formulas for extreme statistics of escape times in 1, 2 and 3-dimensions. *J Nonlinear Sci*, 29(2):461–499, 2019.

[152] Vincent Tejedor, Michaela Schad, Olivier Bénichou, Raphael Voituriez, and Ralf Metzler. Encounter distribution of two random walkers on a finite one-dimensional interval. *Journal of Physics A: Mathematical and Theoretical*, 44(39):395005, 2011.

[153] Eleni Katifori, Gergely J Szöllősi, and Marcelo O Magnasco. Damage and fluctuations induce loops in optimal transport networks. *Phys Rev Lett*, 104(4):048704, 2010.

[154] Vittoria Colizza, Romualdo Pastor-Satorras, and Alessandro Vespignani. Reaction–diffusion processes and metapopulation models in heterogeneous networks. *Nat Phys*, 3(4):276–282, 2007.

[155] Lena K Schroeder, Andrew ES Barentine, Holly Merta, Sarah Schweighofer, Yongdeng Zhang, David Baddeley, Joerg Bewersdorf, and Shirin Bahmanyar. Dynamic nanoscale morphology of the er surveyed by sted microscopy. *J Cell Biol*, 218(1):83–96, 2019.

[156] Cindy EJ Dieteren, Stan CAM Gielen, Leo GJ Nijtmans, Jan AM Smeitink, Herman G Swarts, Roland Brock, Peter HGM Willems, and Werner JH Koopman. Solute diffusion is hindered in the mitochondrial matrix. *P Natl Acad Sci*, 108(21):8657–8662, 2011.

[157] Mark Terasaki, Tom Shemesh, Narayanan Kasthuri, Robin W Klemm, Richard Schalek, Kenneth J Hayworth, Arthur R Hand, Maya Yankova, Greg Huber, Jeff W Lichtman, Tom A Rapoport, and Michael M Kozlov. Stacked endoplasmic reticulum sheets are connected by helicoidal membrane motifs. *Cell*, 154(2):285–296, 2013.

[158] Mithila Burute and Lukas C Kapitein. Cellular logistics: unraveling the interplay between microtubule organization and intracellular transport. *Annu Rev Cell Dev Bi*, 35(1):29–54, 2019.

[159] Jennifer L Ross, M Yusuf Ali, and David M Warshaw. Cargo transport: molecular motors navigate a complex cytoskeleton. *Curr Opin Cell Biol*, 20(1):41–47, 2008.

[160] Saurabh S Mogre, Aidan I Brown, and Elena F Koslover. Getting around the cell: physical transport in the intracellular world. *Phys Biol*, 17(6):061003, 2020.

[161] Anamika Agrawal, Zubenelgenubi C Scott, and Elena F Koslover. Morphology and transport in eukaryotic cells. *Ann Rev Biophys*, 51:247–266, 2022.

[162] Greg Huber and Michael Wilkinson. Terasaki spiral ramps and intracellular diffusion. *Phys Biol*, 16(6):065002, 2019.

[163] Alex H Williams, Cian O'Donnell, Terrence J Sejnowski, and Timothy O'Leary. Dendritic trafficking faces physiologically critical speed-precision tradeoffs. *elife*, 5:e20556, 2016.

[164] Ran Li, Justin A Fowler, and Brian A Todd. Calculated rates of diffusion-limited reactions in a three-dimensional network of connected compartments: application to porous catalysts and biological systems. *Phys Rev Lett*, 113(2):028303, 2014.

[165] Yunhao Sun, Zexi Yu, Christopher J Obara, Keshav Mittal, Jennifer Lippincott-Schwartz, and Elena F Koslover. Unraveling trajectories of diffusive particles on networks. *Phys Rev Res*, 4(2):023182, 2022.

[166] Nahuel Zamponi, Emiliano Zamponi, Sergio A Cannas, Orlando V Billoni, Pablo R Helguera, and Dante R Chialvo. Mitochondrial network complexity emerges from fission/fusion dynamics. *Sci Rep*, 8(1):1–10, 2018.

[167] Tasuku Konno, Pierre Parutto, David MD Bailey, Valentina Davì, Cécile C Crapart, Mosab Ali Awadelkareem, Colin Hockings, Aidan I Brown, Katherine M Xiang, Anamika Agrawal, Joseph E Chambers, Molly J Vander Werp, Katherine M Koning, Emmanouil Metzakopian, Laura M Westrate, Elena F Koslover, and Edward Avezov. Endoplasmic reticulum morphological regulation by rtn4/nogo modulates neuronal regeneration by curbing luminal transport. *bioRxiv*, 2021.

[168] Zitao Yang and Elena F Koslover. Diffusive exit rates through pores in membrane-enclosed structures. *Phys Biol*, 2023.

[169] Shiri Kamhi-Nesher, Marina Shenkman, Sandra Tolchinsky, Sharon Vigodman Fromm, Rachel Ehrlich, and Gerardo Z Lederkremer. A novel quality control compartment derived from the endoplasmic reticulum. *Mol Biol Cell*, 12(6):1711–1723, 2001.

[170] Emily M Sontag, Willianne IM Vonk, and Judith Frydman. Sorting out the trash: the spatial nature of eukaryotic protein quality control. *Curr Opin Cell Biol*, 26:139–146, 2014.

[171] Nesia Zurek, Lenore Sparks, and Gia Voeltz. Reticulon short hairpin transmembrane domains are used to shape er tubules. *Traffic*, 12(1):28–41, 2011.

[172] Dibyendu Bhattacharyya and Benjamin S Glick. Two mammalian sec16 homologues have nonredundant functions in endoplasmic reticulum (er) export and transitional er organization. *Mol Biol Cell*, 18(3):839–849, 2007.

[173] David J Stephens, Nathalie Lin-Marq, Alessandra Pagano, Rainer Pepperkok, and Jean-Pierre Paccaud. Copi-coated er-to-golgi transport complexes segregate from copii in close proximity to er exit sites. *J Cell Sci*, 113(12):2177–2185, 2000.

[174] Christopher I Richards, Rahul Srinivasan, Cheng Xiao, Elisha DW Mackey, Julie M Miwa, and Henry A Lester. Trafficking of $\alpha 4^*$ nicotinic receptors revealed by superecliptic phluorin: effects of a $\beta 4$ amyotrophic lateral sclerosis-associated mutation and chronic exposure to nicotine. *J Biol Chem*, 286(36):31241–31249, 2011.

[175] George H Patterson and Jennifer Lippincott-Schwartz. A photoactivatable gfp for selective photolabeling of proteins and cells. *Science*, 297(5588):1873–1877, 2002.

[176] Melissa J Hoyer, Patrick J Chitwood, Christopher C Ebmeier, Jonathan F Striepen, Robert Z Qi, William M Old, and Gia K Voeltz. A novel class of er membrane proteins regulates er-associated endosome fission. *Cell*, 175(1):254–265, 2018.

[177] Christophe Leys, Christophe Ley, Olivier Klein, Philippe Bernard, and Laurent Licata. Detecting outliers: Do not use standard deviation around the mean, use absolute deviation around the median. *J Exp Soc Psychol*, 49(4):764–766, 2013.

[178] Jan Wilhelm and Erwin Frey. Elasticity of stiff polymer networks. *Phys Rev Lett*, 91(10):108103, 2003.

[179] John C Crocker and David G Grier. Methods of digital video microscopy for colloidal studies. *J Colloid Interf Sci*, 179(1):298–310, 1996.

[180] Elena F Koslover, Caleb K Chan, and Julie A Theriot. Disentangling random motion and flow in a complex medium. *Biophys J*, 110(3):700–709, 2016.

[181] Tongfeng Weng, Jie Zhang, Michael Small, and Pan Hui. Hunting for a moving target on a complex network. *Europhys Lett*, 119(4):48006, 2017.

[182] Konstantin Speckner, Lorenz Stadler, and Matthias Weiss. Unscrambling exit site patterns on the endoplasmic reticulum as a quenched demixing process. *Biophys J*, 120(12):2532–2542, 2021.

[183] Arpita Upadhyaya and Michael P Sheetz. Tension in tubulovesicular networks of golgi and endoplasmic reticulum membranes. *Biophys J*, 86(5):2923–2928, 2004.

[184] Alexandre Toulmay and William A Prinz. Lipid transfer and signaling at organelle contact sites: the tip of the iceberg. *Curr Opin Cell Biol*, 23(4):458–463, 2011.

[185] Máté Katona, Ádám Bartók, Zuzana Nichtova, György Csordás, Elena Berezhnaya, David Weaver, Arijita Ghosh, Péter Várnai, David I Yule, and György Hajnóczky. Capture at the er-mitochondrial contacts licenses ip3 receptors to stimulate local ca2+ transfer and oxidative metabolism. *Nature Commun*, 13(1):6779, 2022.

[186] Larissa Heinrich, Davis Bennett, David Ackerman, Woohyun Park, John Bogovic, Nils Eckstein, Alyson Petruncio, Jody Clements, Song Pang, C Shan Xu, Jan Funke, Wyatt Korff, Harold F Hess, Jennifer Lippincott-Schwartz, Stephan Saalfeld, Aubrey V Weigel, and COSEM Project Team. Whole-cell organelle segmentation in volume electron microscopy. *Nature*, 599(7883):141–146, 2021.

[187] Maija Puhka, Helena Vihinen, Merja Joensuu, and Eija Jokitalo. Endoplasmic reticulum remains continuous and undergoes sheet-to-tubule transformation during cell division in mammalian cells. *The Journal of cell biology*, 179(5):895–909, 2007.

[188] Yumei Wu, Christina Whiteus, C Shan Xu, Kenneth J Hayworth, Richard J Weinberg, Harald F Hess, and Pietro De Camilli. Contacts between the endoplasmic reticulum and other membranes in neurons. *Proceedings of the National Academy of Sciences*, 114(24):E4859–E4867, 2017.

[189] Mahmoud Elgendy, Hiromi Tamada, Takaya Taira, Yuma Iio, Akinobu Kawamura, Ayusa Kunogi, Yuka Mizutani, and Hiroshi Kiyama. Dynamic changes in endoplasmic reticulum morphology and its contact with the plasma membrane in motor neurons in response to nerve injury. *Cell and Tissue Research*, 396(1):71–84, 2024.

[190] Junjie Hu, William A Prinz, and Tom A Rapoport. Weaving the web of er tubules. *Cell*, 147(6):1226–1231, 2011.

[191] Yuting Guo, Di Li, Siwei Zhang, Yanrui Yang, Jia-Jia Liu, Xinyu Wang, Chong Liu, Daniel E Milkie, Regan P Moore, U Serdar Tulu, Daniel P Kiehart, Junjie Hu, Jennifer Lippincott-Schwartz, Eric Betzig, and Dong Li. Visualizing intracellular organelle and cytoskeletal interactions at nanoscale resolution on millisecond timescales. *Cell*, 175(5):1430–1442, 2018.

[192] Nadine R Lang, Stefan Münster, Claus Metzner, Patrick Krauss, Sebastian Schürmann, Janina Lange, Katerina E Aifantis, Oliver Friedrich, and Ben Fabry. Estimating the 3d pore size distribution of biopolymer networks from directionally biased data. *Biophysical journal*, 105(9):1967–1975, 2013.

[193] Chase P Broedersz and Fred C MacKintosh. Modeling semiflexible polymer networks. *Reviews of Modern Physics*, 86(3):995–1036, 2014.

[194] Evgeniy Khain and Lev S Tsimring. Effective pressure and cell area distribution in a confined monolayer. *Fluid Dynamics Research*, 50(5):051413, 2018.

[195] MATLAB. *version 9.5 (R2018b)*. The MathWorks Inc., Natick, Massachusetts, 2018.

[196] Tobias Ambjörnsson, Ludvig Lizana, Michael A Lomholt, and Robert J Silbey. Single-file dynamics with different diffusion constants. *J Chem Phys*, 129(18):11B612, 2008.

[197] Howard C Berg and Edward M Purcell. Physics of chemoreception. *Biophys J*, 20(2):193–219, 1977.